DEPARTAMENT DE FÍSICA ATÒMICA
MOLECULAR I NUCLEAR

VNIVERSITAT DE VALÈNCIA

(ESTUDI GENERAL)

Study of the performances of several layouts and geometries for the future ANTARES neutrino telescope

TRABAJO DE INVESTIGACIóN

JUAN ANTONIO AGUILAR SÁNCHEZ

July 2004

D. JUAN JOSÉ HERNÁNDEZ REY, Investigador Científico del C.S.I.C.,

CERTIFICA :

Que la presente memoria, **Study of the performances of several layouts and geometries for the future ANTARES neutrino telescope**, ha sido realizada bajo su dirección en el Departamento de Física Atómica, Molecular y Nuclear de la Universitat de València por D. Juan Antonio Aguilar Sánchez y constituye su Trabajo de Investigación del Tercer Ciclo que sigue en este Departamento para optar al grado de Doctor en Física.

Y para que conste, en cumplimiento de la legislación vigente, firmo el presente Certificado en Burjassot a 13 de Julio de 2004.

Fdo.: Juan José Hernández Rey

Visto bueno del Director del Depto.: D. Ramón Cases Ruiz

A mis padres y hermana

Agradecimientos

Deseo dar las gracias en primer lugar a mi director D. Juan José Hernández Rey, por haberme permitido formar parte del grupo ANTARES Valencia. Darle las gracias también por la confianza depositada en mí para la realización de este trabajo y por todos su comentarios y consejos que tan acertadamente han elevado la calidad de este estudio.

A mi tutor Juan Zúñiga por ser uno de los mejores profesores y descubrirme el mundo de la física experimental. Deseo agradecerle también el haber estado siempre dispuesto a escucharme y orientarme cuando ha surgido algún problema.

A Emiliano, sin cuya ayuda este trabajo no habría visto la luz, deseo agradecerle las horas empleadas en explicaciones a veces incluso al margen de la física. Toda su labor previa y el acierto de sus respuestas han sido vitales para la realización de este trabajo. En deuda quedan su paciencia ante mis preguntas y como regalo me llevo su valiosa amistad.

A Juan de Dios por ser un gran compañero de despacho y mejor amigo. Gracias por ayudarme a integrarme sin dificultad dentro de la colaboración. Agradecerle también todos los comentarios y explicaciones sobre la física inherente al detector. Le doy también las gracias por las muchas y muy distintas cosas que he podido aprender de él.

Gracias a Jürgen Brunner por su ayuda en muchos de los aspectos de los trazados de los detectores.

Deseo también dar las gracias a Víctor y Diego por hacer que los viajes al CERN fueran más divertidos que simples viajes de trabajo. Mi agradecimiento al proyecto GRID de Valencia, y en especial a Javi, por toda la ayuda prestada. A Santi y Pablo por ser unos excelentes compañeros de trabajo y de piso. A Tere, Amparo, Paqui, Asun, Gabriela, Farida y demás compañeros del IFIC por su inestimable ayuda cuando la he necesitado.

Gracias a mis amigos en Albacete por hacer que los fines de semana sean algo más que el final de otra semana.

Y gracias a mis padres y a mi hermana. Son muchas cosas las que os debo y ahora he de añadir todo el apoyo y ánimo que me habéis dado y que no son pocos. Gracias por permitirme hacer lo que más me gusta.

Finalmente, agradecer especialmente a Andrea por haber estado siempre a mi lado apoyándome incluso en las decisiones más difíciles. Por toda su comprensión y cariño, gracias.

Son muchas las personas, en ocasiones anónimas, que con su apoyo han hecho posible la realización de este trabajo. A todas ellas van dirigidas estas líneas de agradecimiento aún sabiendo que escasas, no son suficientes para mostrar toda mi gratitud.

Contents

Introduction

Although the Universe has been observed thoroughly using mainly the electromagnetic spectrum, still there are unanswered questions. The origin of ultra high energy cosmic rays, gamma ray bursts (GBRs) to mention some of them, are topics still not well settled. However, there are other cosmic messengers that can provide complementary information. Among these new messengers, neutrinos are expected to be a powerful tool to survey the sky. Neutrino Astronomy is a relatively recent field which presents a great interest as it is a very good complement to the observations by photons.

Recent observations in the gamma ray spectrum show us a violent Universe crowded with high energy gamma ray sources. In these scenarios, high energy photons should be produced together with high energy neutrino emission whose detection could provide new evidence about the physics that rules some astrophysical objects. The advantage of Neutrino Astronomy is that neutrinos interact weakly with matter, therefore they can travel through very dense amounts of matter and radiation. On the other hand, high energy photons produced at the furthest sources will not reach the Earth due to the interaction at high energies with matter, infra–red radiation and microwave background. Photons with energy E > 10 TeV coming from sources farther than 100 Mpc away are likely to be unobservable.

Moreover, the magnetic fields deflect charged particles as protons, spoiling any directional information. Neutrons could be a good messenger since they are electrically neutral, however, their short lifetime makes them decay before reaching long distances (neutrons with energies of $E_n \sim$ EeV travel less than 10 kpc).

Neutrinos, on the contrary, are stable and neutral, hence they are not deflected by magnetic fields and can travel long distances. Nevertheless, as they are weakly interacting particles, the neutrino detection is a very difficult task that implies the use of very large detectors.

Several methods are proposed for the detection of high energy neutrino. The construction of underwater/ice telescopes turns out, probably, to be the best option in the GeV to PeV energy region. The detection principle is based on the Cherenkov light emission from muons produced in the charged current interaction of the neutrino with the matter surrounding the detector.

The ANTARES experiment is carried out by an international collaboration aiming at the construction of an underwater telescope in the Mediterranean Sea.

The main goal of the first stage of this project is the construction of a 0.1 km^2 detector which will be completely deployed by 2007. This detector will be made up of

12 strings spread over the seabed forming a tridimensional array of photomultipliers. The study of such configuration is one of the main preliminary tasks when building the detector. The optimization of this arrangement can improve the performances of the detector, by increasing the effective area and therefore the telescope efficiency. This research work deals with the study of the several string layouts as well as several *intra–string* designs.

In the first chapter we will review the basic principles of Neutrino Astronomy. We will inquire on the limitations of the traditional photon astronomy and the way they can be overcome by Neutrino Astronomy. Also we will mention the physics within the scope of the ANTARES experiment.

In chapter two a more detail description of the ANTARES telescope and its performances will be shown. Software tools will be presented and summarized, also the main magnitudes such as effective areas and angular resolution will be defined since they are used to give a measurable value of the telescope efficiency.

Chapter three contains the first approach to the problem of a new detector layout and design. In this chapter a set of new 12–string detectors layouts will be proposed and the response of these new detectors will be studied and compared with respect to the original 10–string detector layout.

In chapter four we will continue the study started in chapter three by proposing more detectors with other characteristics, but preserving the same number of photomultipliers. Also a study of the *single–line* reconstruction strategy will be performed in order to see how these new *intra–strings* designs may affect this reconstruction strategy.

Finally, we will summarize the results obtained by the different detector geometries and their performances, and the final selection of the detector and the reasons that lead to this decision.

Chapter 1

High energy Neutrino Astronomy

Neutrino Astronomy as science has an early birth. In this chapter we inquire into the reasons that lead to this new astronomy, from the open questions about the origin of Cosmic Rays to the nature of the Dark Matter in the Universe.

1.1 High energy cosmic rays

Our planet is continuously being hit by a flux of high energetic particles that are shielded by Earth's atmosphere but have many indirect effects such as ionization and showers of secondary charged particles. In fact, it was by measuring ionization from a balloon that Victor Hess discovered these high energy cosmic rays (CR) [1]. The existence of these showers is caused by energetic primary particles. These particles are mostly ionized nuclei (90% protons, 9% alpha particles and rest, heavy nuclei). The Earth receives about 1000 particles per second per square metre with an individual energy of up to 10^{20} eV. The energy spectrum of the cosmic rays follow a power-law behaviour:

$$dI \propto E^{-\gamma} dE \tag{1.1}$$

The γ index is called the *spectral index*. The spectrum of cosmic rays at Earth is characterized by $\gamma \sim 2.7$. This power-law tendency can be seen in Figure 1.1. There is a change in the *spectral index* value at $E_{primary} \simeq 4 \times 10^{15}$ eV. This part of the spectrum is often named the *knee*, the power-law index changes from the already mentioned value to $\gamma \sim 3.1$. At energies about $E_{primary} \simeq 10^{19}$ eV there is another change in the slope (*ankle*) and the *spectral index* returns to be $\gamma \sim 2.7$. Beyond the *ankle* the behaviour is still controversial (see below). In Figure 1.2, the CRs flux as a function of energy is presented multiplied by E^3 in order to show more clearly the drops in the energy spectrum due to changes in the *spectral index*.

At energies between 10^{19} and 10^{20} eV there is a phenomena known as the Greisen-Zatsepin-Kuz'min (GZK) cut-off [2]. This cut-off was predicted as the consequence of the proton interactions with the cosmic microwave background: those protons with

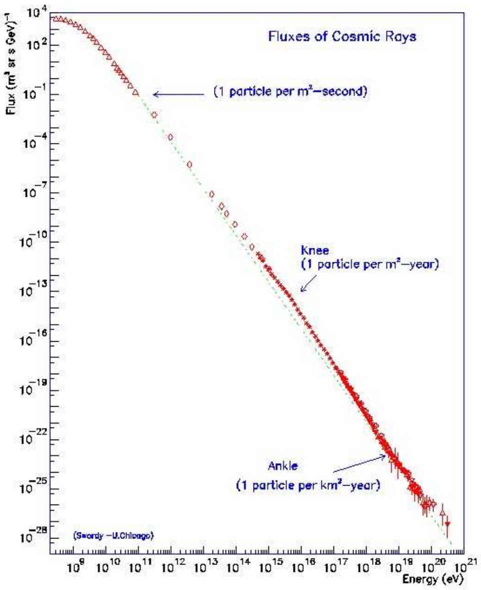

Figure 1.1: Cosmic ray spectrum. Both knee and ankle locations are indicated.

energy about 10^2 EeV are not able to travel distances further than a few Mpc. Astrophysical objects at distances smaller than 50 Mpc are needed in order to explain events beyond the GZK cut-off. However, currently there seems to be a disagreement between the AGASA ground array detector [3] that has detected about 8 events above 10^{20} eV, and the HiRes fluorescence detector [4] whose data seems to be consistent with a cut-off (see Fig 1.3).

1.1.1 Origin of cosmic rays: Fermi Acceleration

The mechanism responsible for the acceleration of particles to high energies is supposed to be the Fermi Mechanism. This process was firstly described by Enrico Fermi in 1949 [5], to explain particle acceleration in the shock–waves of supernovas. Nevertheless, shock–waves play a major role in many other astrophysical environments such as gamma ray burst, active galaxy nuclei or even crashing galaxies. Localized shock–waves form when gas flows at supersonic velocity relative to the local velocity of sound. The Fermi mechanism explains how the kinetic energy of the magnetic plasma is transferred to individual charged particles. The concept of the Fermi Mechanism is that a particle suffers an *encounter* with something that increases its energy a fraction (ξ) of its initial energy E_0, after n encounters the final energy of the particle is:

$$E_n = E_0(1+\xi)^n \tag{1.2}$$

The index n can be written as t/T_{Cycle} where t is the time of the acceleration process and

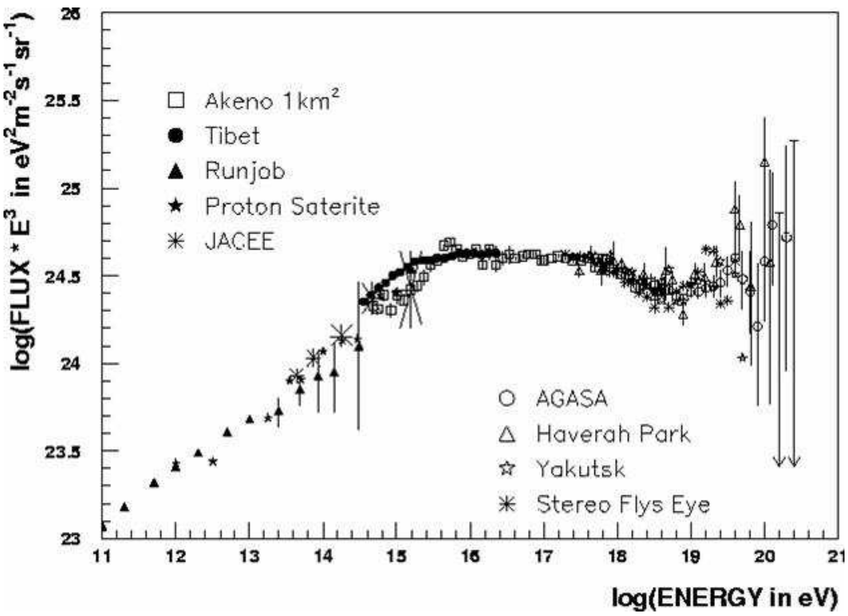

Figure 1.2: Blow-up of the high energy region of the cosmic ray spectrum. The flux is multiplied by E^3 to highlight the change of slope in the *knee* and *ankle* regions.

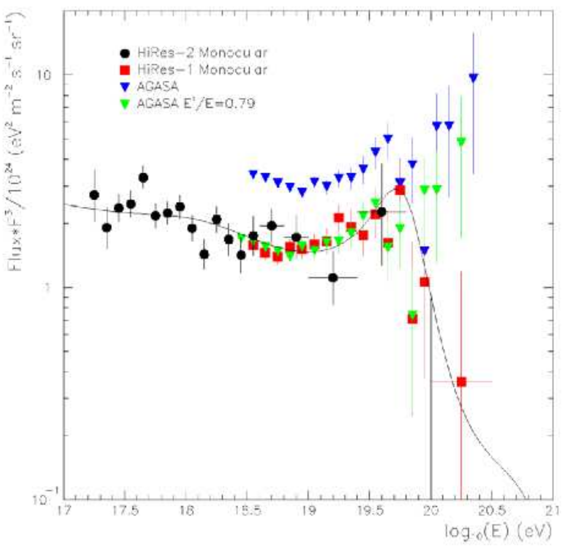

Figure 1.3: Predicted high energy cosmic ray (solid line) and events reconstructed by the AGASA ground telescope and the HiRes fluorescence detector.

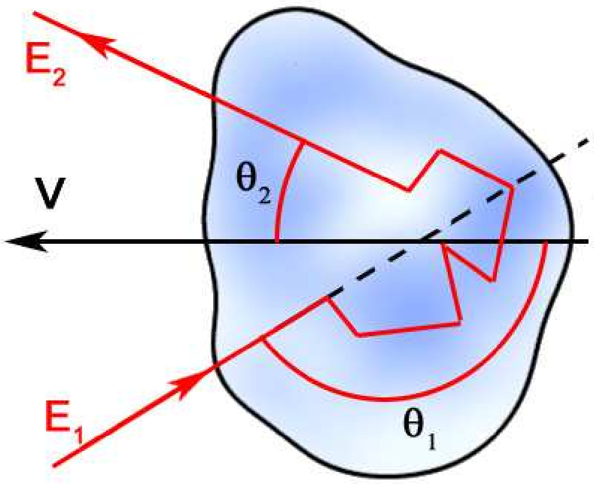

Figure 1.4: Schematic view of the 2^{nd} order Fermi acceleration mechanism.

T_{Cycle} is the characteristic time for the acceleration cycle. The Fermi Mechanism leads to the desired spectrum power-law. This generic concept can be applied on several models, both for relativistic and non-relativistic fluxes of plasma. Historically, the *encounters* were proposed to be with clouds of magnetic irregularities (see figure 1.4) that reflect charged particles through magnetic resonance between the gyromotion and waves in the ionized magnetic gas, the plasma.

This is known as the 2^{nd} order Fermi acceleration mechanism. Particles may increase or lose their energy per *encounter* depending on the incident angles, but on average there is a net increase:

$$\frac{\langle \Delta E \rangle}{E} \simeq \frac{4}{3}\beta^2 \tag{1.3}$$

where $\beta \equiv V/c$ is the speed of the cloud. During the 70's the original idea of Fermi was modified to describe a more efficient acceleration considering a shock-wave gain energy by going back and forth between the two sides of the shock (see figure 1.5). This concept was proposed for the supernova scenario, but it can be applied to any astrophysical context that involves shock–waves.

The average increase of the particle energy depends now on the 1^{st} power of β, where β refers to the relative velocity of the shocked plasma flow:

$$\frac{\langle \Delta E \rangle}{E} \simeq \frac{4}{3}\beta = \frac{4}{3}\frac{V_S}{c} \tag{1.4}$$

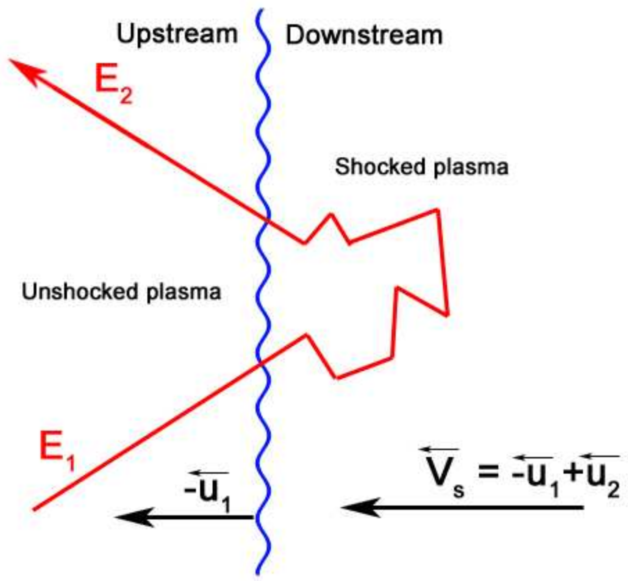

Figure 1.5: Schematic view of the 1^{st} order Fermi acceleration mechanism in the upstream frame.

A consequence of this improved mechanism is that particles always gain energy per *encounter*. This mechanism is called the 1^{st} order Fermi acceleration mechanism.

Actually what happens is a combination of both mechanisms and as a consequence:

- The 1^{st} order acceleration mechanism cannot exit without the 2^{nd} order.
- It is not always true that 2^{nd} order acceleration is less efficient, it depends on the magnetic energy.

The acceleration rate in a 1^{st} order Fermi acceleration is given by:

$$\frac{dE}{dt} \simeq K\frac{u_1^2}{c}ZeB \tag{1.5}$$

where u_1 is the speed of the shock-wave (figure 1.5), Ze is the charge of the accelerated particle, B is the magnetic field and K is a constant ($\sim$0.1). Hillas derived the maximum energy at which a particle of charge Ze can be accelerated [6]:

$$E_{max} \leq \frac{3}{20}\frac{u_1}{c}ZeB(u_1T) \tag{1.6}$$

The accelerator works for a limited time, T, so the distance that the shock-wave travels is $L \simeq u_1T$. Using the time expansion for a typical supernova for a 10 $M_\odot$ ejected at

5×10^8 cm/s, (T ~1000 yrs) and an estimate of $B \sim 3$ μGauss then equation 1.6 gives:

$$E_{max} \leq Z \times 3 \times 10^4 \ \ \text{GeV} \tag{1.7}$$

Therefore, this mechanism is able to describe the primary cosmic ray acceleration up to 100 TeV, however we observe cosmic rays with energies above the knee and beyond the ankle, i.e. 3 EeV. Figure 1.6 is the diagram first produced by Hillas, and gives the relation between the requires magnetic fields to accelerate particles and the dimensions of the astrophysical objects needed to contain the accelerating particle through the acceleration process. The lines give the magnetic field versus the gyroradii for protons (solid) and iron (dashed).

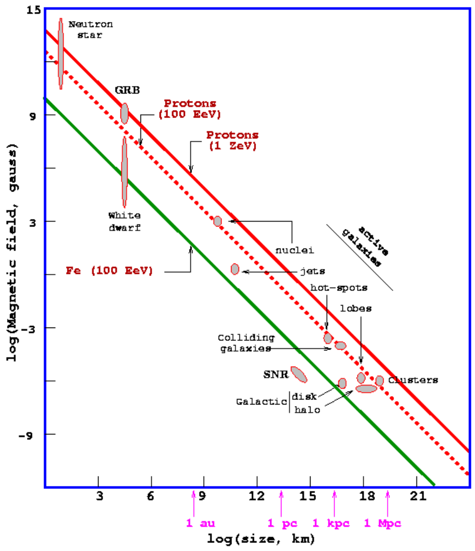

Figure 1.6: Magnetic field strength vs. gyroradii for protons (solid) and iron (dashed). Lines represent plausible limits for 10^{20} eV cosmic ray containment in the sources.

1.1.2 Origin of cosmic rays: Beyond 100 TeV

There are several ideas on how to produce cosmic rays with energies greater than 100 TeV. Even with only the Fermi mechanism worked out we can suggest that those high energy particles are also accelerated in supernova shock–waves, but in those which run through the stellar wind of the predecessor star. With this possibility, energies up to 3 EeV per particle can be reached. The cosmic rays between the ankle and the expected GZK cut-off are explained by many sources, nearly all of them outside our galaxy. Some of them can also explain the events beyond the GZK cut-off. Among these sources, pulsars with very high magnetic fields can accelerate charged particles up to energies of 10^{21} eV. Although there are some problems concerning the adiabatic losses on the way close to the pulsar out to the interstellar gas, if such concept could be proved it would certainly provide an easy explanation of the arriving particles beyond the GZK cut-off. Gamma Ray Bursts (GRBs) constitute other proposed sources, but nowadays we do not know much more about GRBs yet and their contribution to CRs. Another possible sources are radio galaxies which provide giant shock–waves in their *hot spot*. These *hot spots* are in fact huge shock–waves that can even exceed the size of our Galaxy. Not all the aforementioned mechanisms can explain the particles with energy beyond the GZK cut-off. Apart from these astrophysical environments with a *bottom-up* acceleration mechanism, there are others mechanisms suggested in order to explain the acceleration up to GZK energies and beyond. These *top-down* mechanisms involve the decays of super-massive particles such as topological defects (TDs), primordial black holes and other relics formed in the Big Bang. Furthermore, the violation of Lorentz invariance [7] at some very high energy where the four forces of Nature are combined, constitutes a new exciting proposal for those high energy events beyond the GZK cut-off.

1.2 High energy photons and neutrinos

The acceleration mechanisms mentioned above are only valid for charged particles. As regards particles electrically neutral such as photons or neutrinos, the acceleration processes have to be different. In this case, neutral particles are the decay products of accelerated charged particles. One open question concerning the primary acceleration in shock–waves, (in particular inside the jets of the Active Galactic Nuclei) is the kind of particles that are accelerated [8]. The leptonic models consider the acceleration of electrons and positrons producing synchrotron radiation, bremsstrahlung and inverse Compton scattering (see figure 1.7). These models do not predict neutrinos emission.

However, in the hadronic models where protons as well as charged nuclei are accelerated, neutrinos and photons are the decay products of the hadrons produced by the strong interaction of these charged particles with matter. Both processes may coexist in parallel, but one of them may dominate at high energies. If photons with energies larger than 100 TeV exist they can only be explained by means of hadronic mechanisms. However, γ-rays suffer the same problem than CR protons; photons with energies higher than 10^3 TeV only travel distances shorter than 8 Kpc due to the interaction of these high energy photons with the low energy photons of the microwave background. To explore the Universe above distances of 100 Mpc we are constrained to detect photons with energy ≤ 10 TeV. The *Energetic Gamma-ray Experiment Telescope* (EGRET) [9] has measured a considerable number of γ-ray sources with energies up to a few GeV. Figure 1.8 shows the Third EGRET Catalogue for γ-ray sources with energies above 100 MeV. As can be seen in this figure, some of the sources are still unidentified. However, at higher energies ($E_\gamma > 300$ GeV) gamma ray astronomy cannot be performed with satellite experiments due to the low photon fluxes, and is

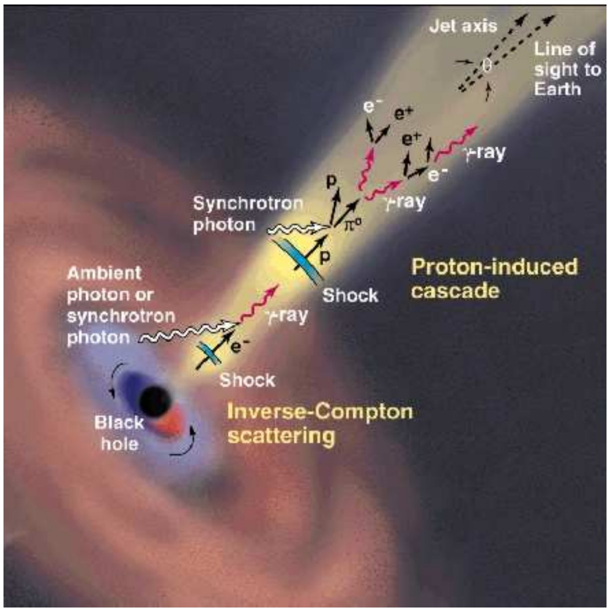

Figure 1.7: Schematic view of the hadronic and leptonic acceleration mechanisms inside an AGN jet.

carried out with ground-based Cherenkov telescopes such as Whipple and HEGRA. Two of the known γ-ray sources above 250 GeV where discovered by the Whipple collaboration [10, 11], they are the galaxies Markarian 421 and Markarian 501, that are at about 100 Mpc away. This is the reason why photons from both galaxies arrive whereas photons from more intensive objects can not reach the Earth and are absorbed along their travel. Neutrinos, on the contrary, can travel without suffering interaction with matter, and they are not deflected by the interstellar magnetic field since they are electrically neutral. The neutrinos sources for the hadronic models previously set out, are the same than for photons.

1.3 High energy Neutrino Astronomy

Neutrino Astronomy can be assumed to be born when the Kamiokande II experiment detected the neutrinos coming from the SN1987A supernova [12] explosion. This is usually called low energy Neutrino Astronomy since these neutrinos are the products of nuclear reactions in stars and in supernova explosions. The low cross-section of this kind of neutrino only allows the observation of objects like our Sun and any supernovas in the Galaxy or galaxies nearby. The high energy Neutrino Astronomy has many advantages over the low energy Neutrino Astronomy:

- The neutrino cross-section is larger at high energy.
- There is also an increase of muon range and angular resolution with energy.

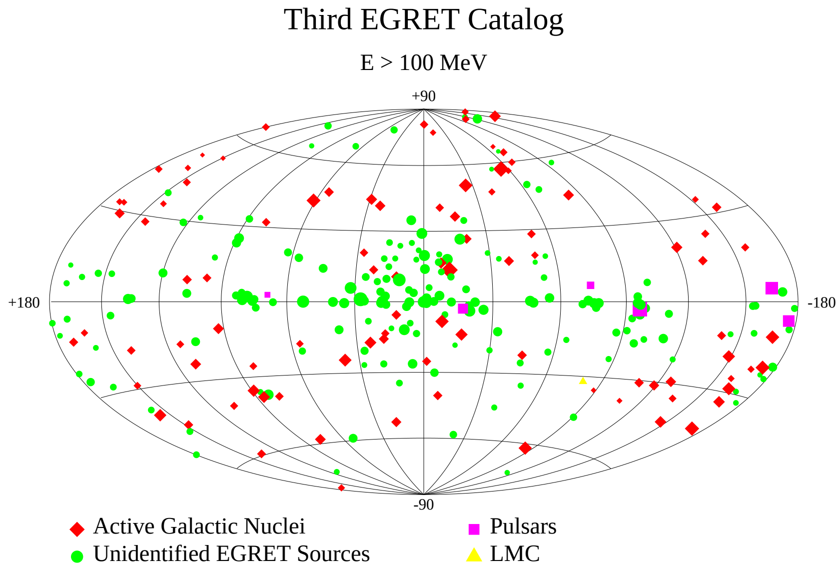

Figure 1.8: Third EGRET catalog for sources above 100 MeV.

- Large volumes of natural media such as water/ice can be used to detect these high energy neutrinos.

High energy Neutrino Astronomy opens a window to study the Universe in conditions never seen before. There are several environments that are assumed to produce measurable neutrino fluxes. In the following sections we will describe the most likely high energy neutrino sources.

1.4 Astrophysical neutrino sources

As mentioned above, neutrinos are mostly expected to be produced in the same scenarios where charged hadronic particles are accelerated. These particles will interact in the surroundings of the astrophysical source giving rise high energy neutrinos as a final product. Since the energy range of CRs spans from subrelativistic to relativistic energies, neutrinos will have also a wide energy range.

1.4.1 Neutrinos from *bottom-up* models

Bottom-up models are those in which neutrinos are produced through the prior acceleration of other particles. As we have seen, there are many astrophysical scenarios in which charged particles can be accelerated to high energies. In all those environments where a flux of accelerated particles exists, neutrinos can be produced through the interaction of these particles with matter.

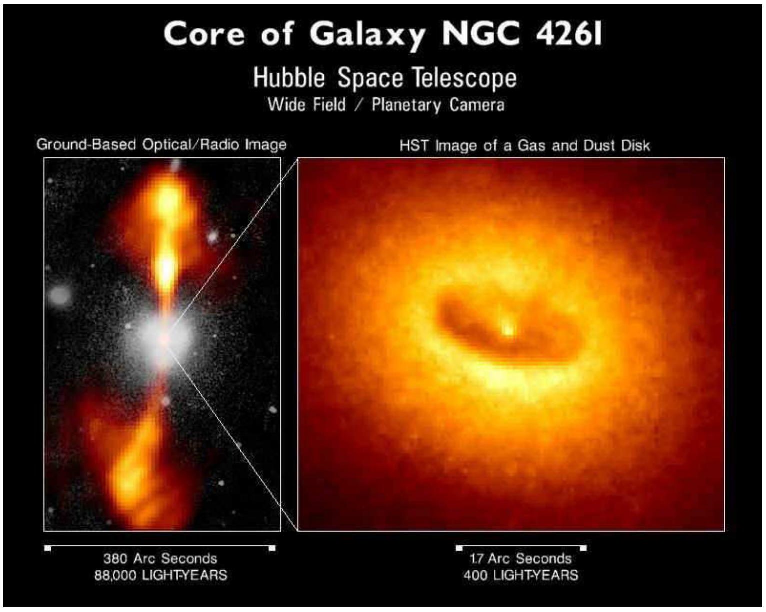

Figure 1.9: Image of the NGC 4261 Active Galactic Nucleus from the Hubble Space Telescope.

- **Active galactic nuclei (AGNs)**

  Active galactic nuclei are galaxies which have a very bright core of emission embedded in their center. This core may be very bright compared to the rest of the galaxy. Models of AGNs concentrate on the possibility of a supermassive black hole which lies at the center of the galaxy. This supermassive black hole ($10^6 - 10^9$ $M_\odot$) would produce material accretion onto it releasing a large amount of gravitational energy. The luminosity measured in these objects can reach 10^{48}erg/s becoming one of the most energetic objects in the Universe. Radio observations of AGNs often show powerful jets, streams of particles or plasma coming from the central source (see figure 1.9). The standard model for AGNs suggests that the phenomenology changes according to the orientation of these jets with respect to us. There is a common inner *engine* model to explain several kinds of AGNs such as Seyfert I and II, Blazards, Quasar, and so on. In particular, Blazards are supposed to be AGNs with one of its jets pointing towards Earth. Models of particle acceleration in those relativistic jets are not well settled, however, speculative models predict accelerated particles up to relativistic velocities and collimated. The neutrino production in AGNs will be a consequence of the hadronic model of particle acceleration. Although there is no evidence of neutrino production there is a direct hint of particle acceleration in the gamma-ray detection by the EGRET satellite.

- **Gamma Ray Bursts (GRBs)**

  They are short lived bursts of gamma-ray and by far the most powerful objects in the Universe. Lasting from a few milliseconds to several minutes they shine hundreds of times brighter than a typical supernova. The γ emission is of the order of $10^{52\pm1}$ erg/s assuming the radiation to be isotropic. So far, GRBs were arguably the biggest mystery in high-energy astronomy. GRBs are likely to be related to the collapse of compact objects, in fact they are supposed to culminate in the creation of a black hole. Recently, there have been proofs of an association between GRBs and supernovas [13]. There are two models that try to explain the GRBs, they are the so-called *fireball* [14] and the *cannonball* [15] models. In the *fireball* model the energy is released by the formation of a black hole when giant stars collapse. Then, an extremely strong electromagnetic field can be formed and this energy could accumulate matter and antimatter, which generates an enormous pulse of energy (*fireball*), expanding with ultrarelativistic velocities with a Lorenz factor $\gamma > 300$. This and the internal shocks between the expanding shells produce the observed burst of γ-rays when the expanding *fireball* ceases to be opaque. A completely different approach from the *fireball* models are the *cannonball* models. This model also assumes a correlation between supernovas and GRBs, in fact after a supernova explosion, in certain conditions a part of the parent star falls back and produces an accretion torus. As a result, relativistic cannonballs are ejected as material collapse in the compact object, and collide with the external expanding shell of the supernova producing the GRB. The advocates of the *cannonball* model argue that this model succeeds in explaining some issues such as the afterglow and the long-duration GRBs that are a problem in the accepted *fireball* models. In both kind of models a hadronic component is expected and therefore, a neutrino flux which would be in the $10^{14} - 10^{16}$ eV energy range.

- **Supernova remnants**

  Supernovas explosions produce a huge amount of neutrinos ($\sim 10^{57}$) that can be detected with the present detectors if they occur in the Galaxy or nearby. However, these neutrinos are not energetic enough ($E_\nu <$ few tens of MeV) to be easily detectable with a neutrino telescope like ANTARES. On the other hand, the supernova explosions have to be placed somewhere in the nearby of our galaxy to be detected. Even though supernova explosions do not occur very frequently (about 2 to 4 supernovas per century in a galaxy like ours), the Kamiokande II and IMB experiments were able to detect the neutrino flux from a supernova explosion taking place in the Large Magellanic Cloud, a galaxy at a distance of about 50 kpc. Well after the supernova explosion, particles can be accelerated in the so-called supernova remnants (SNRs) via the Fermi mechanism in the shock-waves of the expanding shells. If the final product of the supernova is a neutron star, already accelerated particles (protons or any hadronic component) can also suffer additional acceleration due to the strong magnetic fields of the neutron star. More specifically the CANGAROO II experiment has analyzed data from one of the intrinsically brightest sources of γ-rays in the Galaxy, the supernova remnant RX J1713.7-3946 (see figure 1.10). They found that the measured energy spectrum is well fit by models in which the γ-rays are products of π^0 decay generated in *pp* collisions. This γ-ray photons are therefore emitted by a hadronic component, presumably high-energy protons accelerated in the supernova remnant [16]. If it is confirmed, and SNR become one of the most probably source of CRs there would be also a neutrino flux coming from these SNRs. However this claim is controversial [17].

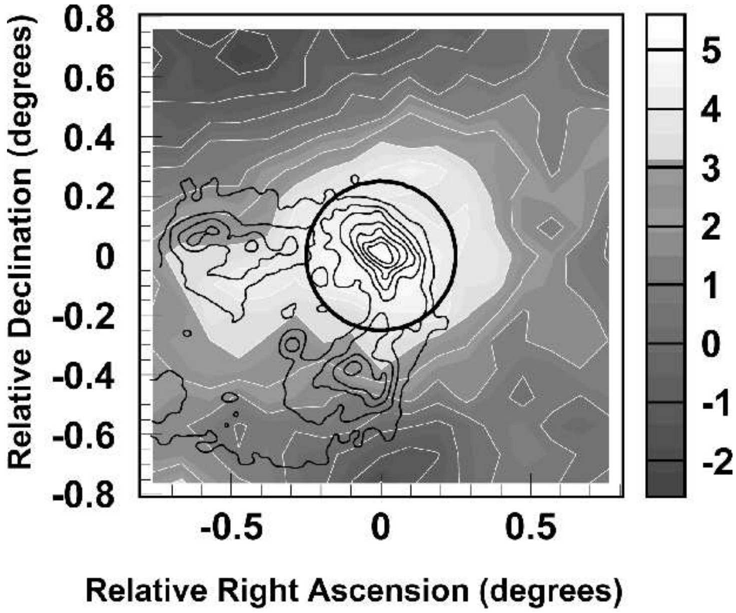

Figure 1.10: Contour map of significance around the NW rim of RX J1713.7-3946 centred at the brightest region in hard X-ray emission.

- **Pulsar wind nebulae (Plerions)**

  This kind of SNRs are also called Crab-like remnants, since they resemble the Crab Nebula (cf. figure 1.11) being this source the youngest and most energetic of them. These SNRs are very similar to the shell-type remnants, except that they hold a pulsar in the middle that blows out jets of very fast-moving material. A number of plerions have been discovered in radio, optical and X-ray bands. Their nature is usually indicated by a center-filled morphology, resulting from the continuous injection of pulsar electrons into the nebula. Radiation observed from plerions (radio, optical and X-ray emission) is believed to be due to synchrotron emission. Hadrons are supposed to play an important role in radiation processes [18, 19]. A simple rescaling of the *gamma-ray* fluxes to the neutrino fluxes has been done by Guetta and Amato [20] for a few pulsar wind nebulae observed. For the Crab nebula, for instance, these results lead to a predicted neutrino flux given (in units of $\mathrm{GeV}^{-1}\ \mathrm{m}^{-2}\ \mathrm{s}^{-1}$) by:

$$\frac{dN_\nu}{dE_\nu} = 1.85 \times 10^{-10} \left(\frac{E_\nu}{10^3 \mathrm{GeV}} \right)^{-2.6} \qquad (E_\nu < 10^5 \mathrm{GeV}) \qquad (1.8)$$

If this simple rescaling is correct, we can ensure that all these Pulsar Wind Nebulae (PWNe) could be detected by a 1 km^2 neutrino detector.

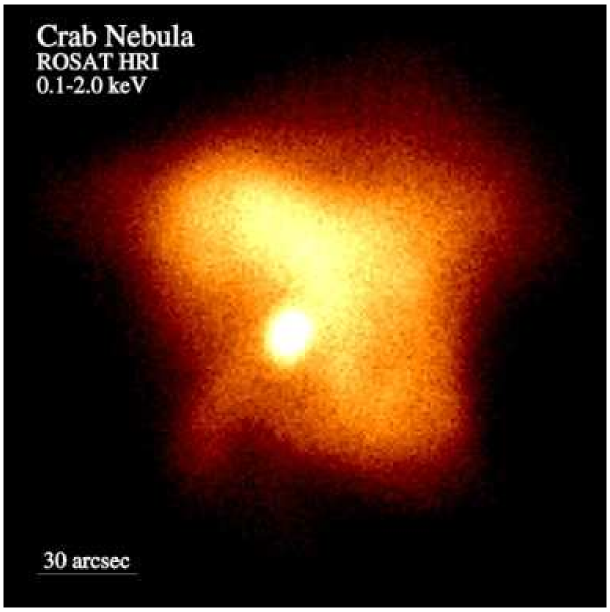

Figure 1.11: X-ray image where both the Crab Nebula and Crab pulsar are clearly visible.

- **X-ray binaries**

  Binary star systems contain two stars that orbit around their common centre of mass. A special class of binary stars are the X-ray binaries stars, so-called because they emit X-rays. X-ray binaries are made up of a normal star and a collapsed star (a white dwarf, neutron star, or black hole). These pairs of stars produce X-rays if the stars are close enough that material is pulled off the normal star by the gravity of the dense, collapsed star. The X-rays come from the area around the collapsed star where the material that is falling toward it is heated to very high temperatures. Neutron stars are known to hold a strong magnetic field (10^{12} G) over their surfaces and a rotation period of milliseconds. Both the matter accretion from the normal star to the neutron star or compact object, and the magnetic dipolar radiation are candidates of acceleration mechanisms of particles.

- **Microquasars**

  Microquasars are Galactic X-ray binary systems, which exhibit relativistic radio jets [21]. These systems are believed to consist of a compact object, a neutron star or a black hole, and a star companion. Mass transfer from the star companion to the compact object through the formation of an accretion disk and the presence of the jets make them similar to small quasars, hence their name "microquasars". The analogy may not be only morphological (see figure 1.12); although there is no obvious scaling, it is common thinking that the physical processes that govern the formation of the accretion disk and the ejection of plasma into the jets are the same for both systems. Local Galactic microquasars may therefore be considered as nearby "laboratories", where models of the distant, powerful quasars can be tested. Microquasars differ in their time behaviour. Some of them, like the SS433 microquasar, are persistent sources, while others appear to be intermittent (GRS 1915+105) or periodic (LS I +61o303). In all cases, however, the observed radiation from microquasar jets, typically in the radio and in some cases also in the IR band, is consistent with non-thermal synchrotron radiation emitted by a population of relativistic, shock-accelerated electrons. In table 1.1 a list of microquasars can be seen with the corresponding expected neutrino flux and figure 1.13 shows the skymap of known microquasars in the galactic centre.

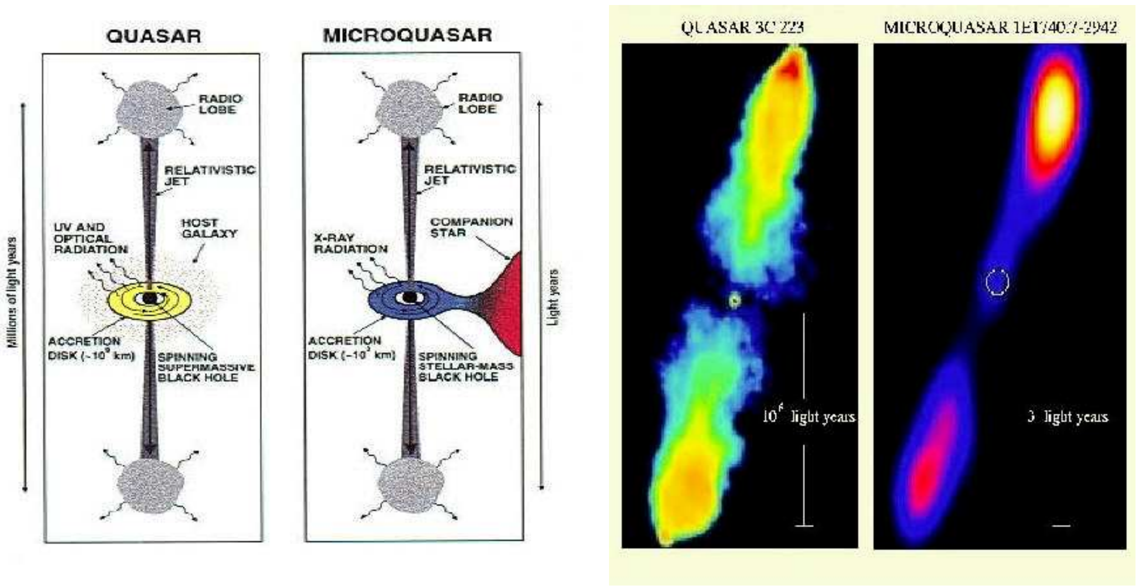

Figure 1.12: Schematic comparison between the morphologies of a quasar and a microquasar (left) and real comparison between the Quasar 3C 223 and the Microquasar 1E 1740.7-2942 (right).

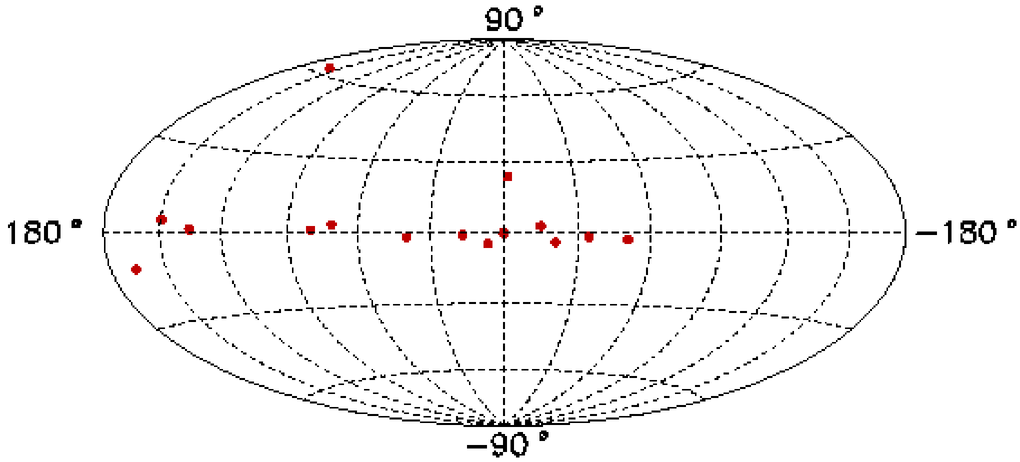

Figure 1.13: Skymap in galactic coordinates of the known microquasars.

- **Magnetars**

  Magnetars are isolated neutron stars with surface dipole magnetic fields much higher than in an ordinary pulsar. Recent observations support the idea that about 10% of neutron stars are born with ultra-high magnetic fields. This may be due to the mass of the progenitor star or the spin that the neutron star gets from the explosion. Such neutron stars sit unnoticed, extremely dim because they have no fuel to burn.

  Gradually, the magnetic field slows down the spin of the neutron star. This slowing-down releases energy, making the star brighter. Additional disturbances in the star's magnetic field and crust (called starquakes) can make it yet brighter. This is when it reaches the magnetar stage. Magnetars manifest themselves in the form of soft gamma ray repeaters (SGRs) and anomalous X-ray pulsars (AXPs). Young fast-rotating magnetars have been recently proposed to be possibly significant TeV neutrino sources [23]. In figure 1.14, the magnetar XTE J1810-197 discovered by NASA's Rossi X-ray Timing Explorer can be seen.

1.4.2 Neutrinos from *top-down* models

Fermi acceleration and in general *bottom-up* models are not enough to explain CRs beyond the GZK cut-off. Extrapolation in energy of the coupling constants suggests that the weak, electromagnetic and strong interactions could be unified at energies of about 2×10^{16} GeV. The "Grand Unified Theories" (GUTs) predict the existence of X particles with mass m_X around the GUT scale of $\simeq 2 \times 10^{16}$ GeV/c^2. If their lifetime is much shorter than the age of the Universe (about the inverse mass $\sim 6.6 \times 10^{-41}$ s) their decays should give rise to ultra-high energy cosmic rays. This can only occurs by emission from topological defects [24]. Topological defects are relics formed in the early phases of the Universe at temperatures close to the GUT scale. Topological defects

Source	F_ν
XTEJ1748-288	3.07×10^{-10}
Cygnus X-3	4.02×10^{-9}
LS5039	1.69×10^{-12}
GROJ1655-40	7.37×10^{-10}
GRS1915+105	2.10×10^{-10}
Circinus X-1	1.22×10^{-10}
XTEJ1550-564	2.00×10^{-11}
V4641Sgr(1)	2.25×10^{-10}
V4641Sgr(2)	3.25×10^{-8}
Scorpius X-1	6.48×10^{-12}
SS433	1.72×10^{-9}
GS1354-64	1.88×10^{-11}
GX339-4	1.26×10^{-9}
GROJO422+32	2.51×10^{-10}

Table 1.1: List of microquasars considered in [22], including the expected neutrino fluencies in units of erg s^{-1} cm^{-2} in a km^2 detector.

are formed between regions that are causally disconnected. Some examples are cosmic strings, magnetic monopoles and domain walls. These topological defects can lead to emission of GUT scale X particles. The X particles can decay into jets of particles whose spectra can be roughly estimated within the Standard Model, having a few percent nucleons and the rest being neutrinos and photons [25].

1.4.3 Other Physics under the scope of ANTARES

There are also several neutrino fluxes estimations that could be measurable and detected in the ANTARES telescope. Most of these speculative sources could be a guarantee of the existence of new and exotic phenomena, or may be the confirmation of models of other hypothetical phenomena.

- **Dark Matter**

  There is an astrophysics evidence that not all the matter in the Universe is luminous. In fact, more than 90% is dark matter. Dark matter has gravitational effects on both the light and the sources of light that can be seen. From this additional gravitation effects, it can be inferred how much mass must be present. The nature of this dark matter is not completely settled, and the candidates proposed range from neutrinos till compact objects such as brown dwarfs or Jupiter-like stars. However, it is known that neutrinos cannot make up all the dark matter due to inconsistencies with the age of the galaxies formation and direct search

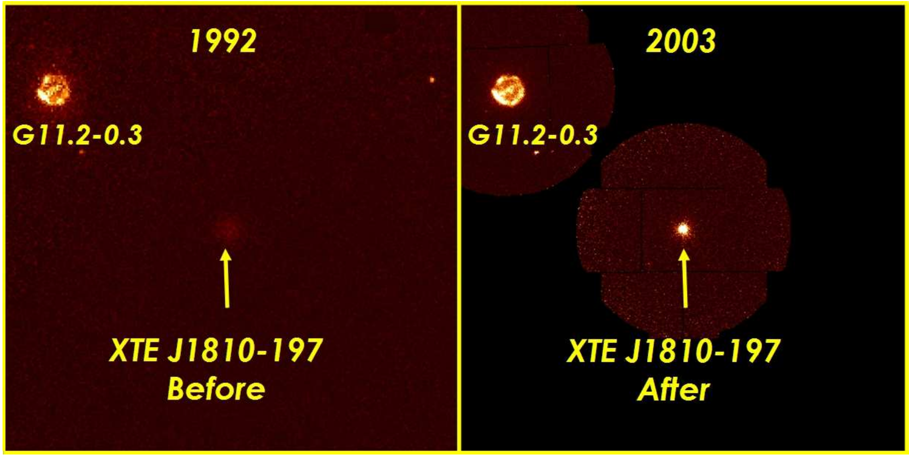

Figure 1.14: An image showing a neutron star before (left) and after (right) the magnetar stage.

of compact objects indicate that these can only be a fraction of the total dark mass. It has been proposed that dark matter is made up with low cross-section particles with masses around the GeV-TeV scales. These particles, so-called weakly interactive massive particles (WIMPs) are predicted by supersymmetric theories. Supersymmetry is a symmetry between bosons and fermions which should be spontaneously broken. The minimal supersymmetric model (MSSM) assumes the existence of a heavier boson *partner* for every fermion, a fermion *partner* for every boson and two Higgs doublets. If the so-called R-parity is conserved, supersymetric particles must be created or annihilated in pairs, so that the lightest supersymmetric particle (LSP) must be stable and all other supersymmetric particles should finally decay to it. This LSP is an excellent candidate for non baryonic dark matter. The identity of the LSP is still not well known, but it is generally assumed to be the lightest neutralino. Neutralinos would suffer the gravitational interaction and would accumulate in the core of massive objects such as the centre of the Sun, the Earth or even the Galactic Center [26]. The density increase would make more likely the neutralino annihilation into a fermion-antifermion pair or into various combinations of W, Z and Higgs bosons. Whereupon, an observable neutrino flux would be produced with a given energy $E_\nu \sim E_{ew}$ (see figure 1.15). Detection of this neutrino flux will be an important step in the determination of the nature of dark matter as well as a proof of the existence of WIMPs as the supersymmetric theories with R-parity conservation predict.

- **Magnetic Monopoles**

  Magnetic Monopoles are a special kind of topological defects. They are basically as electrically charged particles but with short-circuit magnetic fields instead

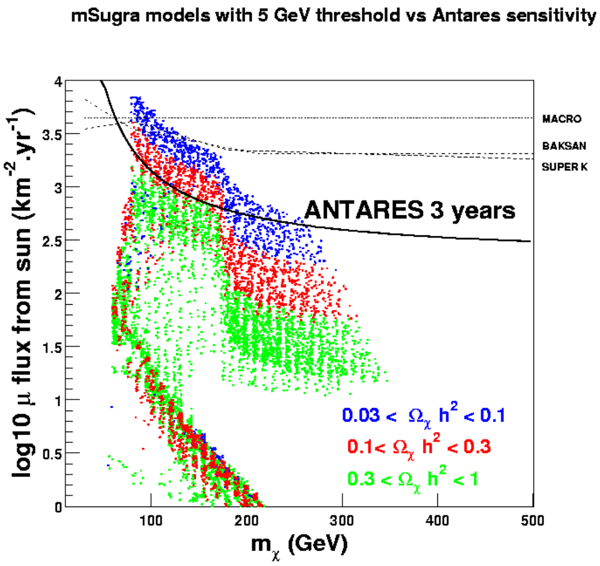

Figure 1.15: Muon flux from the Sun for the ANTARES telescope (3 years) and other experiments and mSUGRA points labelled by Ωh^2.

of electric fields. The universal monopoles flux must be low according to the observations of the permeating magnetic fields in the cosmos. One property of monopoles is that they are accelerated in magnetic fields as charged particles are accelerated in electric fields. In astrophysical strong magnetic fields a magnetic monopole can reach energies of 10^{21} eV or even more. Although there is not well known relation between monopoles and CRs, it has been claimed that ultra high energy cosmic rays could be relativistic monopoles [27]. With a specific trigger in the ANTARES telescope monopoles can be distinguished from the PeV muons. As well as relativistic monopoles, there are slow monopoles, whose track can be detected by the sequential Cherenkov flashes emitted along it. These massive magnetic monopoles would be produced, after the Big Bang and they would be slowed down to velocities $\beta \leq 10^{-3}$.

- **Primordial Black Holes**

  It is also possible that in the early Universe very small black holes were also formed. Black Holes of mass sufficiently small can decay and produce a characteristic spectrum of high energy particles and therefore a source of ultra high energy CRs [28].

- **SUSY Q-balls**

  Neutralinos are not the unique Dark Matter candidate. There are other possibilities bandied about such as SUSY Q-balls. After inflation in a Affleck-Dine

(AD) scenario for baryogenesis [29], fragmentation of the AD condensate will produce Q-balls. These are non-topological solitons with non-zero baryon and lepton numbers. Depending on the parameters of the theory, signal from these Q-balls can be detected.

- **Neutrino Oscillation**

Although the ANTARES telescope is optimized for the search of astrophysical sources, neutrino oscillation studies can also be carried out. Neutrino oscillations were proposed in order to explain the solar neutrino deficit. Some explanations for the solar neutrino problem advocate for non-standard solar models, however the favoured hypothesis is the neutrino oscillation from one flavour to another during their flight from the core of the Sun to Earth. One crucial consequence is that if neutrinos oscillate from one type to another, neutrino are massive particles. If neutrinos have mass they are not necessarily eigenstates of the mass matrix but a linear combination of them:

$$|\nu_\alpha\rangle = \sum_{i=1}^{3} U_{\alpha_i} |\nu_i\rangle \tag{1.9}$$

where $\alpha = e, \mu, \tau$ are the states produced by the weak interaction and $i = 1, 2, 3$ are the eigenstates of the mass matrix. Their composition changes with time. The states at different times ($|\nu_\alpha(t)\rangle$ and $|\nu_\alpha(0)\rangle$) are different mixtures of the mass eigenstates. Therefore, for a given neutrino state at time t=0, the evolution in time follows the equation:

$$|\nu_\alpha(t)\rangle = \sum_{i=1}^{3} U_{\alpha_i} e^{-iE_i t} |\nu_i\rangle \tag{1.10}$$

Therefore, there is a non zero probability that the state α oscillates to the state β. In the case of mixing only two neutrino flavours, the oscillation probability is given by:

$$P_{\alpha\rightarrow\beta}(L) = \sin^2 2\theta \sin^2(1.27\frac{L}{E}\Delta m^2) \tag{1.11}$$

where Δm^2 is the difference of the squared masses given in eV^2, L is the travelled distance in km, E is the neutrino energy in GeV and θ is the mixing angle. The Super-Kamiokande experiment in Japan measured the Solar Muon Neutrino Deficit, constraining the solar neutrino oscillation parameters with 1496 days of data taking [30]. However, it was in 2001 when the Sudbury Neutrino Observatory (SNO) in Canada discovered the strongest evidence yet that solar neutrinos are changing into one another [31]. SNO measured all the neutrino flavours coming

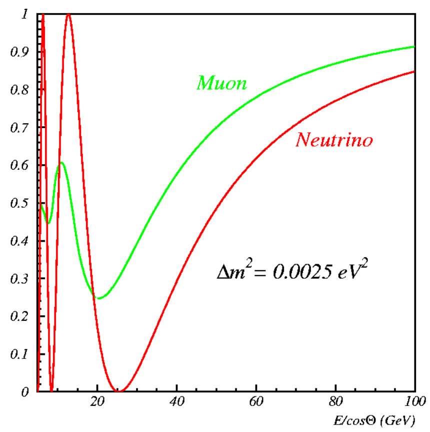

Figure 1.16: Variation of the neutrino survival probability as a function of L/E for $\Delta m^2 = 3.5 \times 10^{-3}$ eV^2 and maximal mixing.

from the Sun, and verified that no deficit was present in the total flux of neutrinos of all flavours.

Change of flavour between neutrinos was also observed in atmospheric neutrinos. Atmospheric neutrinos are induced from the cascade of secondary particles produced by cosmic rays hitting the atmosphere of the Earth. Although the original cosmic ray flux is not known with precision, the ratio of the produced muon neutrinos to electron neutrinos can be predicted to be 2, to a good accuracy. Super–Kamiokande has also measured a signature of neutrinos flavour change in atmospheric neutrino oscillation [32]. Figure 1.16 shows the survival probability for $\Delta m^2 = 3.5 \times 10^{-3}$ eV^2 and $\sin^2 2\theta = 1.0$ values. In figure 1.17 it can be seen what ANTARES may contribute in the search of atmospheric neutrino oscillations.

The main goal of the ANTARES detector is not the study of the neutrino oscillations. Nevertheless, it can be a useful tool since the sensitivity coincides in energy range with the first survival probability minimum. Tau neutrinos can also contribute to the physical background if the oscillation $\nu_\mu \to \nu_\tau$ exists. These tau neutrinos, however, can be detected as signal at very high energies since high energy tau neutrinos ($E_\tau \gg 100$ TeV) can produce tau leptons and these will decay again to tau neutrinos of lower energy that will be less likely to be absorbed since they will be less energetic.

- **New phenomena**

  The opening of a new window in the observation of the Universe can also bring some exciting new discoveries. The possibility of the existence of other neutrino sources in addition to those predicted can not be rejected.

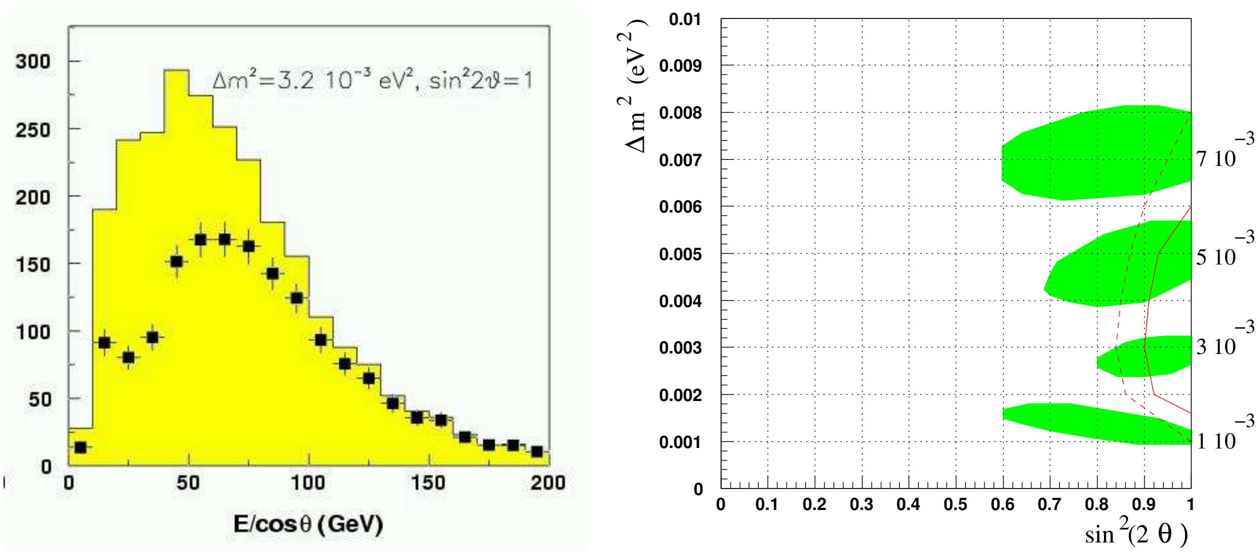

Figure 1.17: Left: Distribution of the $E_{\mu}/\cos\theta$ that ANTARES will see after 4 years of data taking assuming Δm^2=3.2×10^{-3} eV^2 (points). The histogram is for non oscillation. Right: ANTARES 90% CL measurements regions for maximal mixing and four different values of Δm^2. Super–Kamiokande allowed regions (99%CL solid line, 90% CL dashed line) are also shown.

1.5 The neutrino telescope

Since the aim of this research work lies in the study of how the telescope performances can be improved by the re-arrangement of its string design, a description of the detection principle is given in the following sections. On the other hand, a more technical description of the telescope and its performances will be presented in the following chapter.

1.5.1 Detection principle

In 1960 Markov proposed a method to detect astrophysical neutrinos [33]. This method is based on the detection of the Cherenkov light emitted by leptons produced by neutrino interactions with matter while crossing the Earth. The Cherenkov light is emitted provided that the leptons travel through a suitable optical medium such as water or ice. For this reason the detector has to be placed under water, taking also advantage of the shading effect on the secondary CRs. The standard detection in the ANTARES telescope will take place through the muon neutrino interaction with nuclei by charged currents:

$$\nu_{\mu}(\overline{\nu}_{\mu}) + N \longrightarrow \mu^{-}(\mu^{+}) + X \tag{1.12}$$

Neutrinos can also be detected by the electromagnetic or hadronic cascades they produce. Electron neutrinos can produce electromagnetic showers via the charged current interaction and all neutrino flavours can give rise to hadronic cascades via the neutral current interaction. Charged current interactions of ν_τ can also produce events with cascades when the produced τ decays inside the detector into an electron ($\sim 18\%$) or into mesons ($\sim 64\%$). Even though the angular resolution and effective volume are worse for cascade events than for muon events, their energy measurement and separation from background are rather good. Moreover, the detection of all neutrino flavours allows a wider physics scope. The expected neutrino flavour ratios at the source from pp or $p\gamma$ collisions are $\Phi_{\nu_e} : \Phi_{\nu_\mu} : \Phi_{\nu_\tau} = 1 : 2 :< 10^{-5}$ and therefore tau neutrino are not expected to be copiously produced in astrophysical sources. But on the other hand, taking into account the presence of neutrino oscillation, the predicted rates by different models should vary. According to the best fits oscillation parameters these flavour ratios are expected to transform into 1:1:1 along distances $\geq$ kpc [34]. The topologies induced by ν_τ and ν_e are different from ν_μ induced events and hence have different detection efficiencies. As just mentioned, ANTARES is optimized for muon neutrino detection. Most of the muon neutrinos will cross the Earth without suffering any interaction. However, a small fraction of this neutrino flux will interact with the matter surrounding the detector. As a result, a muon will be produced and travel across several kilometres of matter before being stopped. The neutrino cross-section of the deep inelastic charged current interaction is given by [35]:

$$\frac{d^2\sigma_{\nu N}}{dxdy} = \frac{2G_F^2 m_N E_\nu}{\pi} \frac{M_W^4}{(Q^2 + M_W^2)^2}[xq(x,Q^2) + x(1-y)^2\overline{q}(x,Q^2)] \tag{1.13}$$

where $x = Q^2/2m_N(E_\nu - E_l)$ and $y = (E_\nu - E_l)/E_\nu$ are the so-called *scale variables* or *Feyman-Björken variables*, Q^2 is the square of the momentum transferred between the neutrino and the lepton, m_N is the nucleon mass ($N = (n+p)/2$), M_W is the mass of the W boson, and G_F is the Fermi constant.

Figure 1.18 shows the neutrino and antineutrino cross–sections at high energies. As can be seen at low enegies the neutrino cross–section rises linearly with E_ν:

$$\sigma^{\nu N}/E_\nu \simeq (0.677 \pm 0.014)10^{-38} \ \ \mathrm{cm}^2/\mathrm{GeV} \tag{1.14}$$

$$\sigma^{\overline{\nu} N}/E_\nu \simeq (0.334 \pm 0.008)10^{-38} \ \ \mathrm{cm}^2/\mathrm{GeV} \tag{1.15}$$

For energies exceeding about 10^4 GeV, the cross-section is damped by the W–boson propagator. For higher energies, there is a dependence on the shape factor and the transferred momentum. For 10^{16} eV $\leq E_\nu \leq 10^{21}$ eV the cross–sections, according to CTEQ4 parton distributions [36], are given within 10% by:

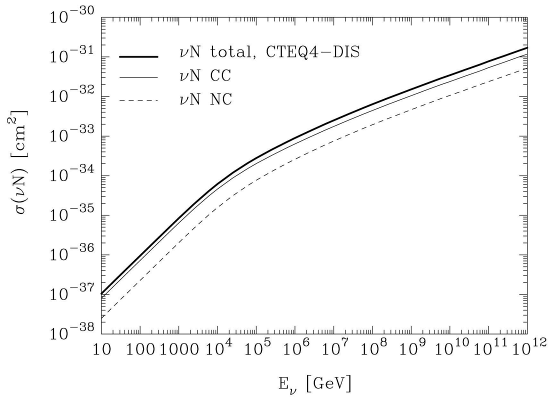

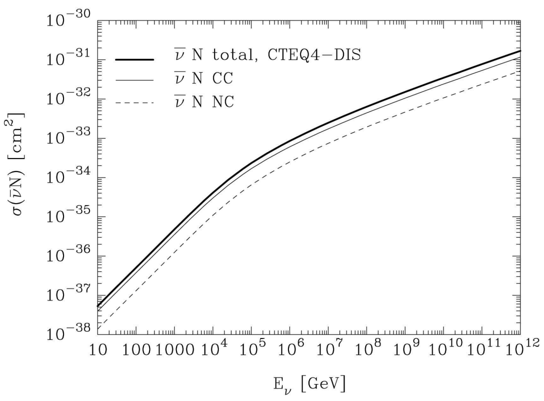

Figure 1.18: Cross-sections for $\nu_l N$ (left) and $\overline{\nu}_l N$ interactions (right), according to the CTEQ4-DIS parton distributions.

$$\sigma^{\nu N} = 5.53 \times 10^{-36} \ \text{cm}^2 \left(\frac{\text{E}_\nu}{1 \text{ GeV}} \right)^{0.363} \tag{1.16}$$

$$\sigma^{\overline{\nu} N} = 5.52 \times 10^{-36} \ \text{cm}^2 \left(\frac{\text{E}_\nu}{1 \text{ GeV}} \right)^{0.363} \tag{1.17}$$

The angle between the incident neutrino and the outgoing muon on the energy depends by the following formula [37]:

$$\overline{\theta}_{\nu-\mu} \simeq \frac{0.7^\circ}{(E_\nu(\text{TeV}))^{0.6}} \tag{1.18}$$

This expression also takes into account the deviation of the muon due to multiple scattering. As can be seen in figure 1.19 this difference decreases with increasing neutrino energy.

The muon energy losses are due to several processes such as ionization, pair production, bremsstrahlung and δ-rays. Up to $\sim$ 600 GeV the energy loss is dominated by ionization and can be considered constant. At higher energies the other stochastic processes of energy loss become more significant and this can be assumed to depend linearly on energy:

$$-\frac{dE_\mu}{dx} = a_{ion} + (b_{brems} + b_{pair} + b_{n.r.})E_\mu \tag{1.19}$$

The energy response of the detector will require different techniques in different energy ranges depending on which process of energy loss dominates in a given energy range. The determination of the muon energy and the direction and therefore of its parent neutrino justify the name "telescope" for a detector like ANTARES. The muon track

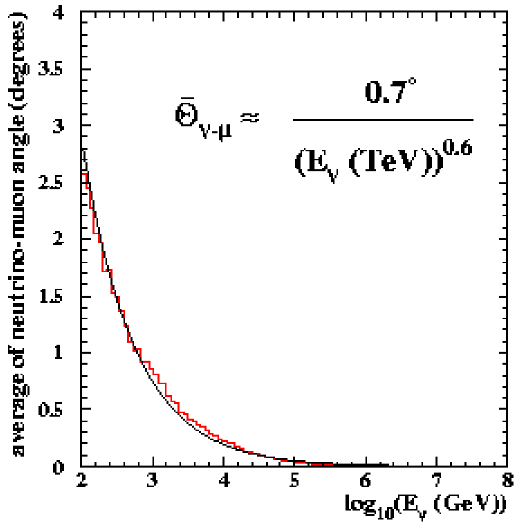

Figure 1.19: Angular difference between the initial neutrino direction and that of the muon track at the detector; the functional form shown (solid curve) reproduces well the observed (histogram) energy dependence.

is detected by means of the Cherenkov light emission by the muon crossing the water with a velocity higher than the light speed in water. The threshold for the Cherenkov emission is given by $\beta \geq 1/n$, where β is the natural muon speed and n is the refractive index of water. For a higher value of β a fraction of the energy of the muon is emitted by means of a coherent electromagnetic radiation emission. This Cherenkov light is emitted with a constant angle with respect to the particle track.

$$\cos\theta_C = \frac{c/n}{\beta c} = \frac{1}{\beta n} \tag{1.20}$$

Concerning the ANTARES situation, taking $n = 1.346$ as the refraction index of water [38], for $\lambda = 450$ nm (which is the wavelength with the longest absorption length in water) and for relativistic particles ($\beta \approx 1$), the Cherenkov angle is $\theta_C \simeq 43°$. The spatial distribution of the emitted photons is given by:

$$\frac{d^2N}{dx d\lambda} = \frac{2\pi}{137\lambda^2}\left(1 - \frac{1}{n^2\beta^2}\right) \tag{1.21}$$

where λ is the wavelength given in nanometres. From this formula is easy to see that shorter wavelengths will contributed more significantly. However, taking into account the light absorption by water and the detector acceptance, some wavelengths will be strongly suppressed. The sensitivity of the detector as a function of the light

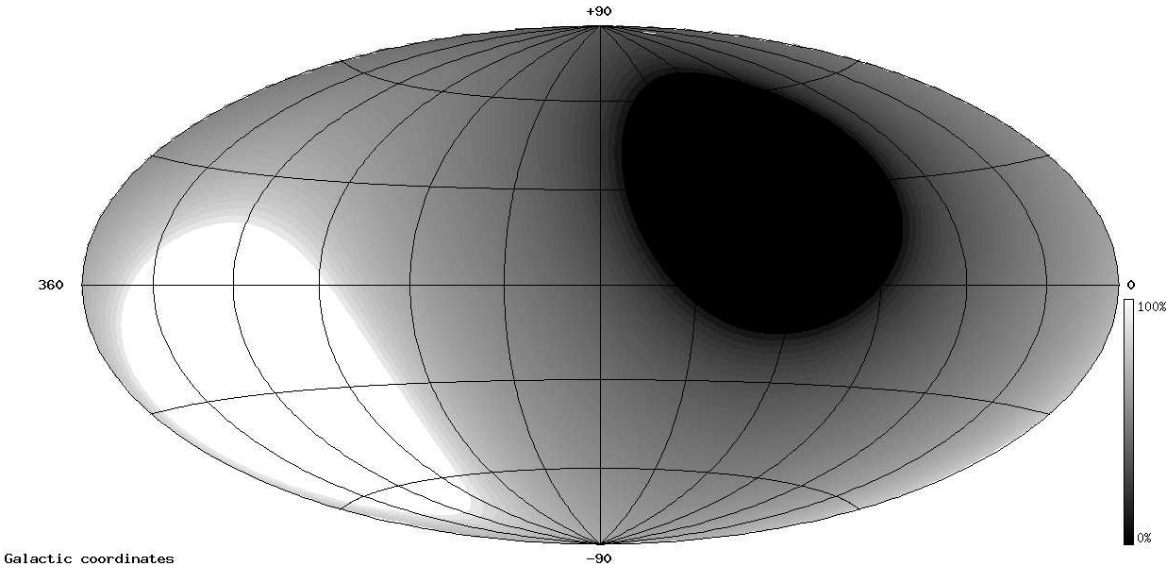

Figure 1.20: Visibility skymap of the ANTARES detector. Dark areas are not observed whereas white areas are visible 24 hours.

wavelength is a convolution of the effect of Cherenkov emission, light absorption in water, transmissivity of the pressure resistant glass spheres and the response of the PMTs as a function of the wavelength.

1.6 Background and signal. Expected fluxes

The ANTARES telescope will be located at 43° of North latitude [1]. For that reason ANTARES can observe most of the sky (about 3.5π sr) due to the Earth's rotation. In the figure 1.20 the dark area corresponds to declinations higher than 47° that are never observed by the ANTARES telescope, whereas the completely white zone in the skymap is visible the 24 hours.

In the previous section, an overview of the general neutrino sources has been presented. These neutrino sources will produce a detectable muon flux, however only a fraction of the total muon flux that arrives to the detector is a meaningful physics signal, the rest will be part of the background, whose rejection will be more or less difficult depending on its nature.

[1] The exact coordinates of ANTARES are (42°50' N, 6°10' E)

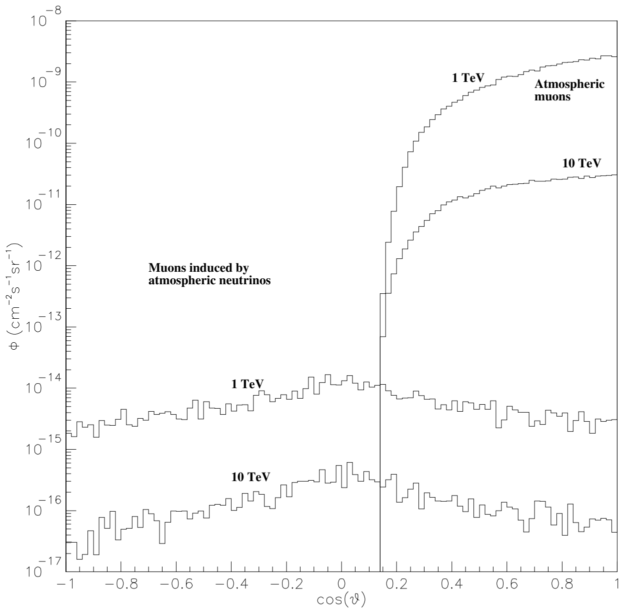

Figure 1.21: Atmospheric and neutrino induced muon flux dependence on the zenith angle.

1.6.1 Physical background

We call physical background –as opposed to other types as the backgrounds due to bioluminescence or to the decay of radioactive salts– that due to high energy particles that leave a signal in the detector. There are two sources of this kind of background. CRs interact in upper layers of the atmosphere, these interactions produces a secondary shower of cosmic rays. Among the secondary cosmic rays, there are horizontal or up-going muons produced by atmospheric neutrinos that have partially or fully crossed the Earth. These neutrinos will interact producing a muon particle just as if they were signal neutrinos. These atmospheric neutrinos are produced following these reactions:

$$\begin{aligned} p \longrightarrow \pi^+(+K^+\cdots) \longrightarrow \quad & \mu^+ + \nu_\mu \\ & \downarrow \\ & e^+ + \bar{\nu}_\mu + \nu_e \\ n \longrightarrow \pi^-(+K^-\cdots) \longrightarrow \quad & \mu^- + \bar{\nu}_\mu \\ & \downarrow \\ & e^- + \nu_\mu + \bar{\nu}_e \end{aligned} \tag{1.22}$$

Figure 1.21 shows muon fluxes induced by the atmospheric neutrinos and the direct muon fluxes as a function of the zenith angle. In general, the flux of neutrinos coming from meson decays can be expressed as:

$$\frac{dN_\nu}{dE_\nu} = \frac{N_0(E_\nu)}{1 - Z_{NN}} \left(\frac{A_{\pi\nu}}{1 + \frac{B_{\pi\nu} cos\theta E_\nu}{E_\pi^C}} + 0.635 \cdot \frac{A_{K\nu}}{1 + \frac{B_{K\nu} cos\theta E_\nu}{E_K^C}} + ... \right) \tag{1.23}$$

The first term of the sum represents the neutrino contribution from pion decays, the second from kaons meson decays and so on. Where $A_{\pi\nu} = Z_{N\pi}(1-(m_\mu/m_\pi)^2)^\gamma/(1+\gamma)$, and similarly for the kaon term, $A_{K\nu}$ but with kaons values instead of pions. $B_{\pi\nu}$ is a constant that depends on the absorption length of muons and pions. E_i^C, where $i = \pi, K....$, is the characteristic meson energy and represents the competence between the absorption process and the decay process. If $E_\nu \ll E_i^C$ then every parent meson will decay, and the atmospheric neutrino spectrum will be parallel to the primary CRs. If $E_\nu \gg E_i^C$ the parent meson will interact and the power-law of the spectrum will increase a power of E. Some of these characteristic energies are $E_{\pi^\pm}^C \approx 155$ GeV, $E_{K^\pm}^C \approx 850$ GeV, $E_{D^\pm}^C \approx 4 \times 10^7$ GeV. In fact, neutrinos coming from the semileptonic decay of very short-lived charmed particles like D mesons –called *prompt neutrinos*– are important since their spectrum is similar to the primary spectrum of CRs, and dominate the atmospheric neutrino flux at high energy (typically above 10^5 GeV).

Atmospheric neutrinos are an irreducible background component, since they cannot be distinguished from extraterrestrial neutrinos. However, at high energies this flux (according to Bartol model [39]) is lower than the expected neutrino flux produced by astrophysical sources (see figure 1.22).

The other type of background are down-going muons also induced by these primary cosmic rays interactions following the reactions described above. Figure 1.21 shows the atmospheric muon flux compared with respect to the muon flux due to atmospheric neutrino flux. These direct atmospheric muon flux is strongly absorbed by the Earth, so only down-going muons are expected. It is a flux six orders of magnitude greater than that induced by the atmospheric neutrinos. Fortunately, due to the strong dependence of this direct muon flux with the zenith angle, they are easily rejected if we consider only up-going events. However, muons arrive sometimes at the detector in groups of several parallel muons induced in the same atmospheric shower. These packets known as *muon bundles* can lead the reconstruction software into an error by reconstructing these events as an up-going event instead of down-going muons bunches. The sea water above the telescope acts as a shield for this background.

1.6.2 Physics signal

As mentioned above, at high energies ($E_\nu \geq 10$ TeV) the atmospheric neutrino flux is lower than the neutrino fluxes predicted by several models of high energy cosmic neutrinos. In figure 1.22, the number of events expected in ANTARES in one year from the atmospheric neutrino flux (Bartol model) is compared with respect to the number of events predicted by several models for a diffuse flux of cosmic neutrinos.

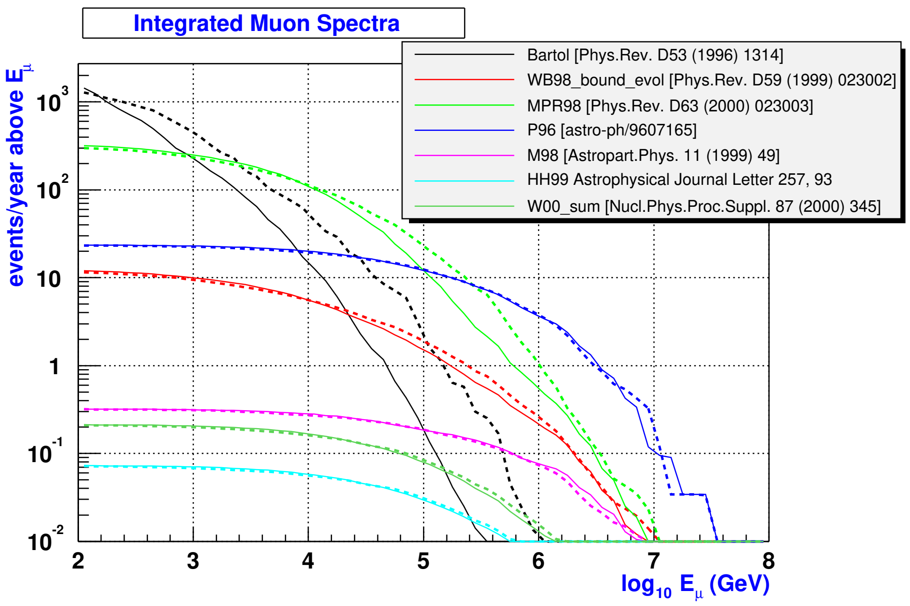

Figure 1.22: Integrated rate of predicted muon events (solid lines) and reconstructed ones (dashed lines) versus generated and reconstructed E_μ for the atmospheric neutrino flux (Bartol model) and several models of diffuse flux of cosmic neutrinos.

For galactic sources the number of neutrinos emitted per unit of time and energy decreases as a power of the energy:

$$\frac{d^2N_\nu}{dE_\nu dt} = AE_\nu^{-\gamma} \tag{1.24}$$

with a spectral index $\gamma \approx 2$ according to the observations of γ-rays below 10 GeV. The source luminosity is related to the normalization factor A, by means of the following expression:

$$\mathcal{L}_\nu = \int_{E_0}^{E_C} \frac{d^2N_\nu}{dE_\nu dt} E_\nu dE_\nu = \epsilon \mathcal{L}_p \tag{1.25}$$

being $\mathcal{L}_\nu$ y $\mathcal{L}_p$ the luminosities for a neutrino and proton source integrated between the minimum energy E_0 and the cut energy E_C. And ϵ is the ratio between the neutrino luminosity and the proton luminosity. The neutrino flux for a source situated at a distance D from the detector is given by:

$$\frac{d\Phi_\nu}{dE_\nu} = \frac{A}{4\pi D^2} E_\nu^{-\gamma} \tag{1.26}$$

and the muon flux for the same distant source with a luminosity $\mathcal{L}_p$ and a ratio of

Model	$E_\mu > 10\ TeV$	$E_\mu > 1000\ TeV$
Bartol [39]	12	0.15
WB98 [43]	5	1.4
MPR98 [44]	102	11
P96 [40]	20	12
M98 [41]	0.3	0.2
HH99 [42]	0.06	0.03

Table 1.2: Expected number of up-going induced muons per year predicted by several models for a 10-string detector.

neutrino luminosity given by ϵ is:

$$N_S = \Phi_0 \left(\frac{1\text{kpc}}{D}\right)^2 \left(\frac{\epsilon}{0.1}\right) \left(\frac{\mathcal{L}_p}{10^{38}\text{ergs}^{-1}}\right) ST \tag{1.27}$$

where Φ_0 is the reference values calculated by Monte Carlo simulation and where S and T are the detector effective area and the time exposure respectively. Even when a point-like source is not detected individually, it contributes to the neutrino diffuse flux formed by all sources emitting together. There are several models for the diffuse neutrino flux assuming that point-like sources are distributed according to a given density and their luminosities follow a certain luminosity distribution. Table 1.2 contains the number of muon events per year (rate) expected for a 10 TeV and a 100 TeV cut on the simulated and reconstructed muon energy. Various *signal* models are considered including the upper limits by Waxman–Bahcall and Mannheim, and the more optimistic by Protheroe and Rachen, both of them valid for sources from which nucleons escape (see figure 1.22). The Bartol atmospheric neutrino flux does not include, for the moment, the contribution of prompt neutrinos from charmed meson decay. The models P96 [40] and M98 [41] are models for neutrinos emitted in the AGN scenario. For GRBs the model considered is HH99 [42].

Chapter 2

The ANTARES telescope

The ANTARES collaboration [37] aims to build an undersea neutrino telescope. The telescope design is constrained by several factors, mainly the environmental conditions at the site, which influence the mechanical structure of the detector and the expected background rates. Nevertheless, extensive studies have been done concerning these essential points in the telescope construction (water optical properties, biofouling, bioluminecence, etc.) ANTARES will consist of a tridimensional array of around one thousand photomultipliers in a surface smaller than 0.1 km^2. This detector is expected to provide useful information in the path to build a km^3 detector under the sea.

2.1 The telescope design

The detector will be located near the coast of the south of France, at about 20 nautical miles from Toulon (42°50′N, 6°10′E) and at a depth of 2500 m (see figure 2.1). This location benefits from the proximity to the coast and to the infrastructures of the French Research Institute for Exploitation of the Sea (IFREMER) that lends their installations and facilities located in La Seyne.

As mentioned above, the telescope design is important in order to optimize the efficiency of the detector. The detector will consist of a tridimensional array of photomultipliers to detect the Cherenkov light emitted by the muons crossing the water surrounding the detector. This array will be formed by 12 flexible strings (also called lines) anchored to the seabed that will stay vertical and taut by a buoy located in the upper end of the string. This research work considers the possibility of increasing the number of lines from 10 to 12 but preserving the total number of PMTs. The strings are spread over an area of about 0.1 km^2 and with an active height of about 0.3 km. Figure 2.2 shows a schematic view of the ANTARES detector with some of the main components labelled. Several criteria have been taken into account to optimize the detector features. The requirements to carry out the three main topics of its scientific program are different [45]. The observation of astrophysical sources above the atmospheric neutrino background requires a threshold of ~ 1 TeV. The threshold for neutralino search is ~ 25 GeV and extends to tens of TeV at most. Neutrino oscillation

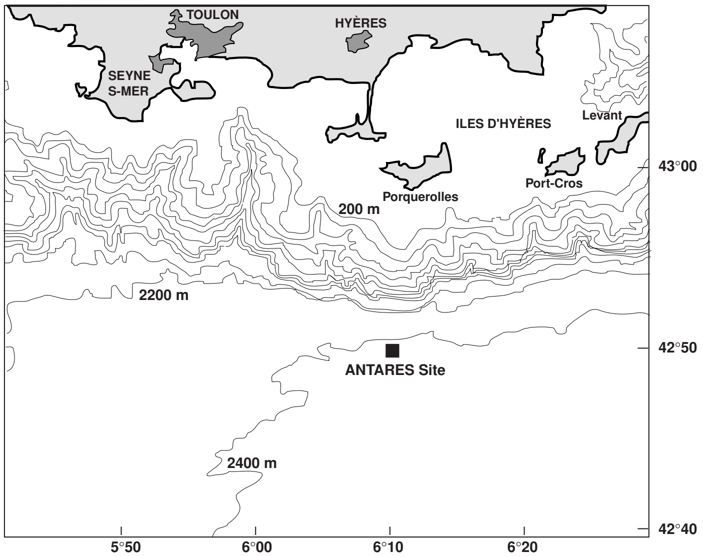

Figure 2.1: Location of the ANTARES site near the south of France.

(although it depends on Δm^2) is expected to be best performed at few tens of GeV. The ANTARES telescope is optimized for the 100 GeV to 1 PeV energy range. As we will see below, a larger spacing among the lines means a higher energy threshold, whereas a shorter distance between lines would decrease the energy threshold and the detector would be optimized for low energies. In this sense, for a fixed number of strings, the energy threshold and the total surface covered are inversely correlated.

2.2 Detector elements

- **The Optical Modules**

  The photomultipliers (PMTs) used in the ANTARES telescope are the 10-inch Hamamatsu photomultiplier tubes R7081-20. These PMTs are housed in a pressure-resistant glass sphere which can withstand pressures up to 700 bars. These glass spheres also hold other elements such as the associated electronics. There is also an internal LED to monitor the transit time of every PMT. The binding between the PMT photocathode and the pressure-resistant sphere is done with a silicon gel that ensures the proper optical coupling ($n_{gel} = 1.40, n_{glass} = 1.48, n_{water} = 1.35$). All these elements are shielded from the Earth magnetic field by means of a *μ-metal* cage and form the basic unit known as an *Optical Module* (OM). In figure 2.3 the cross section view of the OM as well as a picture of a full OM can be seen.

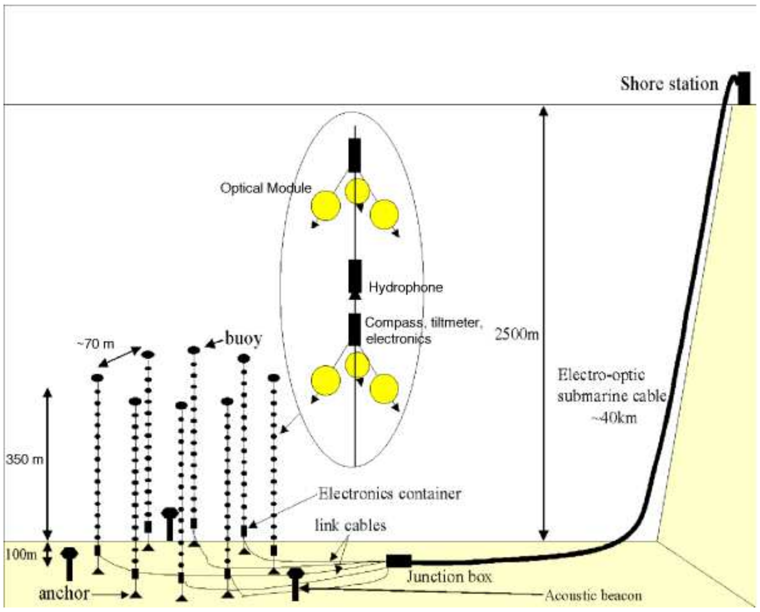

Figure 2.2: Schematic view of the ANTARES detector at the seabed.

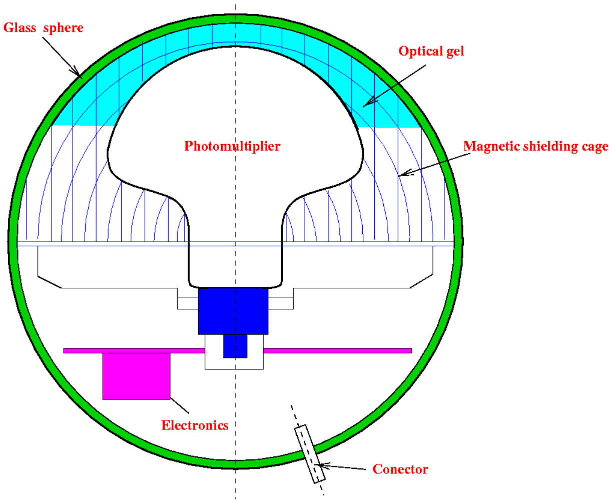

Figure 2.3: Schematic view of an Optical Module (left) and a real Optical Module (right).

- **Storeys and Local Control Module**

  The OMs are gathered in groups of three modules in a *storey* and interconnected via an electro-mechanical cable. The three OMs in each storey are pointing downwards with an angle of 45° with respect to the horizontal line as it is shown in figure 2.4 left. This storey also houses a container for the electronics called the *Local Control Module* (LCM). The electronics includes a digital electronic circuit called ARS (Analogue Ring Sampler) which captures and stores waveforms, pulse heights and timing information, as well as the HV power supply for the photomultiplier tubes and the network nodes for data transmission and slow control. The digitisation performed by the ARS is triggered when the voltage crosses a certain threshold (about 0.3 photo-electrons).

- **The lines**

  The strings are not rigid but flexible. This will avoid breaks due to mechanic tension during the deployment of the strings. The storeys will be placed along the string. The strings hold 25 storeys. A group of five storeys defines a *sector*. Some of the storeys also hold *Optical Beacons* that will allow the timing calibration with external sources. The active part of the strings starts at about 100 metres above the seabed in order to avoid the sea mud and dirt that can be dug up due to the underwater currents. The same underwater currents will cause the strings to rotate and oscillate. Given that the position of the OM has to be known with an accuracy of $\sigma < 20$ cm, there is also a positioning system formed by commercial tilt-meters, compasses and hydrophones that give in real time the relative position of all OMs in the detector and with respect to the four acoustic beacons that will be placed surrounding the detector. In figure 2.4 right, there is a schematic view of a string.

  Apart from the LCM housed in each storey, each string is instrumented with an electronics container in the base called *String Control Module* (SCM). A prototype sector line (PSL) was successfully deployed in 24 December of 2002

- **The Junction Box**

  Each SCM is connected to the *Junction Box* (JB). This is likewise connected with the submarine electro-optical cable that links the strings to the shore station *Institute Michel Pacha* (~ 40 km) where the data will be filtered and processed. The JB also receives the power supply from the shore station and distributes it to the strings. The data, clock and control signals are also sent through the JB via a 1 Gb optical Ethernet link. A high bandwidth is needed since rates of about 70 kHz per PMTs are expected, which results in a data rate of about 625 Mb/s for each line. The JB is protected by a titanium structure housed in a frame which provides stability in the sea bed (see figure 2.5).

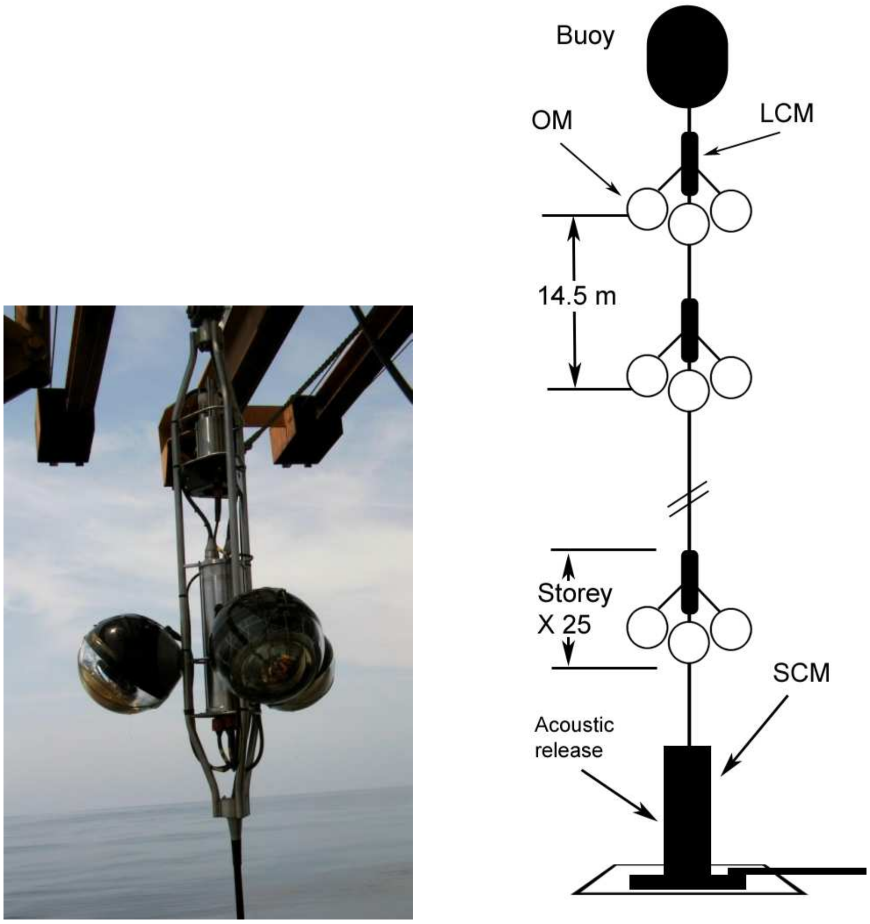

Figure 2.4: Picture of a storey while being deployed (left) and a schematic view of a line (right).

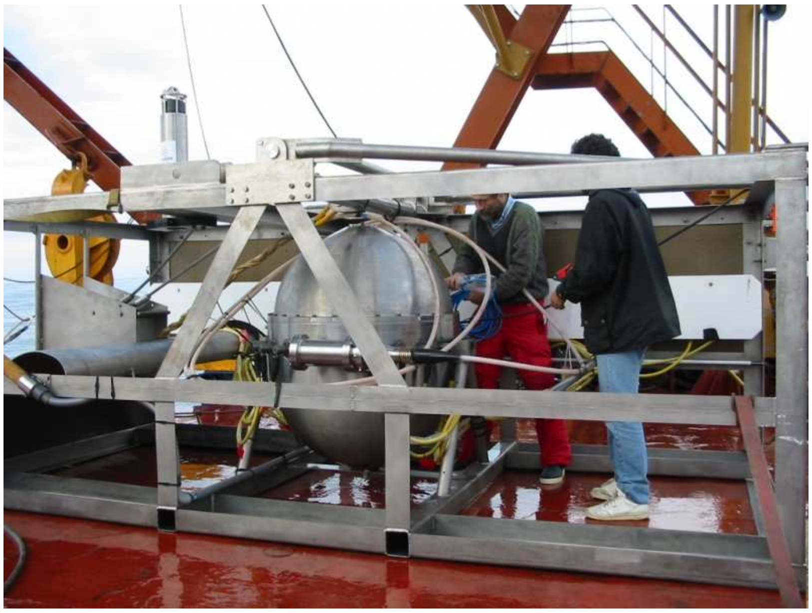

Figure 2.5: Picture of the Junction Box on board of the ship Castor ready for being deployed.

2.3 The PSL and the MIL lines

A sector (one fifth) of a standard line was successfully deployed in December 2002. This *Prototype Sector Line* (PSL) was meant as a *mini-detector* test in real conditions before starting the mass production of the whole detector. Once the PSL was deployed it was linked to the JB that was already in place since December 8 of 2002. The connections were made by means of the Nautile, a bathyscaph lent by the oceanographic institute IFREMER (figure 2.6). Both the deployment and the connection were successful. Together with the PSL, an instrumentation line was deployed in February 2003. This *Mini Instrumentation Line* (MIL) contains the main devices for calibration and environmental parameter monitoring. These instrumentation devices include a seismograph, the acoustic detection system, one LED Beacon in one of the storeys and a Laser Beacon at the bottom of the line, which will allow the timing calibration of the detector. In figure 2.7, a scheme of both lines is shown. The recovering of the MIL and the PSL took place in May and July 2003 respectively, and it was checked that most of the components for both lines had worked properly. However, some problems were found, a fault in the string cable made impossible the reference clock signal distribution, that only reached the String Control Module. The problem was caused by a faulty protection of the fibres of the mechanical cable supplied by the manufacturer. Due to this mishap, it was not possible to determine the relative photon arrival time, and therefore to measure as planned atmospheric muons. Only counting rate and optical background measurements were performed.

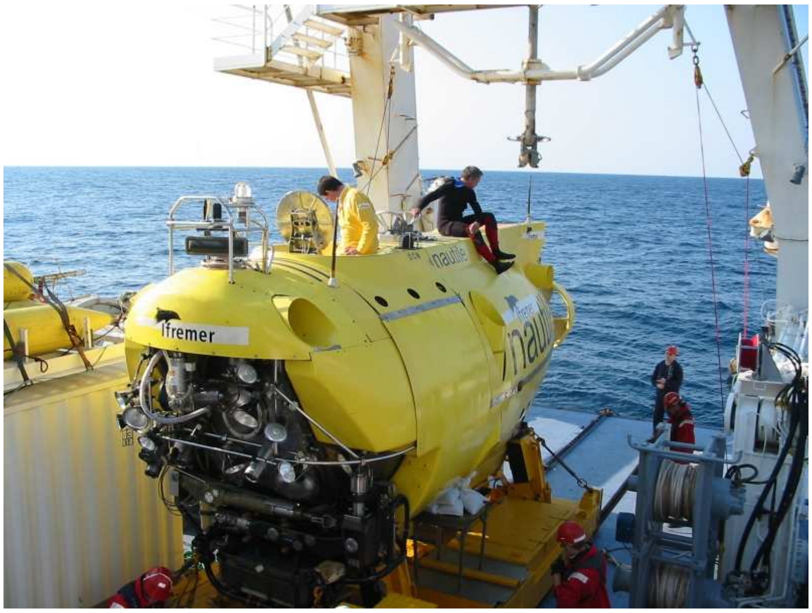

Figure 2.6: View of the Nautile submarine on board the CASTOR ship.

2.4 Environmental parameters

The correct operation of an under-water neutrino telescope depends on several parameters that require a good knowledge and control. Among them, we can mention the water transparency, the optical background, the underwater currents and the sedimentation and biofouling. All of them were studied during the R&D phase with the help of several autonomous lines specially designed for each type of measurement. The latest environmental data was taken with the PSL.

- **Optical background**

  Measurement of the optical background were possible with the PSL. This optical background has deep implications in the *trigger* design, the electronics and the detector mechanics. The main contribution to the background is due to the β-decay of the ^{40}K isotope:

$$^{40}\mathrm{K} \longrightarrow ^{40}\mathrm{Ca} + \mathrm{e}^- + \overline{\nu}_\mathrm{e} \tag{2.1}$$

  The electron carries a maximum energy of 1.3 MeV, enough to produce emission of Cherenkov photons in water. This background is responsible for the baseline in the counting rate as a function of time. The baseline is around 60 kHz (see figure 2.8). Short burst of light (up to few seconds) that can reach several MHz and that are assumed to be produced by bioluminescence are also present. A correlation of these bursts with the speed of the water current is observed. They are classified as isolated *bursts*, if they are only seen by a single OM in a given

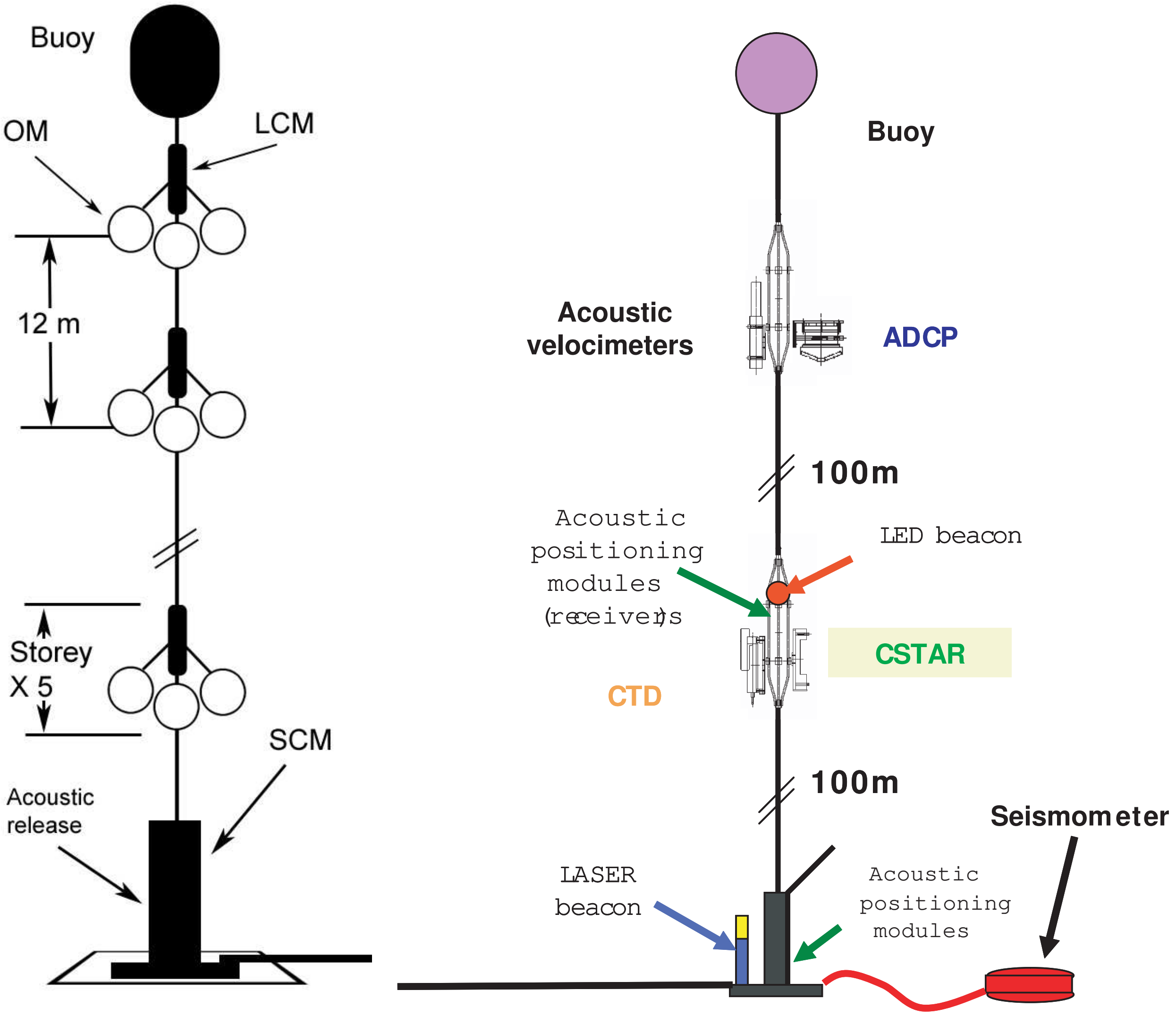

Figure 2.7: Schematic view of the Prototype Sector Line (left) and the Mini Instrumentation Line (right). Their main components are indicated.

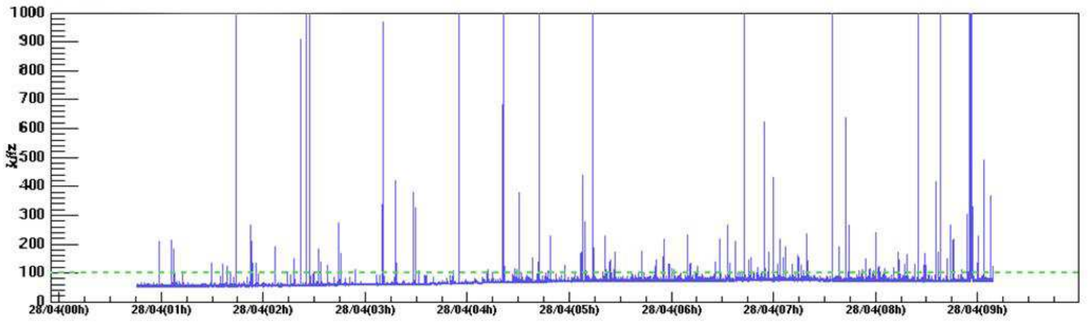

Figure 2.8: The count rate for one OM of one LCM as function of time.

storey, and duet or triplet *bursts*, if they are seen by two or three OMs in the storey respectively. Finally, the baseline changes slowly with time during longer periods. This modulation is thought to be due to another type of bioluminescence, possibly due to bacteria.

Two magnitudes are defined in order to summarize the data taken from the PSL. The *baseline rate* is defined as the median of the recorded count rate in a 15 minute interval, and the *burst fraction* is the fraction of time the count rate exceeds the baseline rate by more than 20%. Figure 2.9 shows the baseline rate (upper plot) and burst fraction (lower plot) recorded by one OMs on one of the storeys (LCM1) as a function of time, from the data acquisition of the PSL. This count monitor shows large variation in the optical background rates. A correlation between bioluminescence and current velocity has also been measured (see figure 2.10).

- **Biofouling and sedimentation**

  Biofouling is a natural process that takes place under sea water. The bacteria stick to the Optical Module surface. Although these bacteria are transparent, they make sediments easier to glue to the Optical Module. The result of some of the measurements performed can be seen in figure 2.11 for different angles of the PIN diodes located in different latitudes of the OM. For an angle $\theta > 90°$ the transmission loss is lower than 1.5% in one year, and it saturates [46]. Sometimes, there is a complete recovery of the total transparency. This phenomenon is correlated with the underwater currents and it could be explained as an increase of clean currents that allows the OM to recover part of the lost transparency.

- **Optical properties of water**

  The optical properties of the water are of main importance since they may affect directly the performances of the neutrino telescope. The OMs density is determined by the light absorption in water. Another important parameter is the light scattering that will constrain the angular resolution of the detector. The

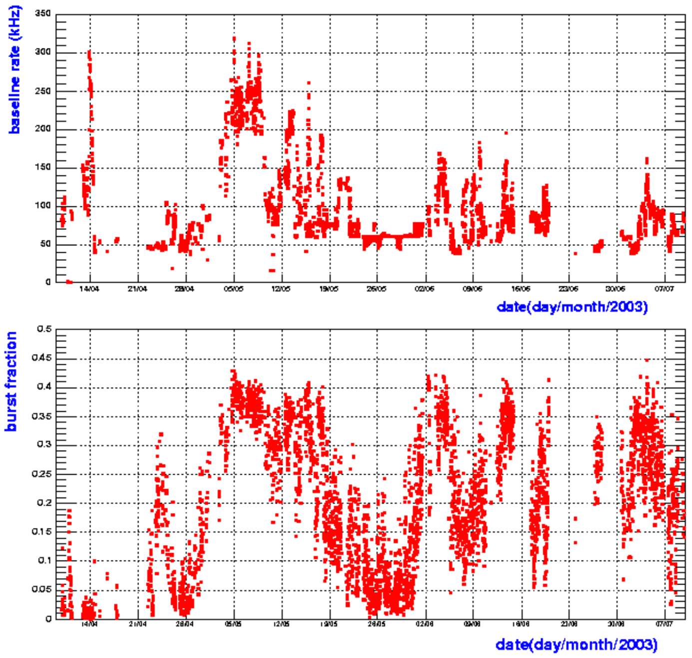

Figure 2.9: The baseline rate (upper plot) and burst fraction (lower plot) for one OM as a function of time for a period of around 13 weeks.

attenuation length was measured by a rigid structure holding a collimated and continuous LED source located at a variable distance from an Optical Module. In order to obtain a constant current on the PMT the LED luminosity is fine adjusted. The value measured for the attenuation length is $\lambda_{att} = 41 \pm 1_{syst} \pm 1_{stat}$ m (see figure 2.12) The attenuation length is a direct consequence of the light absorption and the light scattering and separated measurements have been done for these contributions as well:

$$\frac{1}{\lambda_{att}} = \frac{1}{\lambda_{abs}} + \frac{1}{\lambda_{scatt}} \tag{2.2}$$

To measure the photon scattering an isotropic pulsed source has been used. The fit to the time distribution of the arrival pulses from different distances (24 m and 44 m) detected by a fast PMT, is used to calculate the absorption length and the effective scattering length:

$$\lambda_{scat}^{eff} = \frac{\lambda_{scat}}{(1 - \langle \cos(\theta) \rangle)} \tag{2.3}$$

where λ_{scat} is the scattering length and $\langle \cos(\theta) \rangle$ is the average of the cosine of the scattering angle. Table 2.1 represents the values measured for water transparency.

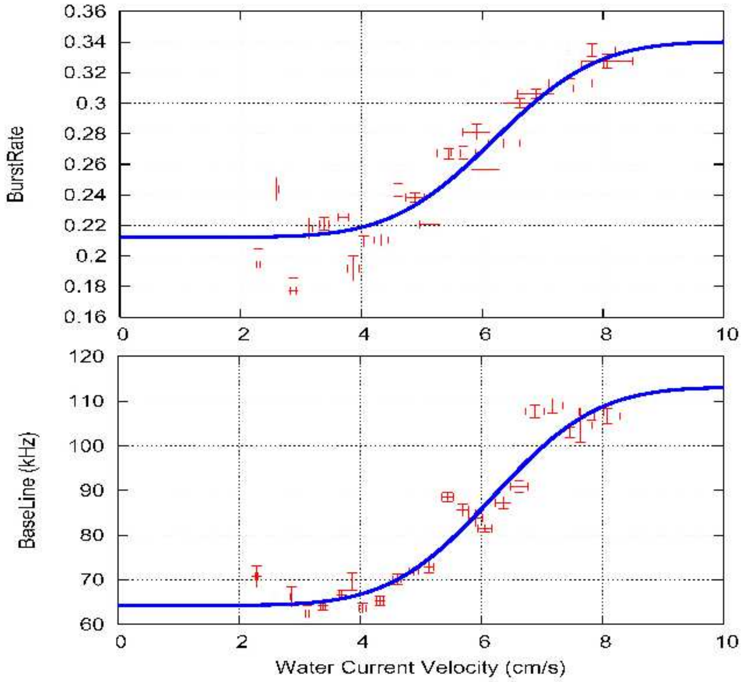

Figure 2.10: Baseline rate (upper plot) and burst fraction (lower plot) as function of the underwater current velocity.

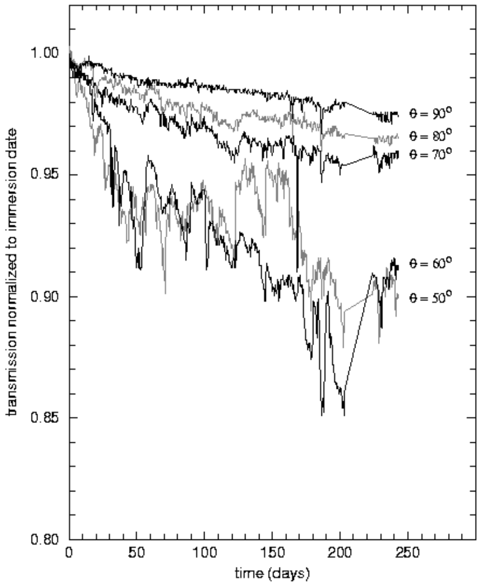

Figure 2.11: Decreasing transparency of an Optical Module as a function of time, at different angles close to the horizontal, over 8 months.

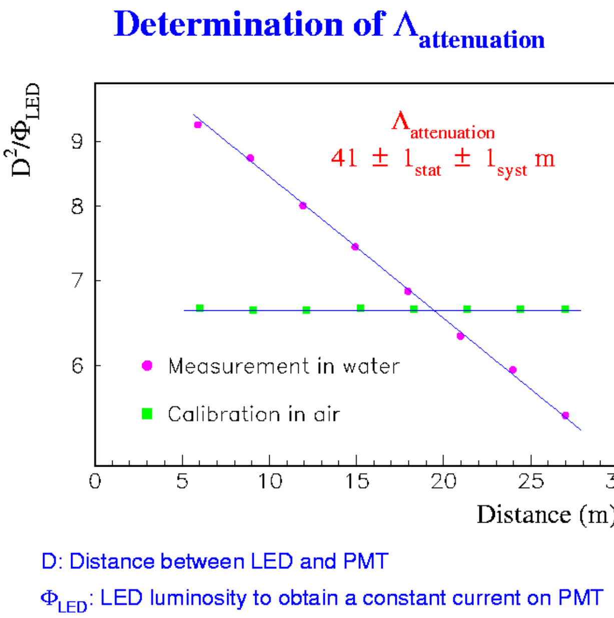

Figure 2.12: Results from the measurement of the attenuation length.

Colour	Period	$\lambda_{abs}(m)$	$\lambda_{scat}^{eff}(m)$
Blue (466 nm)	June 2000	$49.3 \pm 0.3 \pm 2$	$301 \pm 3 \pm 27$
U.V (370 nm)	June 2000	$28.9 \pm 0.1 \pm 1$	$133 \pm 3 \pm 12$

Table 2.1: Measured optical properties of the water.

2.5 Other neutrino telescopes

There are several neutrino telescopes based on the same outlines than ANTARES to detect high energy neutrinos. Some of them are also located under water, but other use the optical properties of the ice.

- **AMANDA**

  The AMANDA project [47, 48] is the first stage of the construction of a 1 km^3 in the South Pole. The telescope started in 1992 and uses ice as the target and Cherenkov medium. Deep ice presents longer absorption length than deep ocean water. Nevertheless, the scattering length in ice is shorter than in water, and affects negatively the achievable angular resolution. Nowadays, the detector is in its AMANDA-II stage (19 strings, 677 OMs) cf. figure 2.13. Although they have no evidence for a extraterrestrial neutrino source, AMANDA has succeeded in the reconstruction of up-going muons coming from neutrinos and in the determination of their energy. This has established in a sound experimental way the principle of operation of the optical neutrino telescopes. The energy spectrum of the measured diffuse flux from the up-going muons detected is compatible with that of the atmospheric neutrino flux. Therefore, a limit on a diffuse flux of extra-terrestrial muonic neutrinos in the energy range 100–300 TeV assuming an E^{-2} spectrum has been set to [49]:

  $$E_\nu^2 \Phi_{\nu_\mu}(E_\nu) < 2.6 \times 10^{-7} \ \text{GeV cm}^{-2}\ \text{s}^{-1}\ \text{sr}^{-1} \tag{2.4}$$

  AMANDA has also demonstrated the possibility to use cascades to detect neutrinos. Charged current interactions of electronic neutrinos produce electromagnetic showers and neutral current interactions of any neutrino flavour produce hadronic cascades. These cascades can be detected with a 4π coverage and thus AMANDA is sensitive to all three neutrino flavours. From the absence of a clear excess of these cascades, the AMANDA-II experiment has set a limit to a neutrino diffuse flux of all three flavours in the energy range between 50 TeV and 5 PeV (and assuming that a hypothetical signal would follow an E^{-2} energy spectrum) of [50]:

  $$E_\nu^2 \Phi_{all\ \nu}(E_\nu) < 8.6 \times 10^{-7} \ \text{GeV cm}^{-2}\ \text{s}^{-1}\ \text{sr}^{-1} \tag{2.5}$$

  This limit assumes that at the Earth the neutrino flavour proportions are ν_e:ν_{mu}:ν_τ = 1:1:1, according to current expectations due to neutrino flavour mixing. Moreover, preliminary limits exist [49] for an ultra-high (1 PeV–3 EeV) neutrino signal looking for events close to the horizon.

  The previous stage AMANDA-B (4 strings, 80 OMs) has measured 188 atmospheric neutrino candidates. Recent results of AMANDA-II, count 1555 events with no evidence of an astrophysical neutrino source (see figure 2.15).

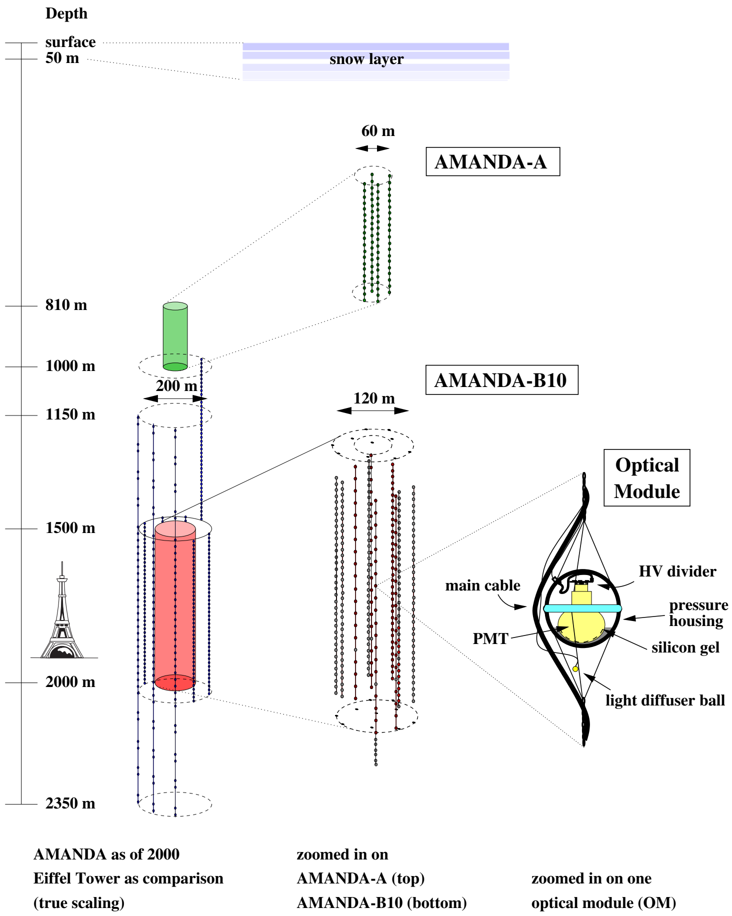

Figure 2.13: Schematic view of the different stages of the AMANDA detector: AMANDA-A (4 lines, 60 m diameter), AMANDA B-10 (10 lines, 120 m diameter) and AMANDA-II (10+9 lines, 200 m diameter).

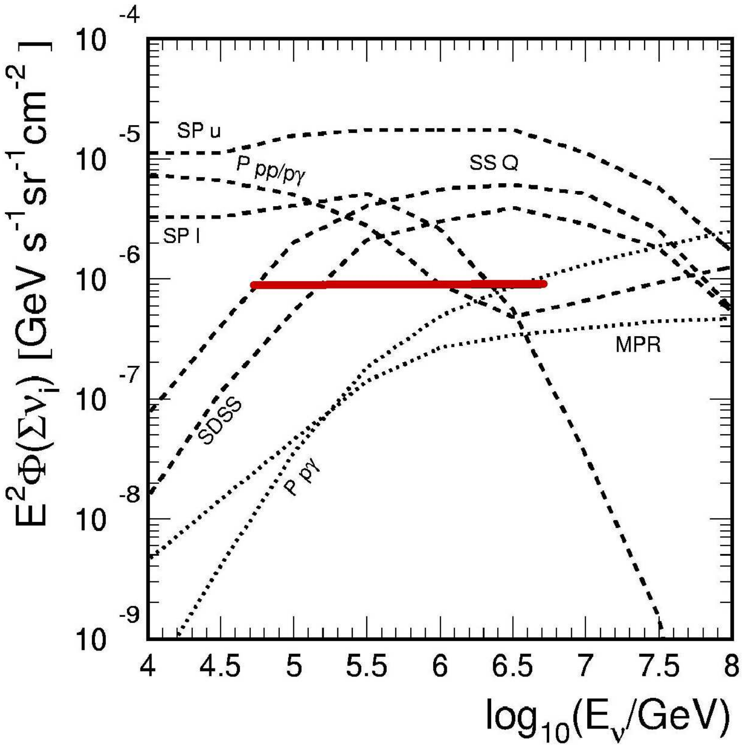

Figure 2.14: Limit on a diffuse extraterrestrial neutrino flux by AMANDA-II [49].

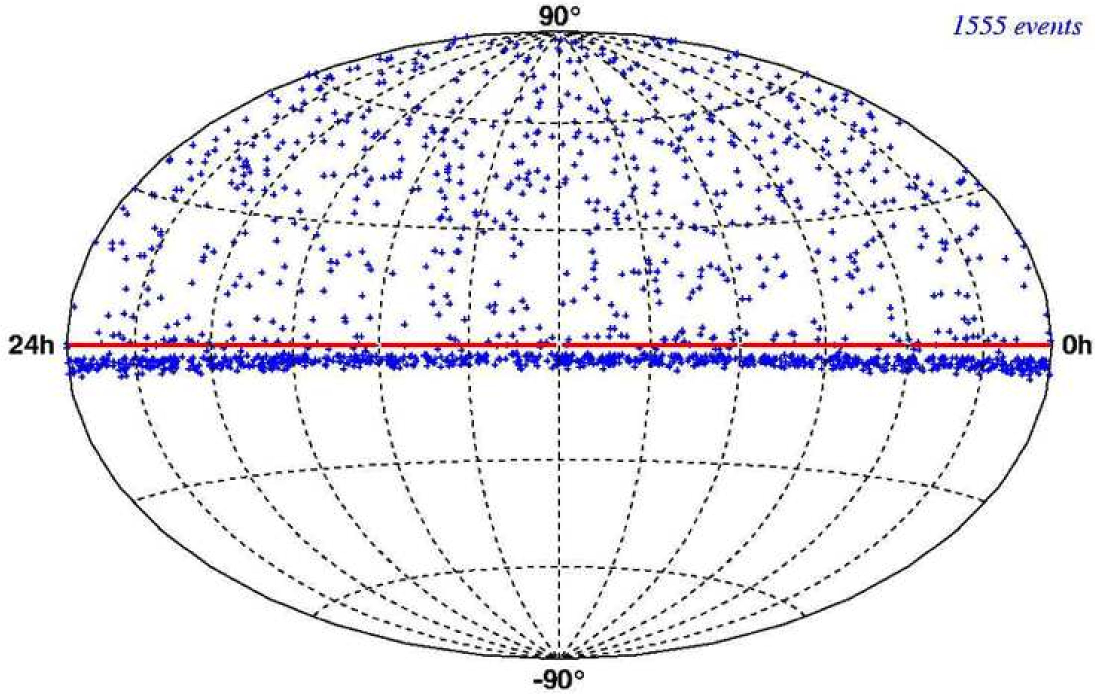

Figure 2.15: Skymap that shows the data collected during 2000 by AMANDA-II. No evidence to suggest an astrophysical neutrino source has been found.

- **IceCube**

  The IceCube project [51, 52] is the one-cubic-kilometre detector successor of AMANDA telescope. It will be located in the same place as AMANDA in the South Pole. IceCube will be considerably more sensitive than AMANDA. It will consist of 80 strings with 60 OMs per string. The project will also include a detector on the ice surface –IceTop– composed of 160 tanks of frozen water with 2 OMs each that will be able to detect cosmic ray showers and muons. This will enable correlation with IceCube and therefore an absolute positioning of the detector. IceCube sensitivity after one year of data-taking to a diffuse flux of muon neutrinos will reach $8.1 \times 10^{-9} E^{-2}$ GeV cm^{-2} s^{-1} sr^{-1} and will have a similar sensitivity, but with full 4π coverage, to cascade events (all neutrino flavours). The sensitivity for point-like sources after one year of data taking will be $5.5 \times 10^{-9} E^{-2}$ GeV cm^{-2} s^{-1} sr^{-1} and will reach an angular resolution around 0.6–0.8 degrees at high energies. The schedule is extremely aggressive with 50 IceCube strings and 100 IceTop tanks deployed by January 2008 and the full detector deployed by 2010. However, the drawback of the location is that both AMANDA and IceCube are not able to observe the Galactic Center.

- **Baikal**

  The Baikal project [53, 54] is the first demonstration of the feasibility for underwater neutrino telescope. Together with AMANDA, they are the only neutrino telescopes that are nowadays taking data. It started in 1981 in the Siberian lake of Baikal at a depth of 1300 m and it is successfully running since 10 years. The experiment takes advantages of the frozen surface of the lake in Winter to deploy the lines. The detector has 8 strings holding 200 PMTs (see figure 2.16) what is called the NT-200 stage. During 2004 and 2005 it will be updated to NT-200+ configuration with 36 more PMTs located in three additional separated strings. Also they are preparing the start of the R&D studies for the Gigaton that will a km^3 detector. During 1998 and 1999, 84 neutrino candidates were detected which is compatible with the expected atmospheric neutrino rate. Recent results set the diffuse limit for astrophysical sources above the AMANDA results [55]:

  $$E_\nu^2 \Phi_{all\ \nu}(E_\nu) < 1.0 \times 10^{-6} \ \text{GeV cm}^{-2}\ \text{s}^{-1}\ \text{sr}^{-1} \qquad (2.6)$$

- **NESTOR**

  NESTOR [56, 57] project aims to deploy a set of towers with 168 OMs in the Ionian Sea (Greece). The site is located at Pylos. These towers will be formed of 12 hexagonal floors. The PMTs will be looking down-wards. The project nowadays is in its R&D phase. Test measurements have already been performed.

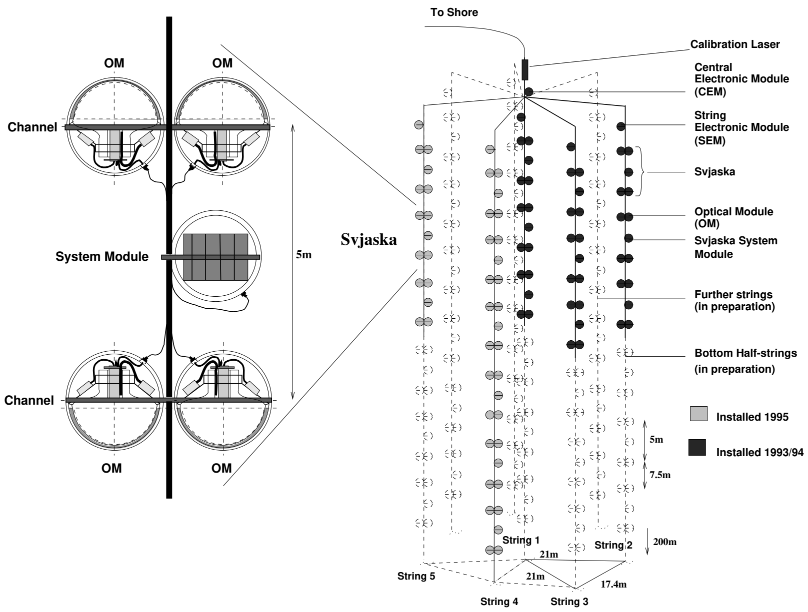

Figure 2.16: Schematic view of the Baikal neutrino telescope.

- **NEMO**

  The NEMO project [58] is a neutrino telescope collaboration starting in 1999. It proposes the construction of a large neutrino detector in the Mediterranean sea in a place called Capo Passero, near the Italian coast of Sicily (see figure 2.17). The site has been deeply studied and now they are completing the R&D activities.

- **ANTARES+NEMO+NESTOR**

  All these three Mediterranean experiments will join efforts in order to construct the first one-cubic-kilometre neutrino telescope in the Mediterranean sea.

2.6 The ANTARES Monte Carlo

ANTARES is expected to be fully constructed during the following years (2004-2007). Until real data could be processed, the Monte Carlo is the best tool in order to compare the performances of the detector. Furthermore, is the only way to study the performances of the detector depending on different arrangements and designs. For that reason, a complete and deep development in the simulation software has been done in the ANTARES collaboration, supporting all the simulation stages needed. The chain of programs which allow us to study the detector response with respect to a neutrino or muon signal can be itemize in four steps:

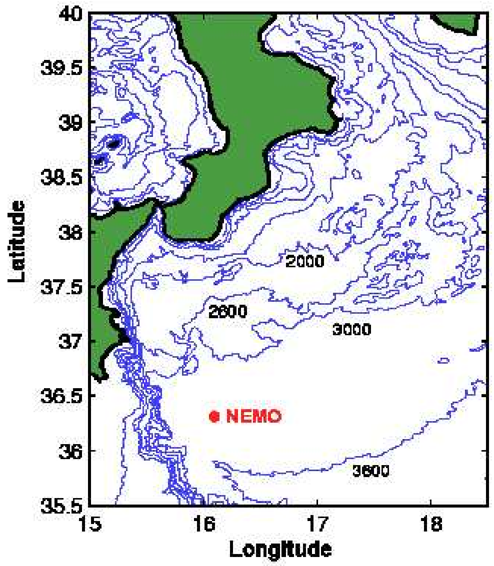

Figure 2.17: Site for the NEMO neutrino telescope.

- Physics generator.
- Cherenkov light emission simulation.
- Response of the photomultiplier and digitization.
- Track and energy reconstruction software.

All these processes can be outlined in the figure 2.18.

2.6.1 The Physics generators

To simulate the neutrino interaction, the ANTARES collaboration has developed a software package named GENHEN [59–61]. This package supports the three neutrino flavours and both interaction channels (neutral current NC, and charged current CC). First, neutrino energy and zenith angle are chosen following a certain input distribution. Then the interaction vertex and target nucleon are chosen. The interaction points are created in a large cylindrical volume or *can* that includes the instrumentation volume inside (see figure 2.19).

This *can* is determined by the light attenuation length in sea water (typically 3 times the attenuation length from the instrumentation volume), and only inside this *can* the light Cherenkov emission will be simulated. Once the vertex is chosen the neutrino interaction is simulated with LEPTO [62]. The CTEQ6 [36] structure functions are used to this aim. For resonant and Quasi-Elastic events RSQ [63] is used at energies

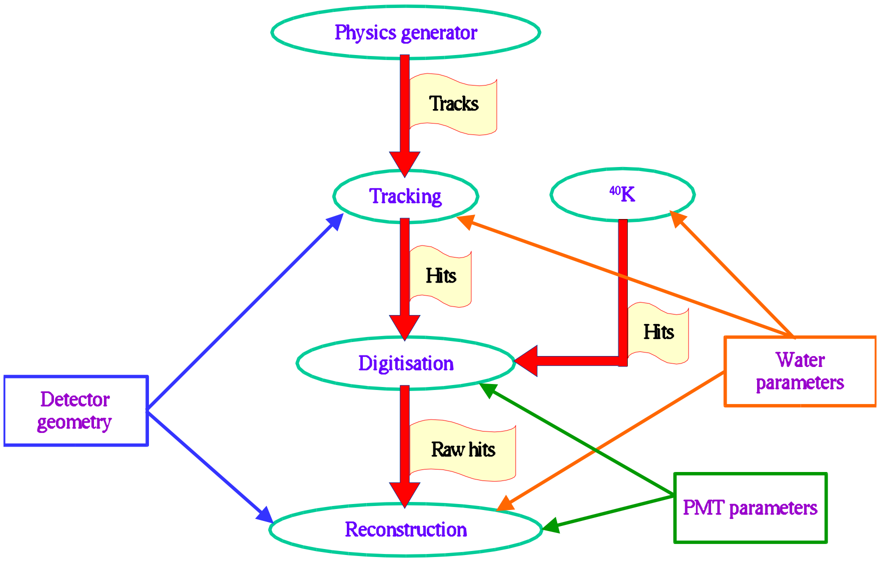

Figure 2.18: Schematic of the ANTARES production chain.

below 100 GeV when this kind of processes plays a major role. If the neutrino vertex interaction is inside the *can*, all final particles from the interaction are stored for further Cherenkov light emission simulation. If the neutrino interaction point is outside the cylindrical volume, only the muon is propagated to the *can* surface.

The background of atmospheric muons is generated with the programs HEMAS [64] and CORSIKA [65,66]. These muons are the remains of the hadronic showers produced by the interactions of cosmic rays at the uppermost layers of the atmosphere (10-20 km). A full simulation of the atmospheric shower is performed, followed by the propagation of the remaining muon to the detector *can*. Once there, these muons are stored as if they were the induced muons of a neutrino interaction outside the *can*. All the simulation is done with a $E^{-\gamma}$ spectrum for the primary flux cosmic rays. Afterward, this could be reweighed following a certain primary flux model.

High energy muons can be detected even if they are produced kilometres away from the detector. However, only the Cherenkov photons emitted in the *can* volume can produce a signal.

There is no reason for a fully track simulation from the vertex where the muon has been produced up to the detector. Nevertheless, the muon track is propagated from this interaction point up to the *can*. Once they reach the *can* surface, a energy cut is applied in order to ensure that the muon will produced a measurable signal. Muons of energy lower than 20 GeV have a range shorter than the distance between the *can* surface and the instrumentation volume, hence they are rejected. The muon propagation is performed by MUSIC [67], PropMu [68] and MUM [69] and is the same for both scenarios: muon from atmospheric showers and from neutrino interactions.

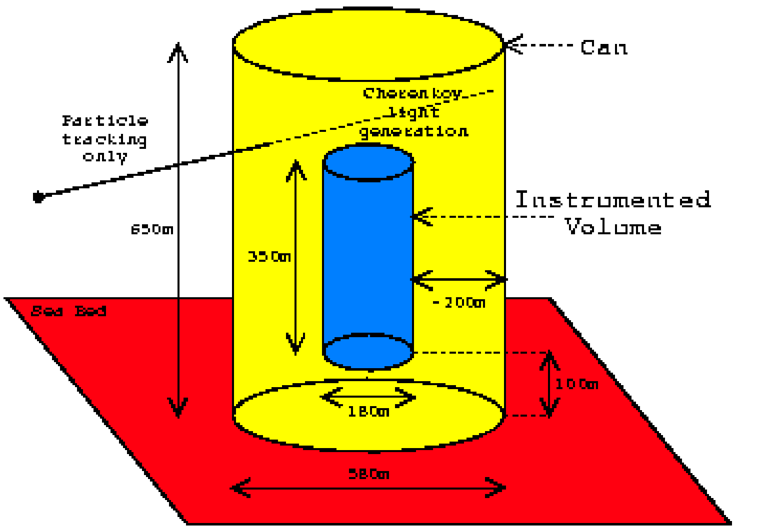

Figure 2.19: Schematic view of the *can* volume used by the generation programs, surrounding the instrumentation volume.

2.6.2 Track simulation and Cherenkov light emission

All the particles that has been stored at the *can* surface level are the input for the track simulations packages. At this stage the available choices are the KM3 [70] and GEASIM [71] programs. The KM3 package was originally devised as a generic track simulation for water and ice. However, what it is used in ANTARES is a specific version specially adapted to the ANTARES singularities. Both packages simulate the passage of the muon through the *can* and all the relevant physical processes: energy loss, multiple scattering, radiative processes, Cherenkov emission, electromagnetic and hadronic cascade production. In figure 2.20 there is an scheme of the data flow into and out KM3.

However, there are some differences between both packages [72]. GEASIM does not include the scattering of light in water but it can simulate hadronic showers. On the other hand, KM3 does include the scattering but does not simulate the hadronic cascade which can add up to a 30% of light in a low energy event. Hence, both packages are used together in order to perform a complete and fully track simulation.

Before simulating physical events, a set of *scattering tables* has to be created. The composition and density of water are fitted to the values of the experimental site.

At each step of the track simulation the Cherenkov cone produced by charged particles is calculated. The *hit* probability for all Optical Modules which are in the cone is calculated and converted into a photoelectron number using Poisson statistics.

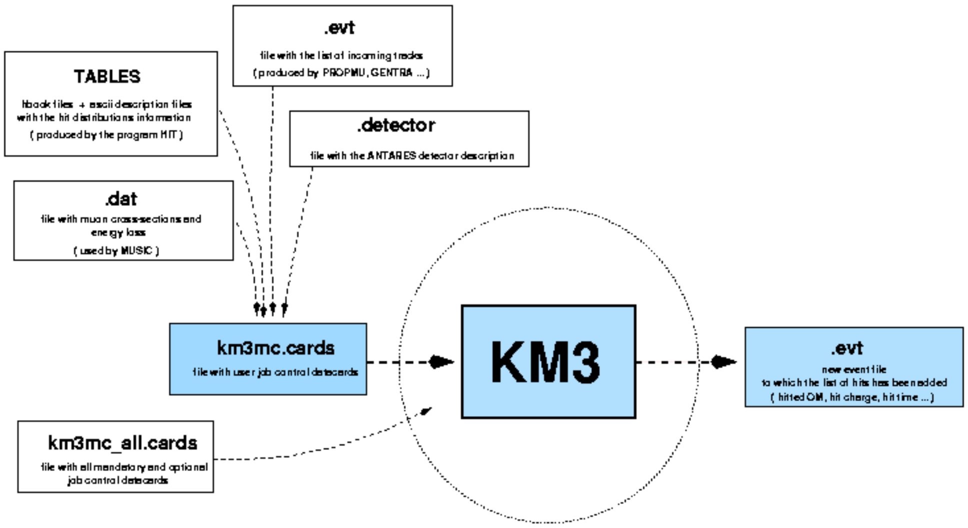

Figure 2.20: Schematic data flow of the KM3 program.

Several elements are taking into account to evaluate this hit probability, such as the wavelength dependent absorption length, the quantum efficiency and the transmission coefficients of the glass sphere and the silicone gel. Also the relative orientation of the PMT with respect to the Cherenkov front and its angular acceptance are considered. The number of Cherenkov photons produced by each track segment is computed by means of a Poisson distribution with mean $763 \cdot Q^2 \cdot d \cdot \sin^2(\theta_{ch})$, where Q is the particle charge, d is the length of the current tracking step in metres, and θ_{ch} is the Cherenkov angle. For each number of Cherenkov photons a position, an energy and a direction are computed.

Afterward, given a photon flux of wavelength λ, $\Phi_\gamma(\lambda)$, that arrives to the OM with an angle θ_γ with respect to the PMT axis, the number of produced photoelectrons, N_e is calculated by:

$$\frac{dN_e}{dx} = A_{geom} \epsilon \alpha f(\theta_\gamma) \int \Phi_\gamma(\lambda) T(\lambda) Q(\lambda) e^{-b/\lambda_{abs}} d\lambda \tag{2.7}$$

where A_{geom} is the photocathode area, ϵ is the charge collecting efficiency, α represents the effect of the magnetic shielding, $T(\lambda)$ is the transmitivity of the sphere and the optical gel, $Q(\lambda)$ the quantum efficiency of the PMT and $f(\theta_\gamma)$ is the angular response. Finally b and λ_{abs} are the total travelled length and the absorption length respectively. All these parameters has been adjusted to the actual components of the detector. The Cherenkov photon flux can be computed from the spectrum of Cherenkov emission and the expansion of the corresponding wavefront.

$$\Phi_\gamma(\lambda) \propto \frac{1}{\lambda^2 d} \tag{2.8}$$

Figure 2.21 illustrates how the Cherenkov photons produced by one muon track are propagated through the medium. Information of the photons is stored at the boundaries of spheres (shells) until they are absorbed or leave the instrumentation volume.

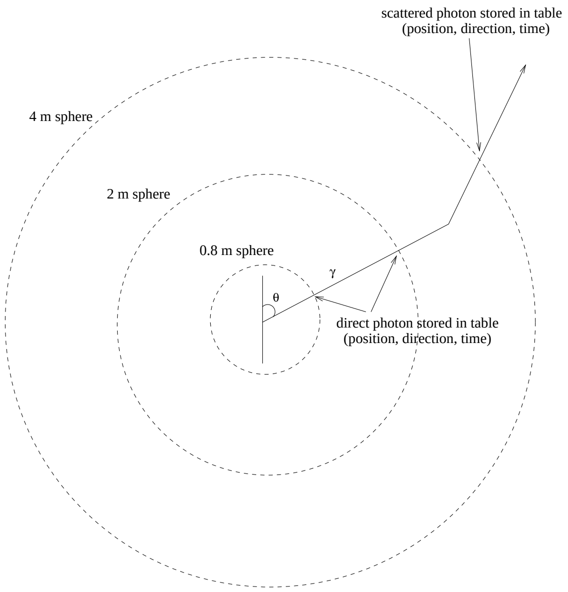

Figure 2.21: Scheme of the spherical shells for creation of scattering tables.

Apart from the signal produced in the PMTs due to the Cherenkov light emission from muons (*hits*), these packages (both GEASIM and KM3) also simulates the *hits* due to the optical background at the ANTARES site. The main optical background is produced by the β decays of ^{40}K and bioluminescence. Bioluminescence is difficult to model and predict, and therefore has not yet added to the Monte Carlo. However, this is not very important since bioluminescence will affect only to given parts of the detector in a recognizable way. Therefore, the appearance of bioluminosity can be easily rejected by the *trigger*. This is not the case of the ^{40}K background. The β particles produced by the natural radioactivity of the ^{40}K will give raise to light at a rate up to 60 kHz in a 10 inches photomultiplier. This will affect the whole detector 100% of the time and even *triggered* events will hold a fraction of these *hits*. The light emitted by β particles arrives randomly to the Optical Modules, uncorrelated with the muon passage. Finally, there is another source of optical background: the dark noise pulses produced in the photomultiplier itself, however this pulse rate is very small ($\sim$ 2 kHz) compared to the rate from ^{40}K ($\sim$ 60 kHz).

2.6.3 Digitization

KM3 and GEASIM alike, also perform the simulation of the detector response and the digitization. After the PMT simulation above described we are left with a number of photoelectrons. In ANTARES detector the *hits* are digitized by an ASIC which is called ARS [73]. The behaviour of the ARS response can be approximated by setting a few parameters like integration, dead time and saturation, allowing a rather realistic and simple simulation. Both packages perform this simulation of the electronics in the Optical Module that limits the maximum amount of light collected in the same Optical Module and the number of *hits* collected in a short period of time. However, a more sophisticated simulation of all the electronics functionality which includes as well the option of a fast signal sampling will be developed for the simulated data offline chain production.

2.6.4 Event Reconstruction

Once data are fully simulated, the next stage on the Monte Carlo chain is to analyze the output data, and to reconstruct the events. RECO is the main program used by the ANTARES collaboration [74–76]. RECO, written in C++, inherits the basic algorithms and classes from POSIDONIA, the first reconstruction program used on ANTARES. One of the capabilities of this reconstruction program is that the user can choose among different track reconstruction strategies, as well as among different energy estimators to reconstruct the energy of the event or for spectra reconstruction. The purpose of asking for a different reconstruction strategy depends on the type of events and physics the user is interested in: down-going atmospheric muon events, very low energy events or multi-string reconstruction. Among the multi-string reconstruction strategies, the user can choose any of the followings:

- The *Standard strategy* is the first reconstruction algorithm written for ANTARES. Many aspects have changed from the POSIDONIA reconstruction fit procedure, though, the basic concepts of the *Standard strategy* remains the same. The reconstruction fit uses the arrival time to the PMT of the light emitted by muons. These photons may be *direct photons*, if they do not suffer any scattering or *indirect photons* if they do. There are also Cherenkov photons emitted by secondary particles produced by the muon interaction with the media. However, these *hits*, firstly mingled with the direct Cherenkov *hits*, have arrivals times that are uncorrelated to the track parameters. Figure 2.22 shows the different kinds of photons that may produce a signal in an Optical Module.

- The *Carmona strategy* also called the *Iterative strategy* was developed in Valencia [77], and it means the first marked improvement with respect to the *Standard strategy*. The first step of this *iterative strategy* is the usage of a new pre-fit method. This new pre-fit is based on the geometrical relationships between the Cherenkov *hits* and the track hold as a consequence of the fixed Cherenkov angle. For any direct *hit* i produced, the relation followed is:

$$r_i = \frac{ct_i - ct_0 - L_i}{\tan\theta_c} \tag{2.9}$$

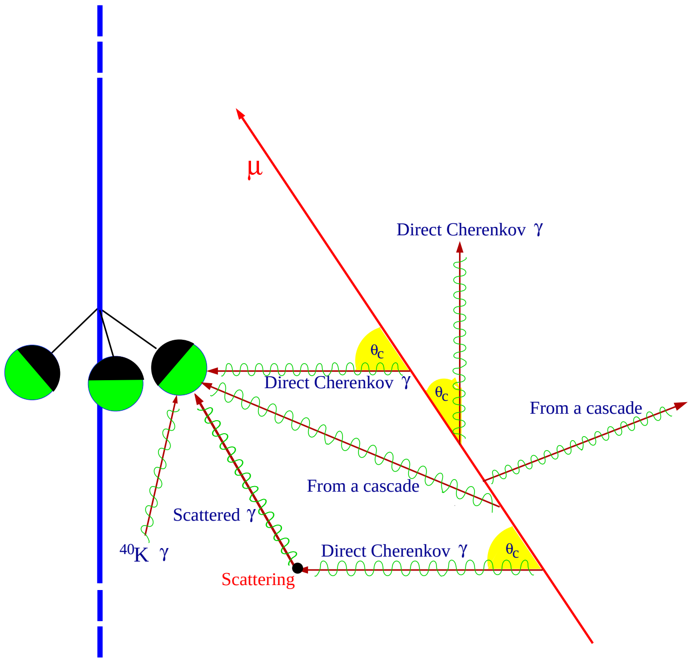

Figure 2.22: Schematic view of the different kinds of photons according to the way they are produced. Direct Cherenkov photons are the first photons from the muon track to arrive to an Optical Module. Other photons produced by the track arrive some time later. Photons from ^{40}K decays and bioluminescence can arrive at any time since they are not correlated with the passage of the muon.

where r_i is the transverse distance from the muon track to the PMT, L_i is the longitudinal distance along the track direction, and t_0, and t_i are the reference time and the photon arrival time respectively (cf. figure 2.23).

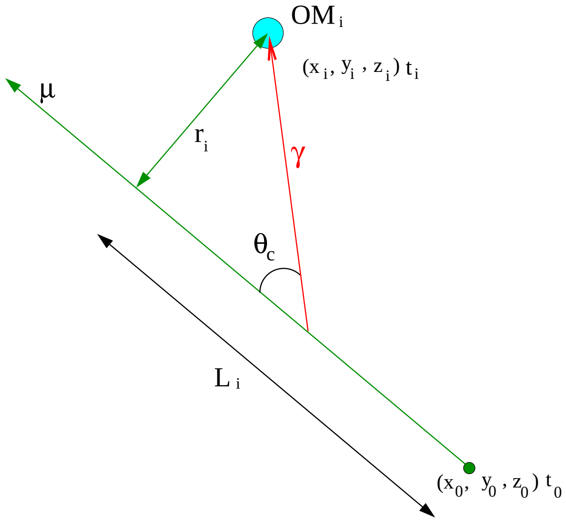

Figure 2.23: Arrival of photons to an Optical Module.

By grouping two or three *hits* it is possible to find the track projection in the plane determined by the three *hits*. Once the track projection is determined and t_0 is obtained by:

$$t_{0,i} = t_i - \frac{1}{c}(L_i + r_i \tan\theta_c) \tag{2.10}$$

the whole track information is fully recovered and reconstructed.

- The *Aart Strategy* [78] also used in this study, was developed after the *Iterative strategy* and also makes an important contribution with respect to the *Standard strategy*. This method can be considered as an improved version of the linear prefit. The reconstruction algorithm consists of a sequence of different fitting procedures. Each of them use the result of the previous one as input. Also a maximum likelihood method has been include that performs the likelihood of *hits* from the background light.

There is also a reconstruction strategy based on a *single-line* reconstruction performance. This strategy uses the *hits* of one string only, it is therefore suitable for only vertical or low energy muons near the string. The procedure begins applying (after a software *trigger*) the *hit* selection based on causality and select the string that contains the most of the *hits* selected. Then performs a one dimensional track prefit and the track fit with the selected *hits*.

2.6.5 Analysis tools

The analysis tool chosen for this study has been the ROOT framework [79]. For this issue a set of new libraries has been developed for the specific ANTARES experiment. The output of the Monte Carlo production chain described above is stored as ASCII files. A program written in C++ enables to transform those ASCII files into the proper ROOT format that will be used in the analysis. A set of macros has been also developed in order to compute several performances of the ANTARES telescope that will be used at the comparison level in this study.

2.6.6 Detector generator

Another package used by the ANTARES collaboration is the program GENDET [80, 81]. This program permits to generate detector geometries by the use of input cards. It allows to produce aligned and misaligned detectors in a fast and flexible way. The detector description is stored at present in ASCII files and it is used as an input in the Monte Carlo chain production.

2.7 ANTARES performances

In order to compare the performances of several detector geometries we should set the magnitudes and parameters that better describe the telescope efficiency. The predicted number of detected events from several neutrino fluxes will give an idea of the difference among the detector geometries. Nevertheless, other parameters have also to be taken into account.

2.7.1 Effective Area

The *effective area* of the ANTARES detector is the way used to express the detector efficiency. The ratio of selected events with respect to the incident flux could be already a reasonable quantity of the ANTARES efficiency. However, expressing this efficiency in terms of an effective area is a more convenient way. This parameter reflects the size of a 100% efficient surface that observes the same number of through-going neutrinos/muons than the detector. This effective area can be used then, to calculate event rates incorporating all the information contained within the simulation and reconstruction.

Neutrino effective area

The effective area can be expressed both in terms of muons and neutrinos. The neutrino effective area is computed from the number of events selected with respect to the total incident neutrino flux arriving at the Earth. The neutrino effective area is a function of the neutrino energy (E_ν), and the neutrino direction (θ_ν, ϕ_ν). The expression that leads to the neutrino effective area is the following:

$$A^{\nu}_{eff}(E_\nu,\theta_\nu,\phi_\nu) = \frac{N_{selected}(E_\nu,\theta_\nu,\phi_\nu)}{N_{generated}(E_\nu,\theta_\nu,\phi_\nu)} \times V_{generation} \times (\rho N_A) \times \sigma(E_\nu) \times P_{Earth}(E_\nu,\theta_\nu) \quad (2.11)$$

where $N_{generated}$ is the number of events in the generated neutrino flux and $N_{selected}$ is the number of selected events after the reconstruction selection criteria for each strategy. $V_{generation}$ is simply the *can* volume. The term ρN_A accounts for the target nucleon density of Earth. The neutrino cross-section per nucleon is represented by $\sigma(E_\nu)$ and finally the factor P_{Earth} takes into account the Earth absorption for a given neutrino, and it is a function of the energy and direction of the neutrino. If an isotropic, upward neutrino flux is supposed, then the effective area can be averaged and will remain only as a function of the neutrino energy.

Once the effective area is computed, it will allow us to calculate the number of selected events for any incident flux by using the expression 2.12. No reference or additional assumptions concerning the neutrino cross-section will be required.

$$N_{selected} = \int A_{eff}(E_\nu, \theta_\nu, \phi_\nu) \times \frac{d\Phi_\nu}{dE_\nu d\theta_\nu d\phi_\nu} dE_\nu \, d\theta_\nu \, d\phi_\nu \quad (2.12)$$

where $\frac{d\Phi_\nu}{dE_\nu d\theta_\nu d\phi_\nu}$ is the differential neutrino flux before entering the Earth.

Muon effective area

Historically, the ANTARES efficiency was presented in terms of an effective area as a function of the muon energy at the detector. However, this method did not consider a unified footing of medium and low energy events. A new definition was proposed in [82] as function of the neutrino energy that combines both surface and volume event. Taking into account the relation between the neutrino flux and the muon flux we can write the number of reconstructed events in terms of the latter as:

$$N_{observed} = \int \frac{V_{eff}(E_\nu)}{\langle R^{\mu}_{eff}(E_\nu)\rangle} \frac{d\Phi_\mu}{dE_\nu} dE_\nu \quad (2.13)$$

where once again V_{eff} is just the can volume, $\frac{d\Phi_\mu}{dE_\nu}$ is the muon flux in terms of the neutrino energy and $\langle R^{\mu}_{eff}(E_\nu)\rangle$ is the average effective muon range defined as:

$$\langle R^{\mu}_{eff}(E_\nu)\rangle = \int \frac{dP_\mu}{dE_\mu} R_{eff}(E_\mu) dE_\mu \quad (2.14)$$

where $\frac{dP_\mu}{dE_\mu}$ calls for the probability of a neutrino to produce a muon in the interval dE_μ and $R^{\mu}_{eff}(E_\nu)$ is the effective range that is the average distance travelled by muons with a given starting energy up to the point where their energy goes below a given threshold.

The first term in the integral in expression 2.13 is a quantity with area dimension, when multiplied by a differential muon flux will give an event rate and therefore it is defined as the muon effective area:

$$A^{\mu}_{eff}(E_\nu, \theta_\nu, \phi_\nu) = \frac{N_{selected}(E_\nu, \theta_\nu, \phi_\nu)}{N_{generated}(E_\nu, \theta_\nu, \phi_\nu)} \times \frac{V_{generation}}{\langle R^{\mu}_{eff}(E_\nu) \rangle} \tag{2.15}$$

The effective area such expressed can be considered as the area of an equivalent *flat* surface at the ANTARES detector. Despite being an effective area for muon it is expressed as a function of the neutrino energy. Another remark is that although the quantity $d\Phi_\mu/dE_\nu$ in expression 2.13 is well defined (as the total flux of muons produced by neutrinos with energies in the range $E_\nu \to E_\nu + dE_\nu$) it is not the obvious way to describe a differential muon flux. Nevertheless, this description is the most suitable in terms of calculations for several reasons. There is not a well defined surface on which all the muons are incident and therefore there is not well defined muon energy since it changes as the muon propagates (One could choose the muon energy at the interaction vertex, or when crossing some arbitrary surface inside the instrumented volume). Using the neutrino energy instead of expressing the muon flux in terms of the muon energy, simplifies also the computations since one could take the advantages of the fact that the initial event distribution is known from the inputs of the event generator.

2.7.2 Angular Resolution

The angular resolution is one of the requirements of a neutrino telescope such as ANTARES. The angular resolution of the event is defined as the angle between the muon track and the reconstructed track. There is also a defined neutrino angular resolution which expresses the angle between the true neutrino and the reconstructed muon track. Both distributions are presented as the median of the distribution in each energy bin. The neutrino angular resolution contains the angle between the neutrino and the outgoing muon in the interaction. Furthermore, for energies lower than 10 TeV the neutrino angular resolution is dominated by this unavoidable physical angle. For that reason the muon angular resolution is more suitable to describe the angular performances of the ANTARES telescope. Therefore, the detector pointing accuracy can be represented by the muon angular resolution, and the pointing accuracy for a neutrino point-like source by the neutrino angular resolution.

2.7.3 Flux limits

Since the expected number of events from astrophysical sources is very low, one of the expected results of the ANTARES detector is an upper limit for the diffuse fluxes. Even if no point-like source is detected it is possible to estimate an upper limit to the flux formed by all point sources emitting together. In figure 2.24 can be seen the ANTARES average upper limit for diffuse fluxes compared with other experiments. Some theoretical models are also shown.

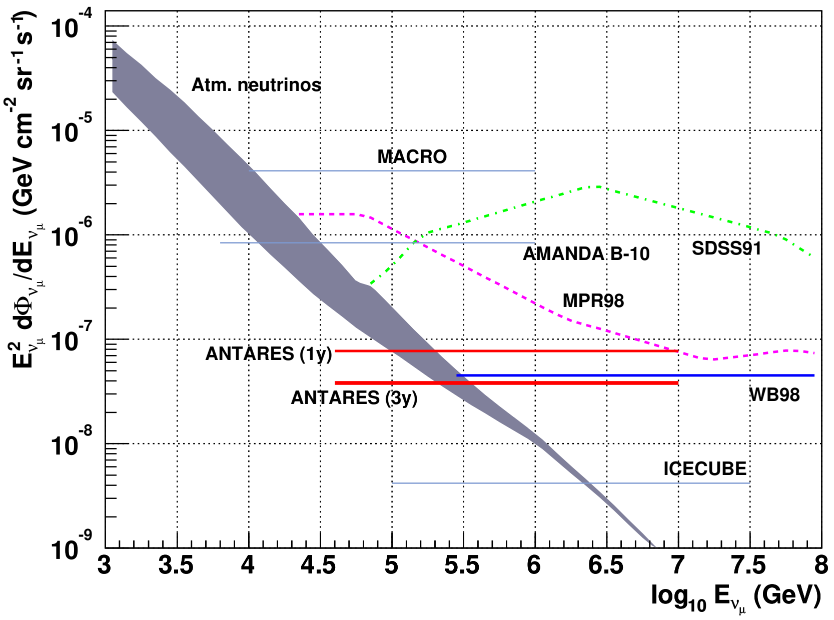

Figure 2.24: Comparison of different diffuse limits for several experiments and the ANTARES (1 year) and ANTARES (3 year) sensibility.

Concerning the search for point-like sources, the dotted line in figure 2.25 shows the flux limit as a function of the source's declination that ANTARES can set after one year of data taking assuming an E^{-2} energy spectrum. As can be seen, it will be the best limit set in the southern sky. Also indicated in this plot are similar flux limits set by the SuperKamiokande, Macro and the AMANDA experiments together with some theoretical expectations for a few source candidates.

More results on the expected performances of ANTARES can be found in [77] and [83].

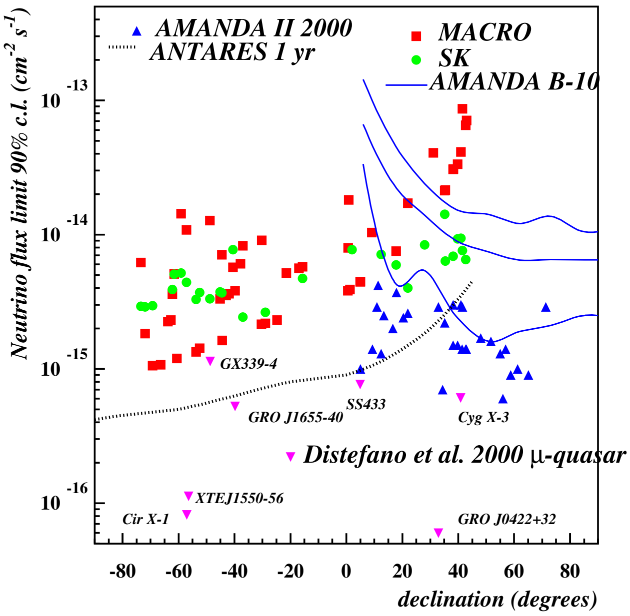

Figure 2.25: All sky flux limit results obtained for several experiments and the estimate of the ANTARES limits after 1 year.

Chapter 3

A new detector layout

In this chapter the results of the study of the performances of a set of 12–string detector layouts with several storey arrangements are presented. The main magnitudes in the characterization of the ANTARES telescope such as the effective area, the detector response to an E^{-2} signal and the angular resolution are studied and compared using the standard 10–string detector as a reference.

3.1 New 12–string detector layout

Up to now, the official detector was a 10–string detector the so-called **d04**. This detector follows an octagonal layout as can be seen in figure 3.1, and has also a certain string arrangement, i.e., each string holds 30 storeys with 3 photomultipliers (see figure 3.2) which amounts to a total of 900 PMTs. The aim of this study is to increase the efficiency of the detector preserving the same number of PMTs by adding two more strings. This goal implies not only a new string arrangement at the seabed but also a new *intra–string* configuration in terms of number of storeys and distance among them. However, the inner storey configuration remains the same, i.e.: each storey holds three OMs pointing at 45 degrees below the horizontal.

The **d04** detector (from now on also called the 10–string detector) has what we call the standard string arrangement, i.e. a string that has 30 storeys separated a distance of 14 metres.

As just mentioned, in order to increase the efficiency, a new 12–string detector with a reduced number of storeys has been proposed. Our strategy will be the following: firstly, we will study what happens if simply two more strings are added without changing the *intra-string* arrangement. The configuration of this detector would have 1080 PMTs and will be named the **d08** detector henceforth. This initial stage allows us to study in more detail the correlation between the effect of the string distance and the *intra–string* design. This new detector layout differs slightly from the octagonal layout of the 10–string detector of figure 3.1 in order to ensure the isotropic response of the detector.

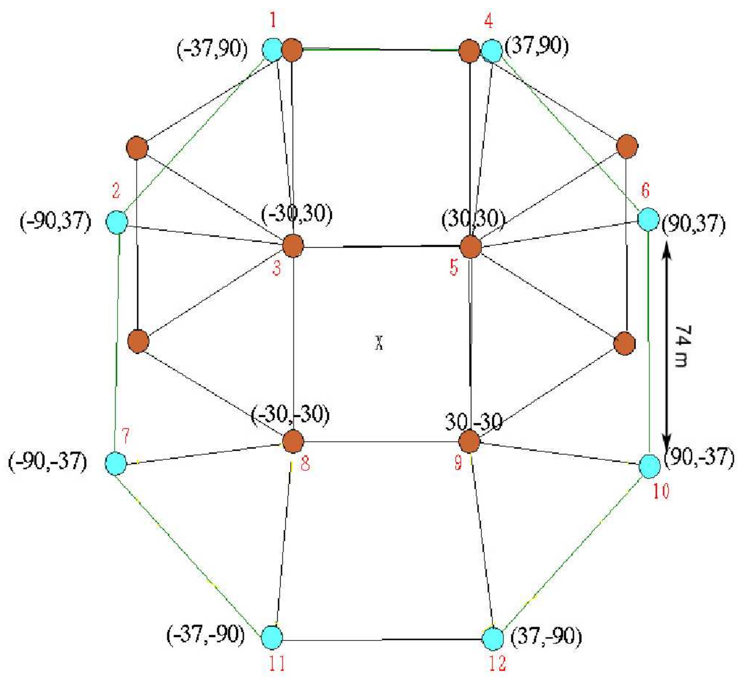

Figure 3.1: The red dots represent the 10–string detector layout **d04**, the blue ones are the new 12–string detector layout **d08**. Coordinates in metres are referred to the X center mark.

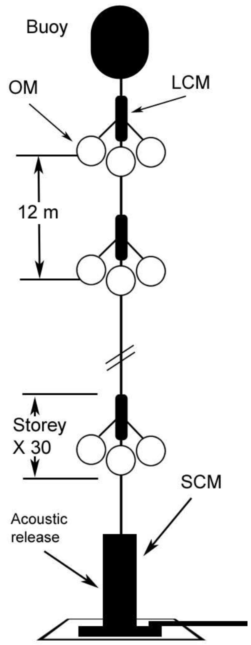

Figure 3.2: Schematic view of the *standard intra–string* design, with 30 storeys 12 metres apart one from each other.

Once we have studied the response of this detector we are ready to propose other detectors constrained to have a total number of 900 PMTs.

Since the new **d08** has 1080 PMTs, better effective area and angular resolutions are expected. These detector configurations are produced by the GENDET program [80, 81]. Once the detector was created, a Monte Carlo production was generated in order to simulate its response.

3.1.1 Effective area for reconstructed muons

As mentioned in previous the chapter, the effective area is one of the main magnitudes to take into account in order to study the performances of a neutrino telescope. In this section we compare the muon effective area of the new 12–string detector with 1080 PMTs (**d08**) and the 10–string detector (**d04**). The comparison of their muon effective areas in the whole energy range can be seen in figure 3.3. To a first approximation, the increase in the muon effective area of **d08** w.r.t. **d04** is as expected. A more detailed view in the high and low energy ranges can be seen in figure 3.4. In the high energy range (lower plot in figure 3.4) the results show that the **d08** detector has the best effective area. If we estimate how much effective area is gained by **d08** with respect to **d04** an increase of $\sim$25% is obtained. Therefore, for **d08** the increase in effective area seems to scale with the number of strings added.

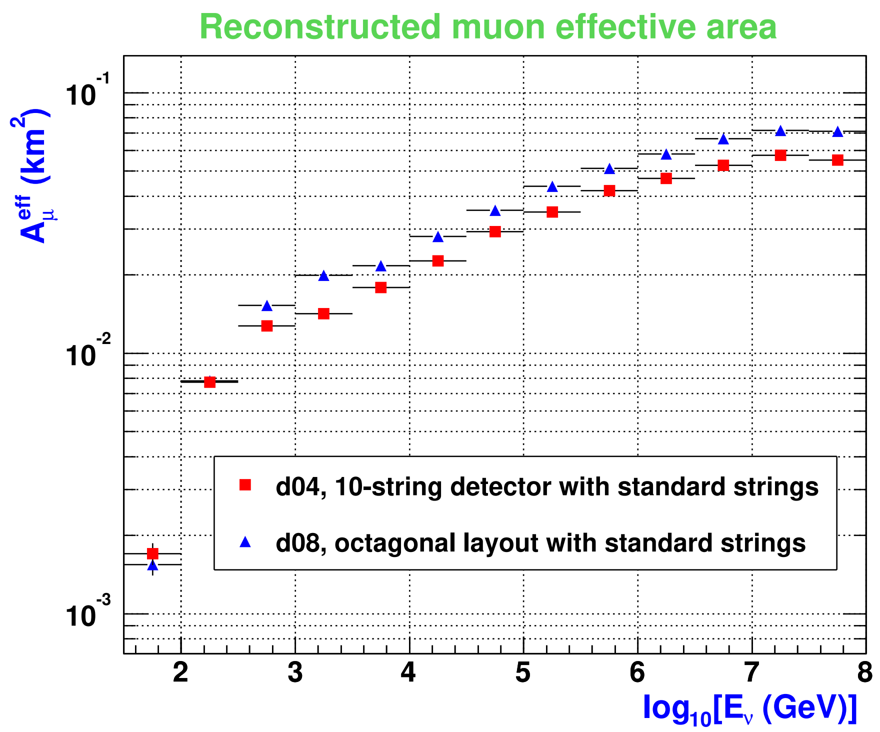

Figure 3.3: Reconstructed muon effective areas as a function of the neutrino energy for the 10–string detector **d04** and the 12–string detector **d08**.

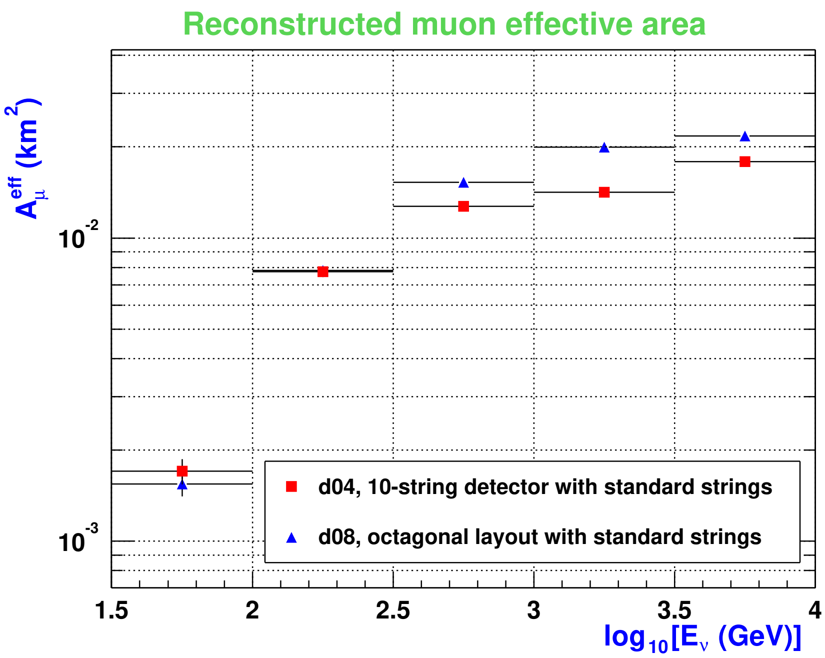

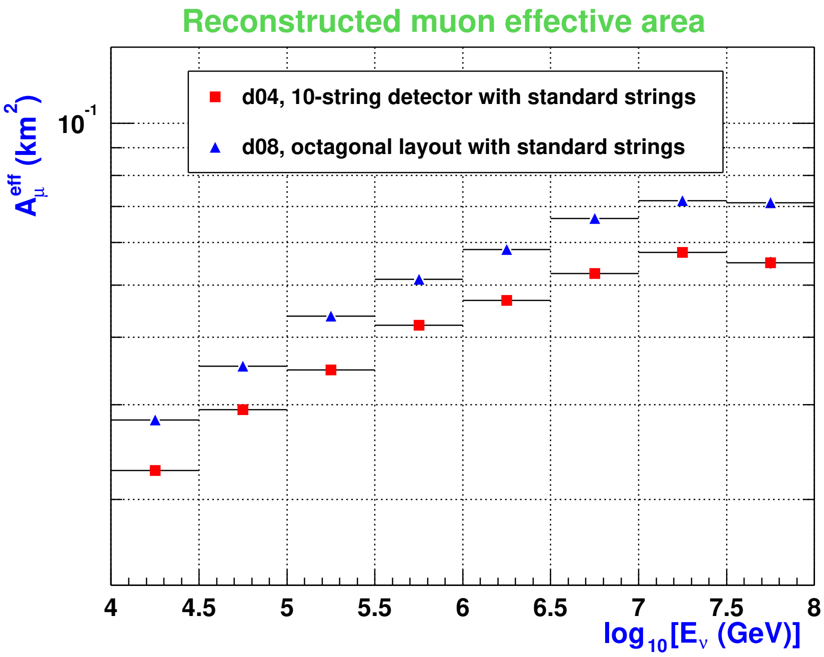

Figure 3.4: Blow-up of the muon effective area as a function of energy for the **d04** and **d08** detectors for the low energy (upper-plot) and the high energy (lower-plot) ranges.

This increase has been computed using the integrated sum over the energy bins, which has the drawback of giving more importance to the higher energy bins. Although there are other ways to calculate the increase in percentage, this is the simplest one and reflects clearly how much the effective area has increased. At lower energies there is an unexpected effect: both detectors seem to have the same response below $10^{2.5}$ GeV (figure 3.4 upper plot). In order to discard that this effect is an artefact caused by the reconstruction software, we tried another reconstruction strategy, the so-called Aart strategy [78] (figure 3.5).

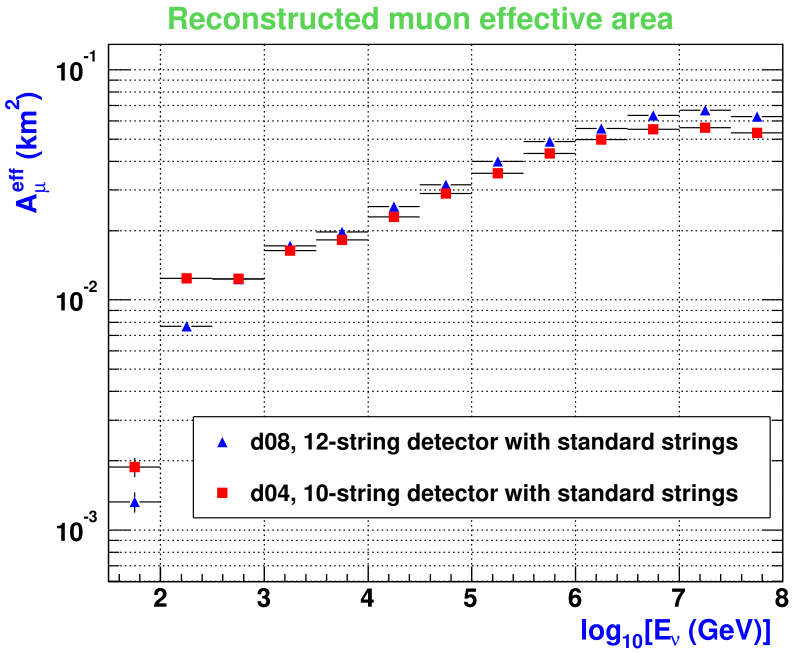

Figure 3.5: Reconstructed muon effective area for the two detector **d08** and **d04** with the Aart strategy.

As can be seen from the figure above, for this latter strategy, there is even a *cross-over* among the first bins in the effective areas. Therefore, this effect is present in both cases, but the details depend on the reconstruction strategy and the selection cuts.

This result hints that this effect is not motivated by a software problem, but is due to the intrinsic characteristics of the detection principle at low energies. A possible explanation is the following. At low energies, at most three strings are used by the reconstruction software. This is because the emission of light from the induced muon is very small and can only reach a few strings. Therefore, the shower only affects one string and the closest ones. The main factor in the efficiency of the detector at low energies may not be the number of strings but their proximity. We can see in figure 3.1 that the strings are closer to each other in the **d04** detector than in **d08**. To have a numerical idea we can estimate the average distance from each string to the two nearest ones: we obtain an average value of 60 metres for the 10–string detector **d04** and 65 metres for the 12–string detector **d08**. One could think that this difference is too small to have a sizeable effect on the detector efficiency, however the distance between strings is of the order of the absorption length of light in water and therefore a small change may have an important influence (see table 2.1).

We can take this idea further and count the number of strings with at least two hits (to ensure that they are not a ^{40}K) and plot it as a function of the energy (figure 3.6).

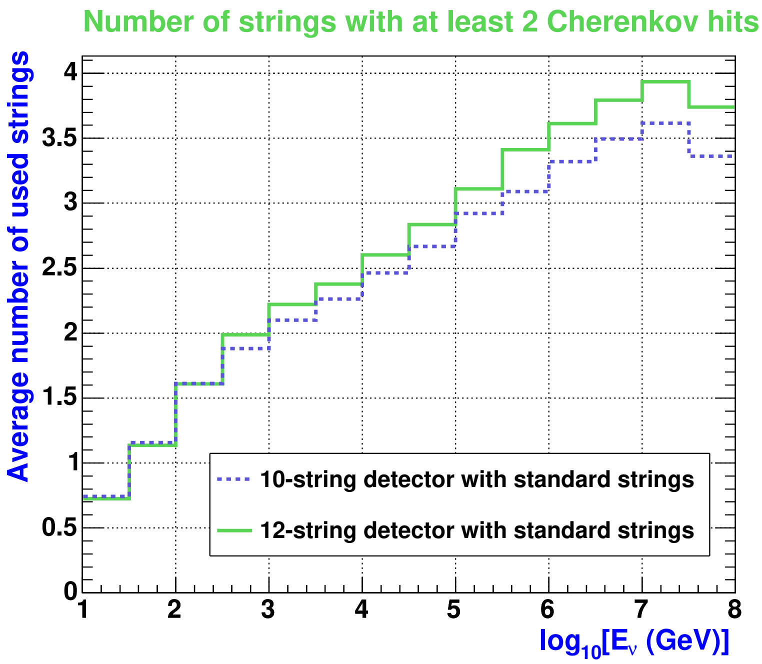

Figure 3.6: Average number of strings with at least two hits as a function of the neutrino energy for the **d04** and **d08** detectors.

The results in figure 3.6 suggest that both detectors have the same performances at low energy because the same number of strings are being *activated* by a *trigger* defined by at least two simultaneous hits.

We can also compare the ratio of reconstructed events as a function of the energy and of the zenith angle. In the upper-plot of figure 3.7 we can see this comparison for the Carmona strategy and in the lower-plot same ratio for the Aart strategy.

As can be seen the number of reconstructed events is lower for **d08** at low energies for both strategies. However this effect disappears for almost horizontal muons ($\cos\theta > -0.5$) due to the larger transversal dimension of the **d08** detector with respect the 10–string detector, which makes it more efficient in the reconstruction of horizontal tracks.

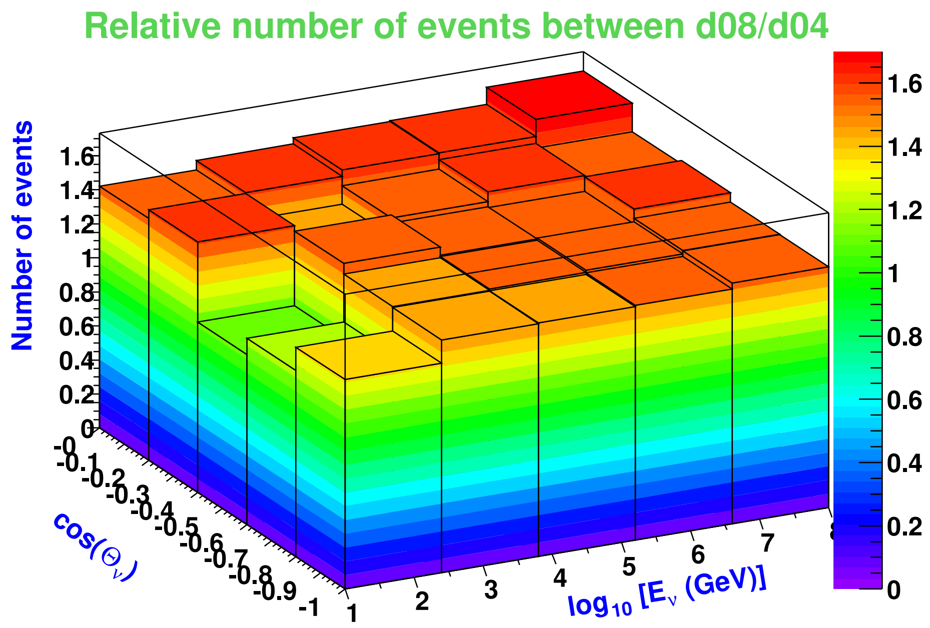

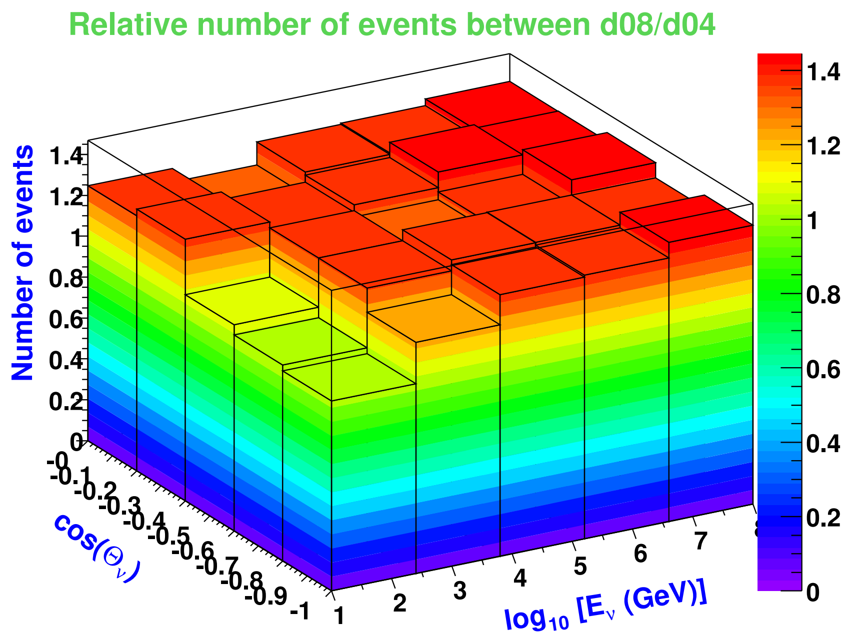

Figure 3.7: Ratio of reconstructed events in the **d08** and the **d04** detectors as a function of the neutrino energy and the cosine of the zenith angle for Carmona (upper-plot) and Aart (lower-plot) strategies.

3.2 Neutrino effective area

As explained in chapter 2, the ANTARES efficiency can also be expressed in terms of a neutrino effective area. Since both magnitudes (muon and neutrino effective areas) lead to a similar estimate of the telescope performances, it is natural to think that both variables will undergo the same effect in a more or less sizeable way. Nevertheless, these magnitudes are not proportional and different behaviours are expected for neutrino effective area and muon effective area. That is the reason why for the neutrino effective area the low energy effect seems to disappear as can be seen in figure 3.8 although in the two first bins of the low energy range the increase with respect to **d04** is less sizeable.

Another detail is that at high energy the increase of **d08** w.r.t **d04** is almost 35% whereas for muons this increase was of the order of ∼25%. This result, that at first sight may seem surprising, becomes clearer if we look into the definition of both effective areas. The muon and neutrino areas differ mainly in the factors that weigh the number of reconstructed events. These weights take into account both muon and neutrino cross-sections for each effective area and in the case of the neutrino effective area, a factor that takes into account the Earth's absorption. While the muon cross–section is almost flat at the energy range we are dealing, the neutrino cross–section increases quickly as function of the energy as can be seen in figure 3.9. When averaging over a given energy range (a bin) this steep increase makes the gain of neutrino effective areas become more significant at high energies. Also the Earth's absorption factor is important at higher energies since the 12–string detector will reconstruct more horizontal events.

3.2.1 Comparison to other detectors with 1080 PMTs

Before proceeding to the proposed 900–PMT detector, we need to confirm and settle the low energy response of the 12–string detector. As mentioned, the string configuration on the seabed could have an important influence in the detector response, in particular the distance between lines. To further investigate this idea, we estimated what we called the *string density* in order to have a guideline of what should be changed in the detector layout to avoid this low energy effect. To this end, other 12–string layouts have been proposed preserving the string design and therefore with a total of 1080 PMTs.

These new detectors are the **d11** and the **d12** detectors, whose layouts can be seen in figure 3.10

The **d11** detector layout also follows a geometrical shape, however, in this case all distances among strings have been reduced a 10%. The **d12** layout is an hexagonal string arrangement designed to keep a distance of 60 metres among strings. With these new designs we are able to perform a more detailed study of the detector response at low energies. Table 3.1 gives a summary of the detectors proposed up to now.

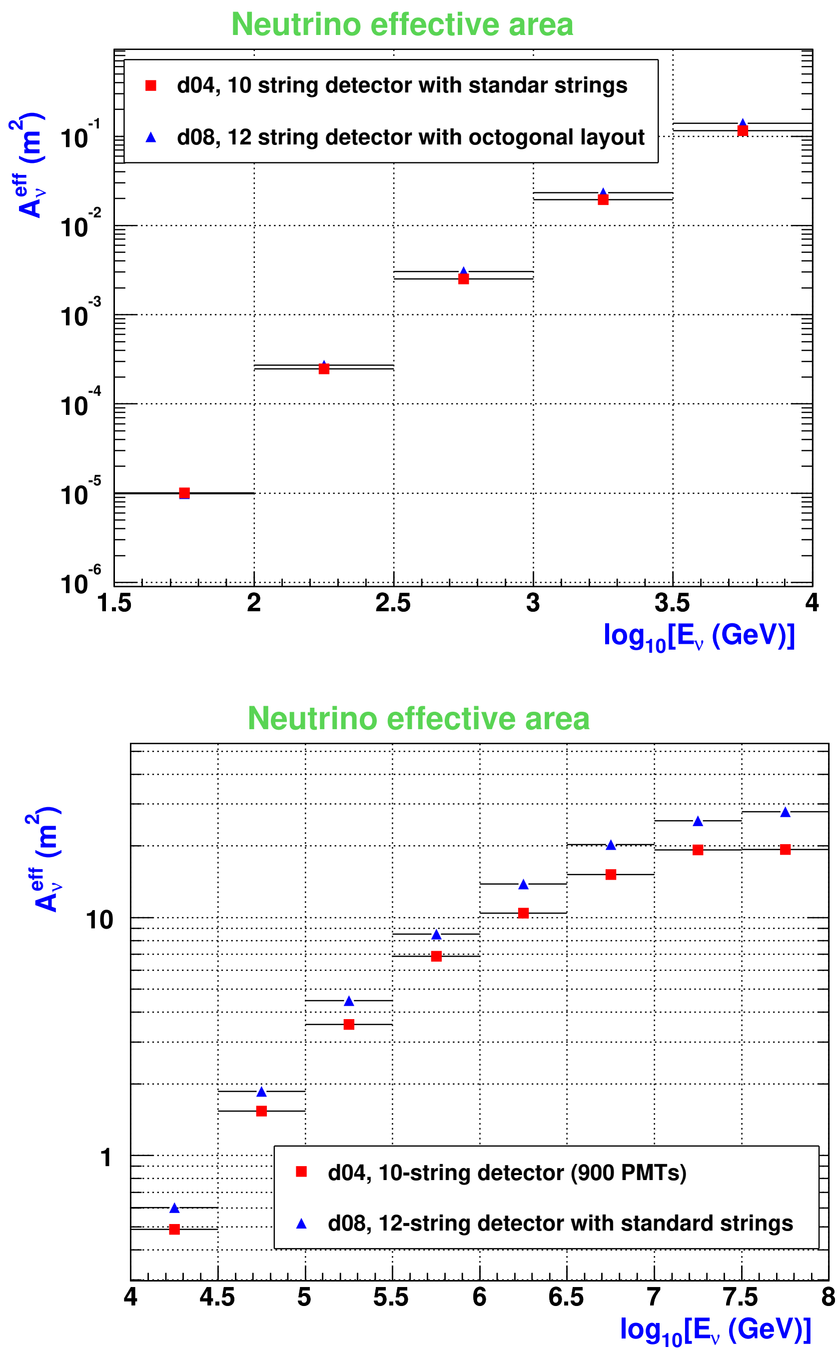

Figure 3.8: Neutrino effective area for the low energy $10 - 10^4$ GeV (upper-plot) and high energy $10^4 - 10^8$ GeV (lower-plot) ranges

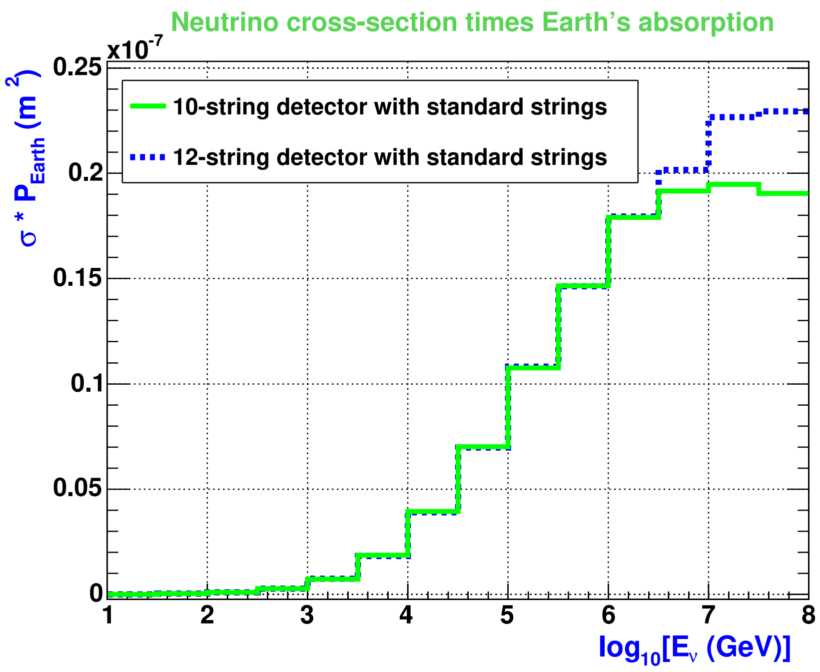

Figure 3.9: Neutrino cross-section times the probability to cross the Earth as a function of the neutrino energy.

Detector	No. of strings	No. of PMTs	No. of storeys	distance between storeys (m)	Layout	String design
d04	10	900	30	12	10–string TDR	*standard*
d08	12	1080	30	12	octagonal	*standard*
d11	12	1080	30	12	octagonal reduced	*standard*
d12	12	1080	30	12	hexagonal	*standard*

Table 3.1: Description of several 12–string detectors and the old 10–string detector.

Muon effective area

Once again the effective area for reconstructed muons is used to measure the detector's behaviour at low energies. As can be seen in figure 3.11 the low energy effect seems to disappear for the two new 12–string layouts proposed.

The increase in the muon effective area that we obtain is shown in the table 3.2. From these results, we can conclude that the low energy effect can be avoided reducing the string spread by shortening their distance. Nevertheless the trade–off is a lower

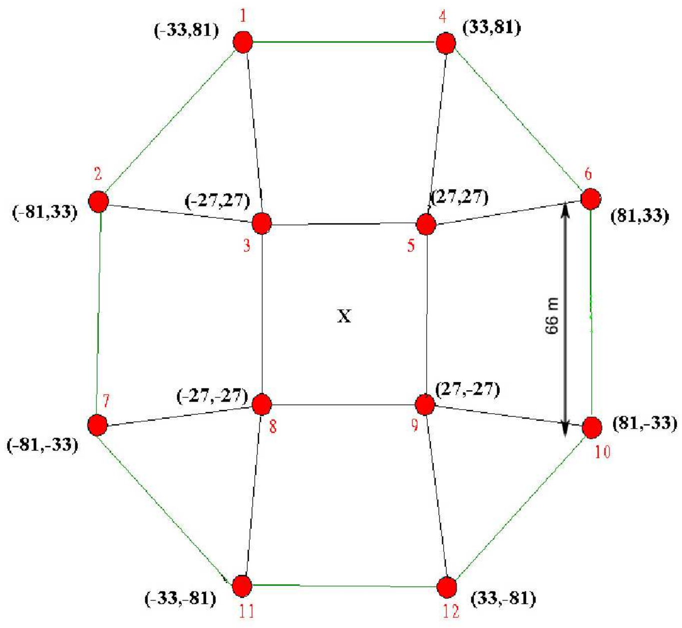

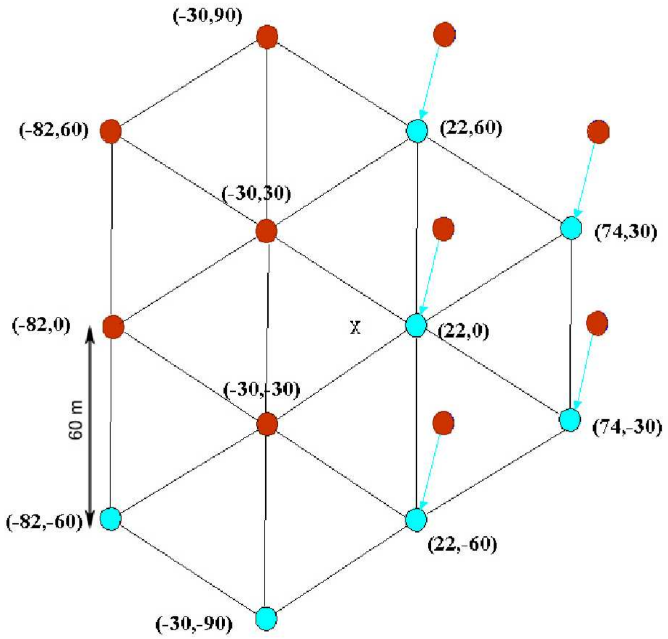

Figure 3.10: The reduced octagonal layout for the **d11** detector (left) and the new hexagonal layout of the **d12** detector (right).

efficiency at high energy where the ANTARES detector has its best performance as a neutrino telescope. All these results will be taken into account when designing a 900–PMT detector and a compromise will be looked for to guarantee a better response of the new detector.

3.3 The 12-string detector layouts with 900 PMTs

As we already mentioned, the aim of this research work is to increase the effective area and the efficiency of the ANTARES detector by adding two more strings but keeping the same number of PMTs. To follow this idea two string designs were put forward. These new string configurations correspond to the **d10** and **d09** detectors with the same layout at the seabed. In table 3.3 the main parameters of these new detector designs together with the 10–string detector and the previously proposed **d08** detector are shown.

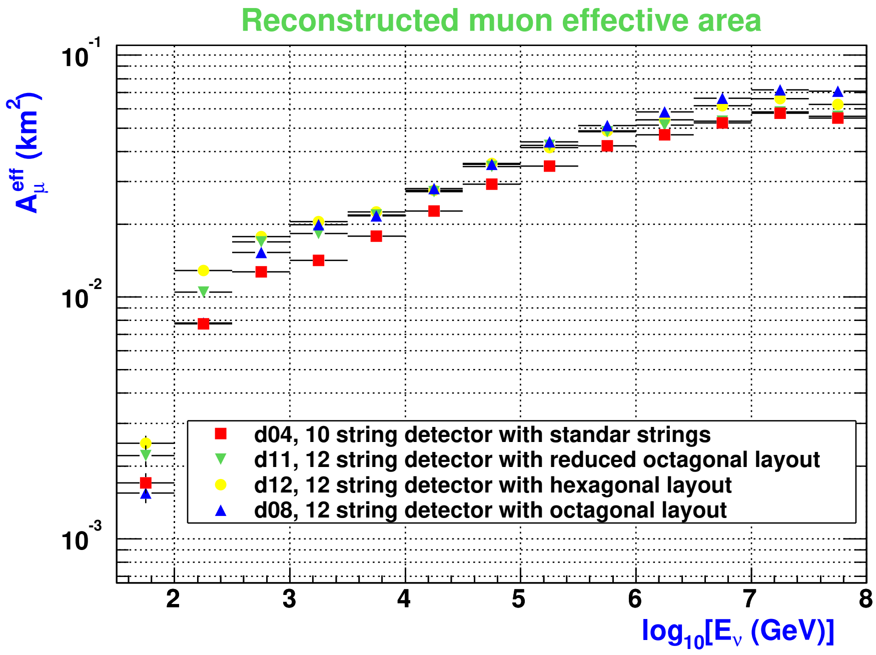

Figure 3.11: Muon effective area for all the 1080–PMT detectors and the 10–string detector **d04** with 900 PMTs for the Carmona strategy.

Detector	Low energies (10 to 10^4 GeV) w.r.t **d04**	High energies (10^4 to 10^8 GeV) w.r.t **d04**
d08	(0–1)%	25%
d11	38%	8 %
d12	40%	15 %

Table 3.2: Increase in the muon effective area of two different 12–string detectors with respect to the 10–string detector **d04** for the Carmona strategy.

Detector	No. of strings	No. of PMTs	No. of storeys	distance between storeys (m)	Layout	String design
d04	10	900	30	12	10–string TDR	*standard*
d08	12	1080	30	12	octagonal	*standard*
d09	12	900	25	12	octagonal	*chopped*
d10	12	900	25	14.5	octagonal	*sparse*

Table 3.3: Description of several 12–string detectors and the old 10–string detector.

The **d09** detector is just the **d08** detector with 25 storeys instead of 30, i.e. without the highest 5 storeys (called the *chopped* design henceforth). The **d10** detector has 25 storeys as well, but the distance between storeys has been increased in order to have the same height as **d08** and **d04**, 360 metres, and we call this string design *sparse*. Figure 3.12 shows the three proposed strings design up to now.

3.3.1 Muon effective area

The same plots for the **d08** detector were done for the **d09** and **d10** detectors using the 10–string detector as a reference. For the generation we used the same software and parameters as for the simulation of the full 12–string detector. Given that the effect at low energy is not due to the reconstruction algorithm used, from now on, we will use the Carmona strategy to reconstruct the events. In figure 3.13 the comparison between the muon effective areas of the three detectors in the whole energy range is shown, while figure 3.14 shows the same variable for the low and high energy regions.

The gain in the muon effective area for **d10** (*sparse*) at high energies (from 10^4 to 10^8 GeV) is about 15% with respect to the **d04**, while for the **d09** (*chopped*) the increase in the effective area is only about 6%. This suggests that the height of the detector has an important influence in the reconstruction of events, a fact that will be

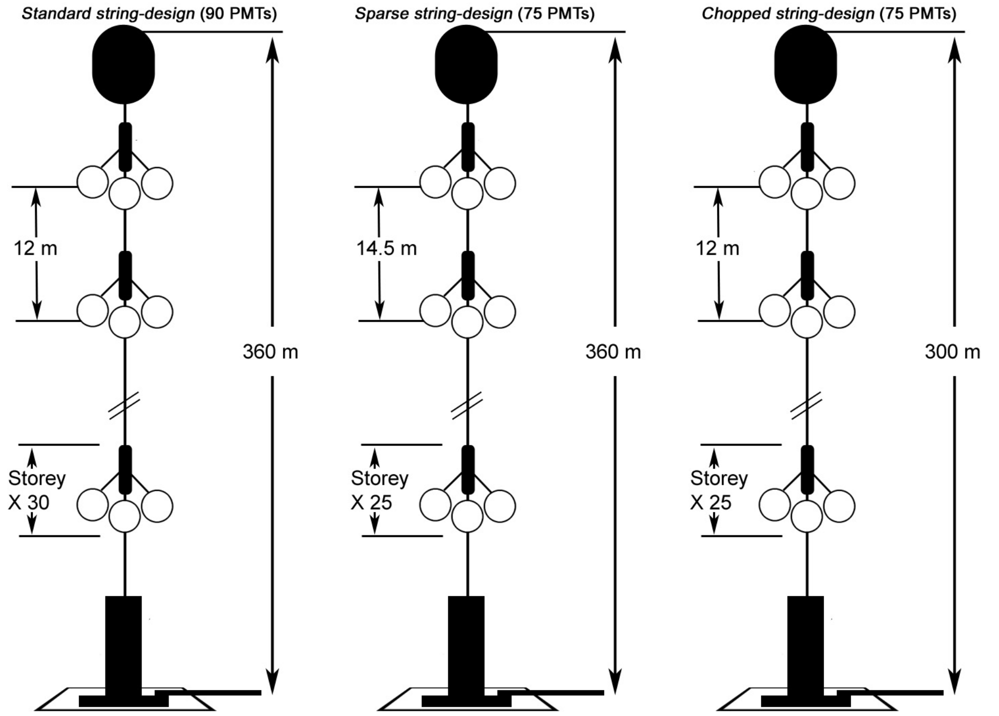

Figure 3.12: Comparison among the *standard* (left), the *sparse* (center) and the *chopped* (right) string designs.

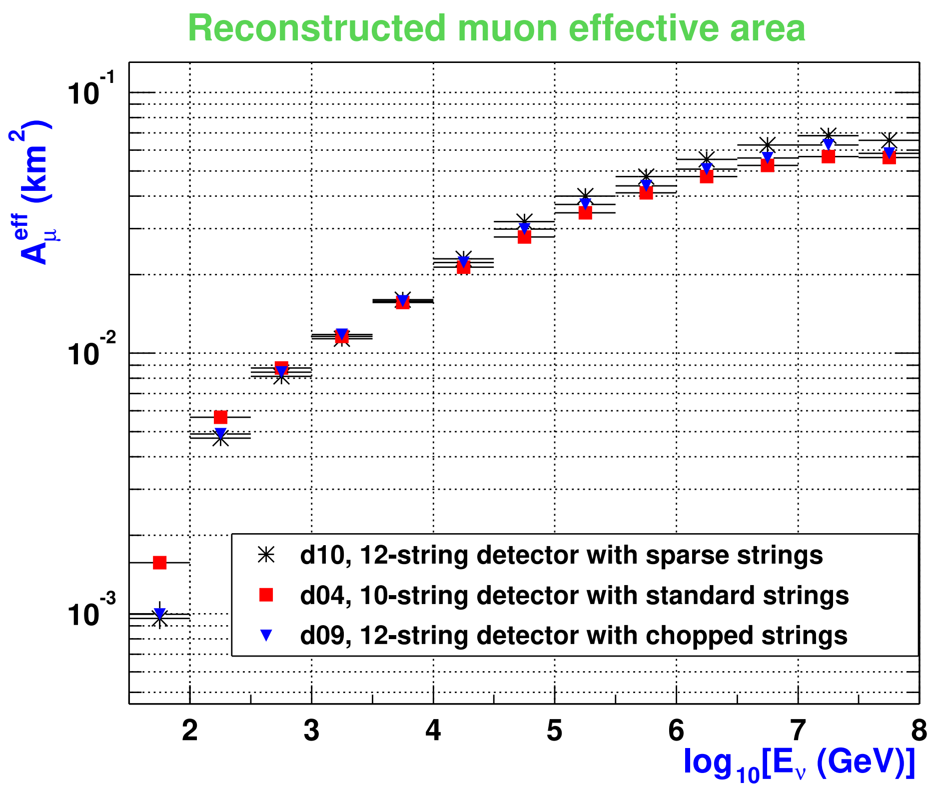

Figure 3.13: Effective area for muons as a function of energy for the different 900–PMT detectors.

confirmed in the following sections. As it can be seen in figure 3.14, (lower plot), an even larger effect happens at low energies. This is not unexpected since in the **d10** detector we have enhanced the distance between strings but also the distance between storeys, and consequently the distance from one PMT to another. **d09** is slightly better than **d10** at energies below $10^{2.5}$ GeV, what can be explained the same way as we justified the low energy effect for the 12-string detectors.

In figure 3.15 it can be seen the ratio of the muon effective area with respect to the **d04** detector. We summarize the increase in muon effective area for all these 900–PMT detectors in table 3.4 where these figures are given together with the **d08** detector in order to compare how much is lost reducing the number of PMTs from 1080 to 900.

Detector	Low energies (10 to 10^4 GeV) w.r.t **d04**	High energies (10^4 to 10^8 GeV) w.r.t **d04**
d08	(0–1)%	+25%
d09	-3%	+6%
d10	-3%	+16%

Table 3.4: Variation of the muon effective area of several 12–string detectors with respect to the 10–string detector **d04**.

From these values it can be seen that the loss of effective area at low energies is more marked for the 900–PMT detectors **d10** and **d09** as can be expected. Another important point is that differences between the *sparse* design of the **d10** and the *chopped* one for the **d09** do not show on the effective area for low energy. Both of them lose the same amount in efficiency at low energies. Nevertheless, these differences become remarkable at high energies, where for the **d09** there is an increase of hardly 6% with respect to the **d04** detector.

3.3.2 Number of reconstructed events.

We have also compared the number of reconstructed events for a signal with a *spectral index* of 2 ($d\Phi_\nu/dE \propto E^{-2}$). The normalization constant used has been set to the Waxman–Bahcall upper limit (2×10^{-4} GeV^{-1}m^{-2}s^{-1}sr^{-1}). Figure 3.16, shows that a large difference exists in the number of reconstructed events at energies between 10^4 GeV and 10^5 GeV, for the 12-string detector **d08** and its 900–PMT versions, the *sparse* **d10**, and the *chopped* **d09**. Moreover, because of the smaller number of reconstructed events for **d09** with respect to **d10**, it seems that the detector height is more significant to reconstruct events than the total number of PMTs.

It can be noticed from these numbers that there is about 5% more increase in the number of reconstructed events for the **d10** detector than for the **d09** detector, even

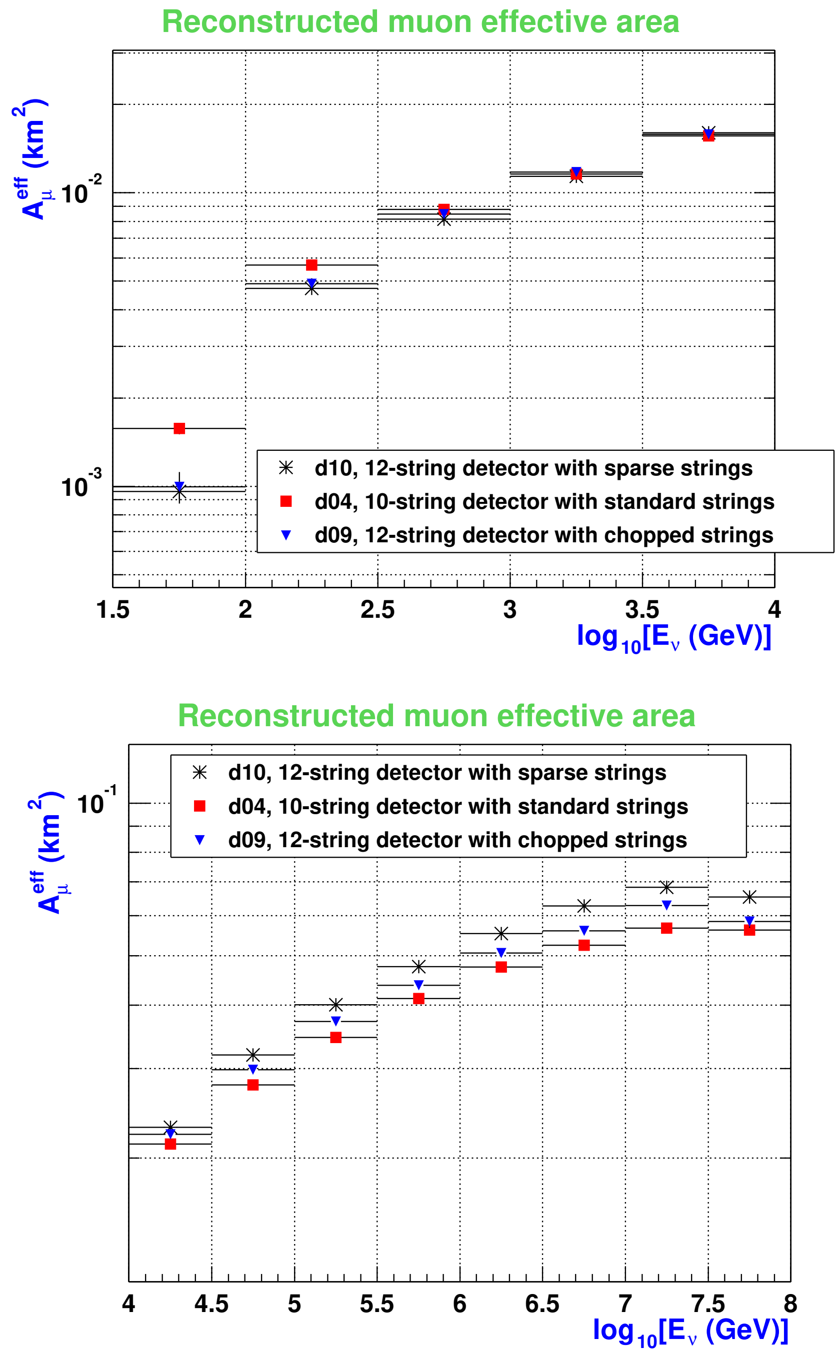

Figure 3.14: Muon effective area as a function of energy for the low energy range (upper-plot) and the high energy (lower-plot) range.

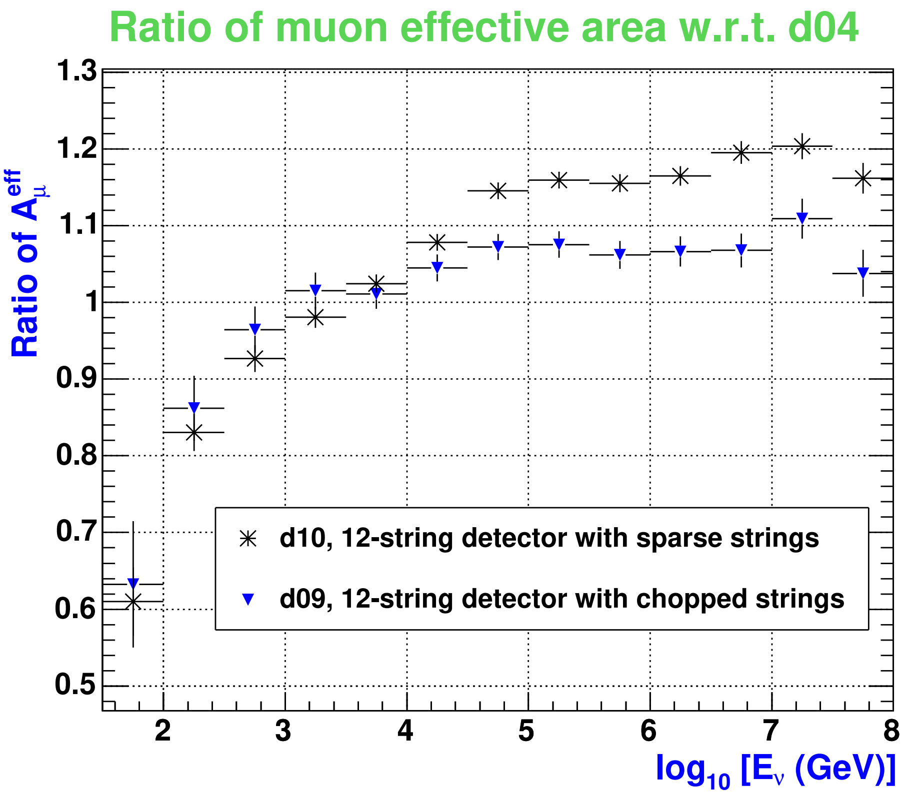

Figure 3.15: Ratio of muon effective area w.r.t the 10–string detector **d04** as a function of energy for the different 900–PMT detectors and the **d08** detector.

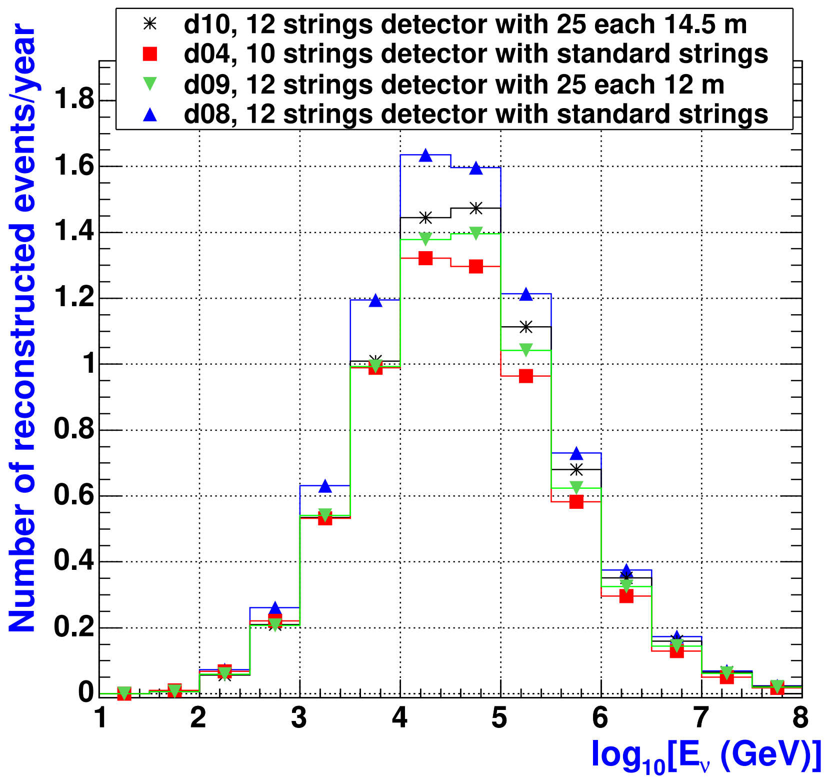

Figure 3.16: Number of reconstructed events per year for the different detectors.

though they both have 900 PMTs. These results confirm the importance of the detector height as pointed out in the previous section.

3.3.3 Angular resolution

In this section we are going to compare another important variable that has to be taken into account in a neutrino telescope like ANTARES. We are referring to the angular resolution defined in the previous chapter. There are two possible angular resolutions depending on which trajectories we use to compute the angle. The neutrino angular resolution also comprises the physical angle between the neutrino and the induced muon. In this section we will use the muon angular resolution that includes only the angular difference between the true and the reconstructed muons directions.

As we can see from figure 3.17 the muon angular resolution roughly follows the same trend for all the detectors.

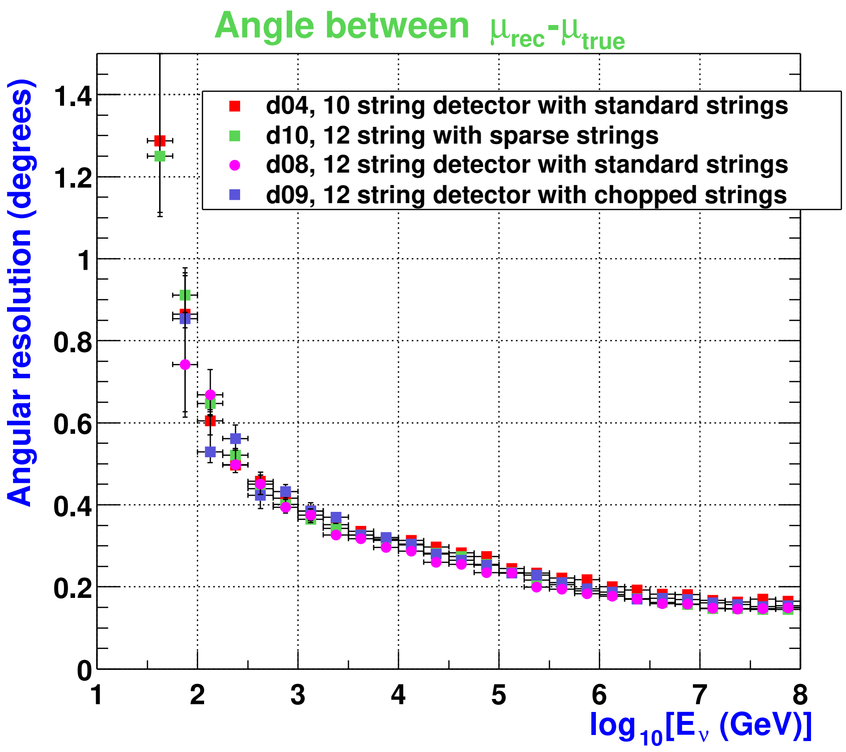

Figure 3.17: Angular resolution for the different detectors.

However, as can be seen in figure 3.18 from 10^4 GeV up to 10^8 GeV the angular resolution is better for **d08** than for **d04** by an average of 11%. The two 900–PMT versions of the 12-string detector, **d09** and **d10**, have better angular resolution with respect to **d04** at high energies by about 8% for **d10** and 6% for **d09**.

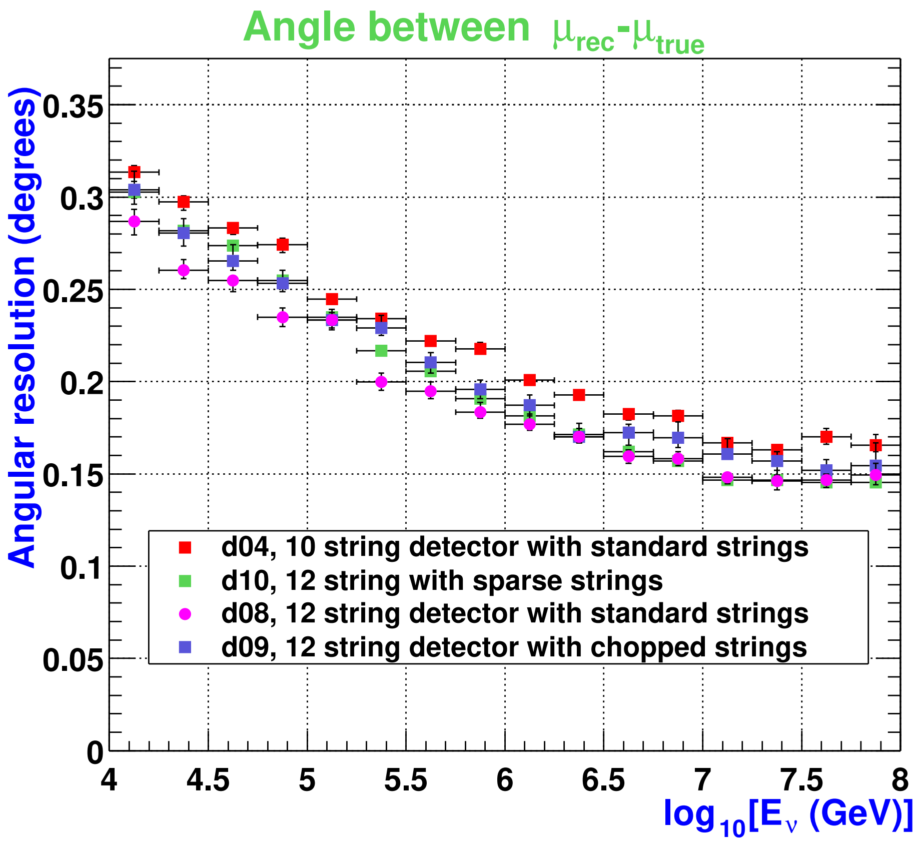

Figure 3.18: Blow-up of the angular resolution as function of the neutrino energy at higher energies.

3.4 The symmetry of the detector

When we proposed a new 12–string detector layout the first step was to follow an octagonal layout in order to ensure the isotropic response of the detector. However, this symmetry has to be confirmed by measuring the azimuth angle distribution for the reconstructed muon for an atmospheric neutrino flux. This distribution must be uniform for a symmetrical detector and can be fitted to a straight line. It is known that for the **d04** detector the response is not completely uniform in azimuth at low energies. In the case of atmospheric neutrinos, the response of **d04** is plotted in figure 3.19, (top-left), where a slight dependence on azimuth can be noticed. The same distribution can be seen for **d08** in figure 3.19, (top-right). In this case, the response of the detector is compatible with being flat in azimuth. Indeed, for the **d09** and **d10** detectors (figure 3.19 lower-left and lower-right) one can see that the response is also azimuth–independent.

3.5 Conclusions

We can summarize the results of this chapter as follows:

- Adding two more strings we have increased the muon effective area at high energies by about 25%. The increase of the effective area at this energies roughly scales with the number of strings.

- At the lowest energies the 12-string detector **d08** has approximately the same response than the 10-string detector **d04**. This effect appears using anyone of the two reconstruction strategies available.

- Nevertheless we checked that this effect disappears for detector layouts with higher strings densities (**d11** and **d12**), but the trade-off is a lower increase of the effective area at high energies.

- For the 900–PMT detectors we see that at high energies the increase in effective area of the *chopped* detector **d09** with respect to the standard 10–string detector **d04** is $\sim$ 6%, whilst the increase for the *sparse* 12–string detector **d10** w.r.t. **d04** is $\sim$ 16%.

- The loss at low energies is even more marked for this 900–PMT detectors. They have around 3% smaller effective area than the 10-string detector. This effect is seen independently of the reconstruction algorithm used.

- The number of reconstructed events in the whole energy range assuming a neutrino signal with spectral index of 2 increases in all 12-string detectors. However the highest increase is for **d08**, and the lowest is for the **d09** detector, i.e. the detector height has an important influence.

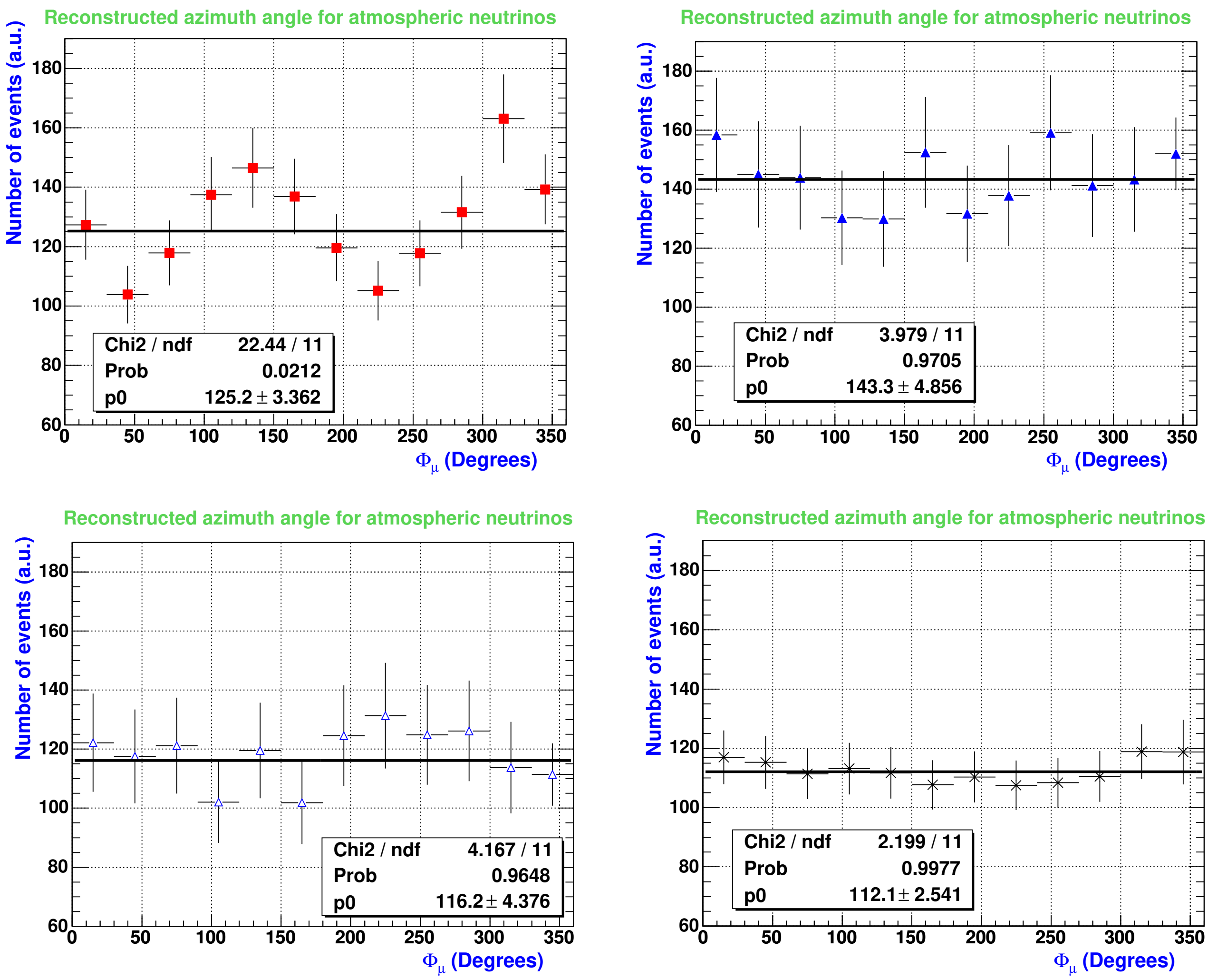

Figure 3.19: Azimuth angle distribution of the reconstructed muons for atmospheric neutrinos in the **d04** detector (upper-left), the **d08** detector (upper-right) the **d09** detector (lower-left) and the **d10** detector (lower-right)

- All the 12–string detectors have a uniform distribution in the azimuth angle.

Chapter 4

Further 12–string layouts and study of the reconstruction with the *single-line* strategy

In this chapter, we will propose additional 12–string detector layouts in order to make sure that we can avoid the problem at low energy. We will also take this study further by investigating how the proposed 12-string detector layouts respond when using the one-dimensional strategy, which is used by the ANTARES collaboration in order to search for neutralinos as well as for the neutrino oscillation studies. This kind of strategy is optimized for the low energy range, unlike the three-dimensional strategies used up to now, whose scope is the performance of ANTARES as a high energy neutrino telescope.

4.1 More 12-string detector layouts

We have seen that for all the 12–string detectors there is a slight loss of effective area at very low energies with respect to **d04** due to the increase in the distance among strings. For that reason other 12–string detector layouts were proposed. These new arrangements of the strings follow the criterion of having the same or higher *string density* than the old 10–string detector layout (remember that the *string density* for the **d04** detector was 0.603×10^{-3} strings/m^2). In figure 4.1 several 12–string detectors layouts with equal or higher *string density* can be seen.

There are three new layouts, the upper plot in figure 4.1 shows an hexagonal layout where we have reduced the distance among strings in certain parts of the layout. The two bottom plots are 12–string versions of the layout proposed in the Technical Design Report for a future 14–string detector. The idea is just to follow this 14–string layout but with only 12 strings on it to guarantee a possible upgrading to a 14-string detector in the future. In these two latter plots, the yellow dots (lighter grey on paper) represent the additional strings needed to form the 14–string layout.

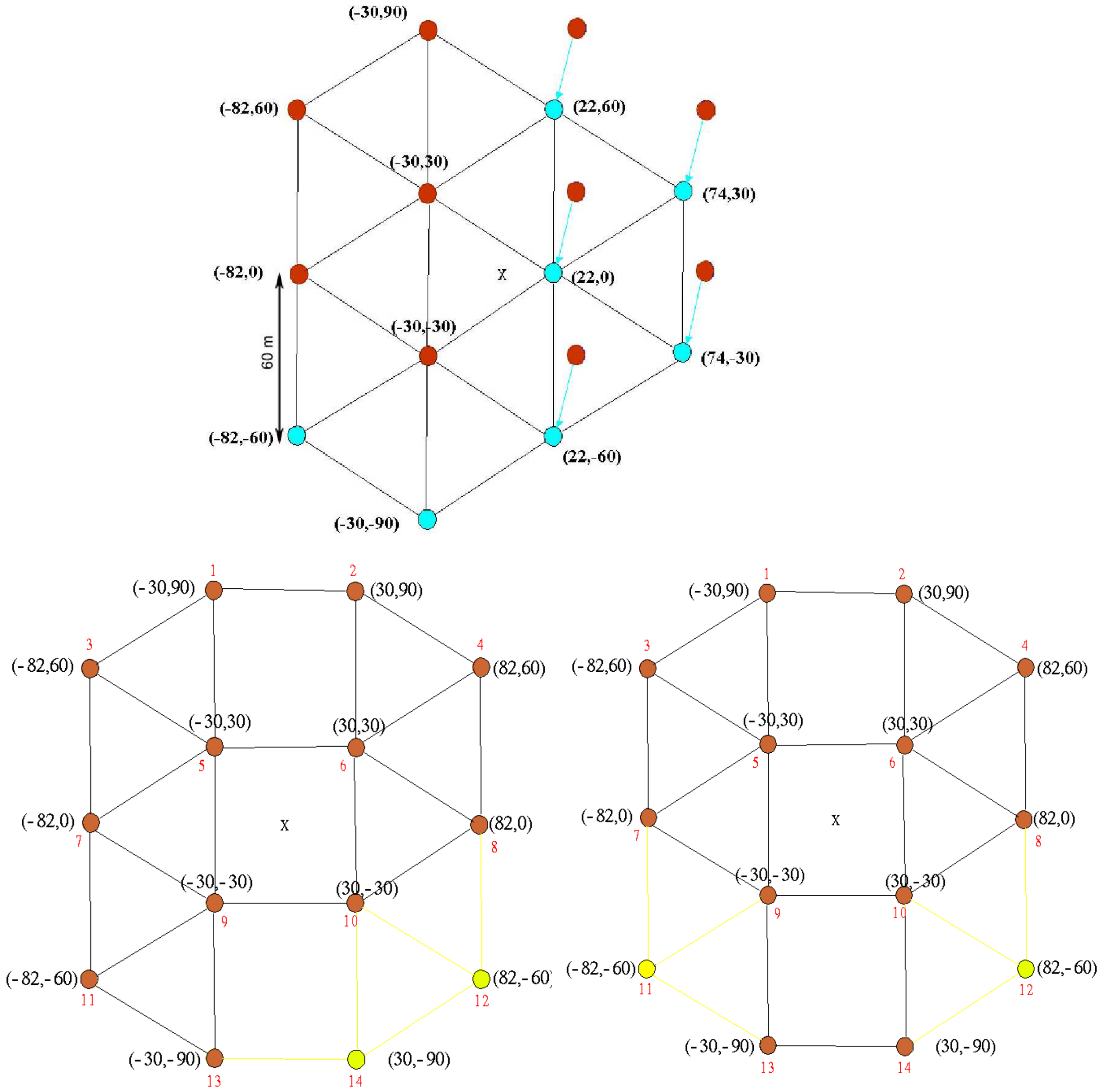

Figure 4.1: Layouts studied in this chapter. Upper plot: hexagonal detector **d13**. Lower plot left: The TDR asymmetrical detector **d15** and right: the TDR symmetrical **d18**.

In the previous chapter we have seen that the *sparse* string design seems to be the best configuration for a 900 PMTs detector. The detector height appeared as an important characteristic of the detector configuration. For that reason in this chapter we are going to concentrate in this string design for the new detectors. A summary of the specifications of the new 12–string detectors can be seen in table 4.1 together with the **d04** detector.

Detector	No. of strings	No. of PMTs	No. of storeys	distance between storeys (m)	Layout	String design
d04	10	900	30	12	10–string TDR	*standard*
d13	12	900	25	14.5	hexagonal	*sparse*
d15	12	900	25	14.5	TDR asymmetrical	*sparse*
d18	12	900	25	14.5	TDR symmetrical	*sparse*

Table 4.1: Description of more 12–string detectors and the old 10–string detector.

4.1.1 Muon effective area

Once again we compared the new 12–string detector among each other using the 10–string detector **d04** as a reference. In figure 4.2 the whole energy range can be seen, while in figure 4.3 the same comparison is shown at low (upper-plot) and high (lower-plot) energies.

In Table 4.2 the relative muon effective areas in percentage with respect to the **d04** detector are shown both at high and low energies.

Detector	Low energies (10 to 10^4 GeV) w.r.t **d04**	High energies (10^4 to 10^8 GeV) w.r.t **d04**
d13	+26%	+5%
d15	-1%	+11 %
d18	0%	+13 %

Table 4.2: Increase of the muon effective area of several 12–string detectors with respect to the 10–string detector **d04**.

As expected, the effect at low energies completely disappears for the more compact layout proposed, the hexagonal layout **d13**. The drawback however is that the increase in the muon effective area at high energies is only of 5%. This is something normal: if we reduce the distance among strings, we do not benefit from the addition of more strings. The balance between what we can gain at low and at high energies will be something crucial for the selection of the detector which better fit to the main goal

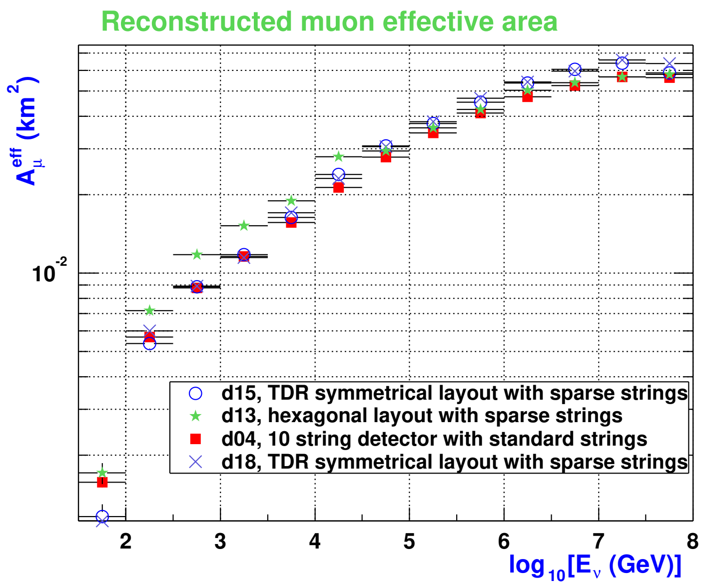

Figure 4.2: Effective area for muons as a function of energy for the different 900–PMT detectors.

of the ANTARES detector. Concerning both the TDR detectors, **d15** and **d18**, still suffer the low energy effect, this is something normal if we bear in mind that although we have preserve the *string density* of the **d04** detector we have enlarged the distance among storeys.

4.1.2 Angular resolution

It is expected that if the distance among PMTs is reduced a higher PMT density will be obtained and the angular resolution should increase. Nevertheless for the **d13** detector we have also shortened the detector size and therefore there would be fewer horizontal tracks reconstructed and the angular resolution will be influenced.

To see how the angular resolution changes we have computed it for these new detectors together with the 10-string detector **d04** (see figure 4.4).

The gain in the angular resolution for these three detectors is similar for all of them. Hence, the angular resolution is better in **d18** than **d04** by an average of 7% from energies of 10^4 GeV up to 10^8 GeV, as well as for the **d15** detector. The hexagonal layout detector **d13** has an increase of 6% with respect to the 10-string detector **d04** at high energies.

4.1.3 Number of reconstructed events

In this section we present the number of reconstructed events for a signal with *spectral index* of 2 for the new 12–string detector layouts. In figure 4.6 it can be seen

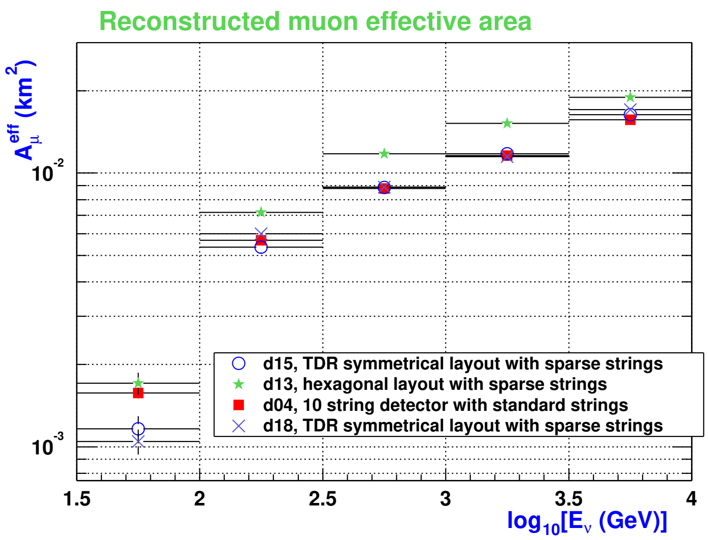

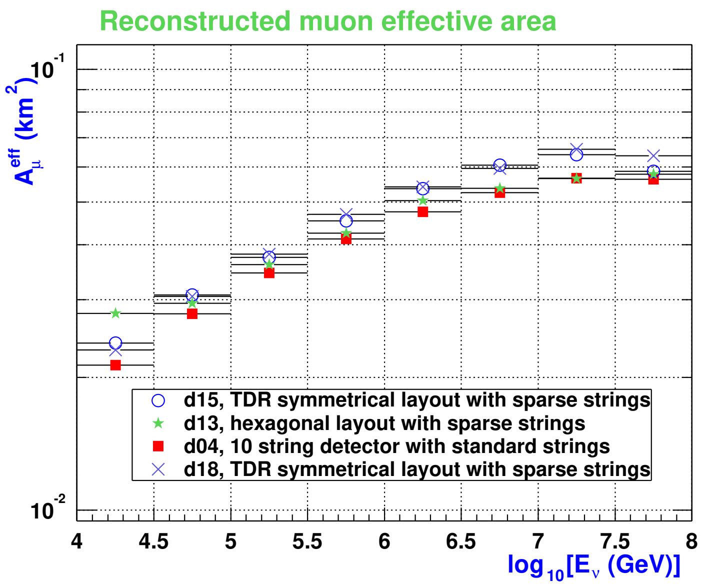

Figure 4.3: Blow-up of the muon effective area as a function of energy for different detector layouts for the low energy (upper-plot) and high energy (lower-plot) ranges.

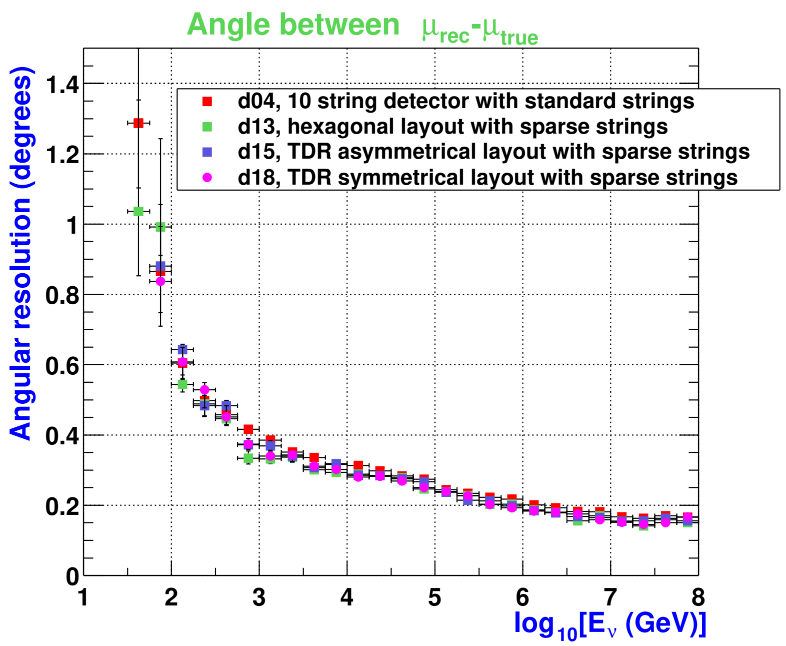

Figure 4.4: Angular resolution as function of energy for the different detectors.

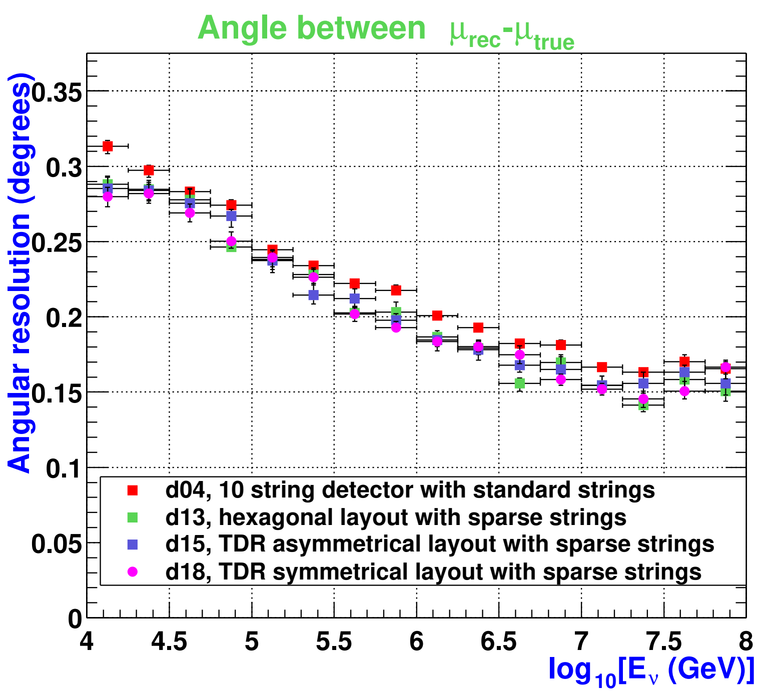

Figure 4.5: Blow-up of the angular resolution at high energies.

that both **d15** and **d18** detectors have a similar response, and in table 4.3 it can be noticed that the increase in the number of reconstructed events with respect to the **d04** are very similar. On the other hand, the hexagonal layout detector **d13** has a lower number of reconstructed events than the others and has only an increase of 2% (see table 4.3) with respect to the **d04** detector.

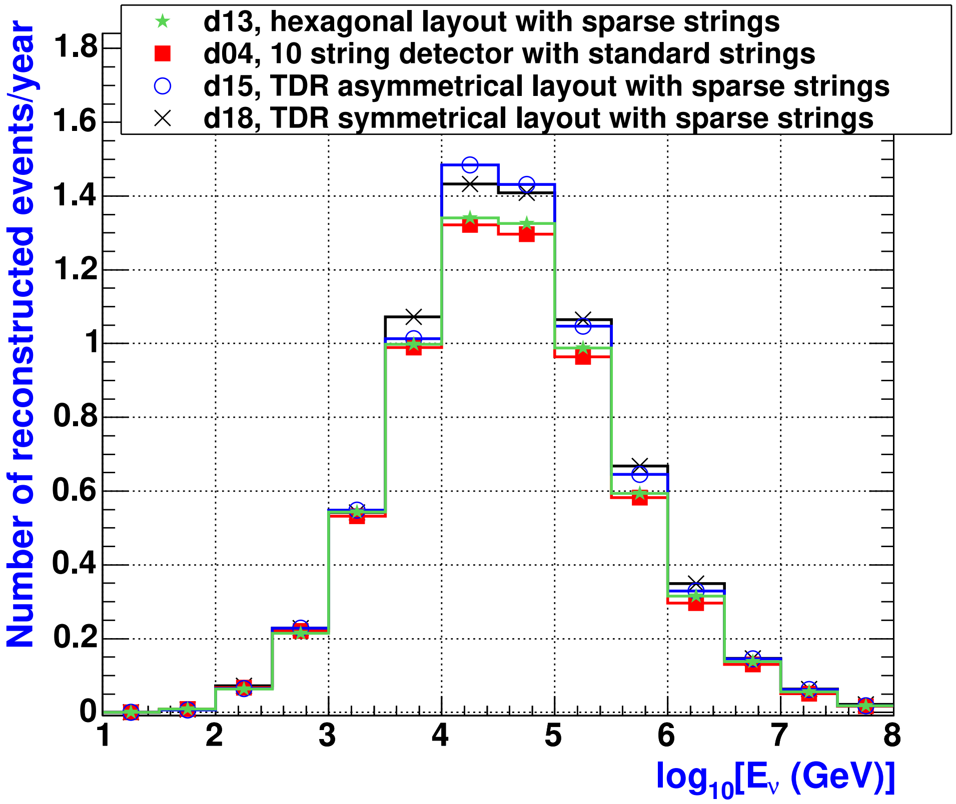

Figure 4.6: Number of reconstructed events per year.

In figure 4.7 the numbers of reconstructed events for all detectors we have studied up to now are summarized; these numbers are the integral number of reconstructed events for one year from a flux with spectral index of 2.

4.1.4 The azimuth distribution

The latter detectors studied in this chapter have a design slightly different from the octagonal layout. Once again the azimuth distributions of reconstructed events from an atmospheric neutrino flux will help us to check the symmetry of the new detectors. In figure 4.8 the azimuth distributions for the asymmetrical TDR layout **d15** (upper-plot), the hexagonal layout detector **d13** (lower-plot-left) and the symmetrical layout

Detector	Number of reconstructed events w.r.t **d04**
d13	+2%
d15	+8.4%
d18	+9.2%

Table 4.3: Number of reconstructed events for all the 12–string detectors with respect to the 10–string detector **d04**

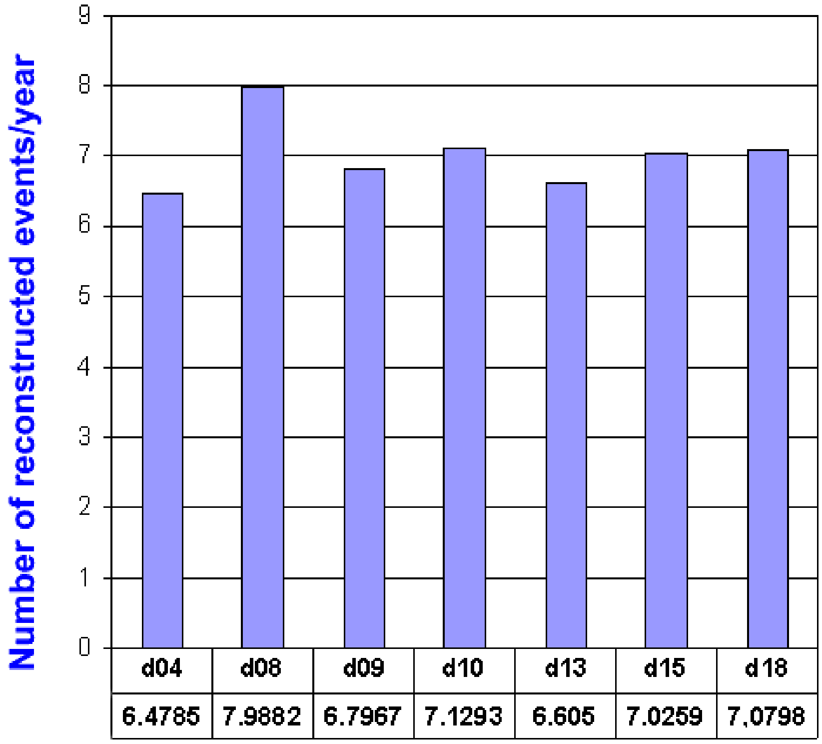

Figure 4.7: Number of reconstructed events for all detectors.

detector **d18** (lower-plot-right) can be seen. In this figure a fit to a straight line for each distributions is also shown. The **d13** and **d18** detectors have the responses that could be more easily fit to a straight line while the response of the asymmetrical detector **d15** is not completely flat.

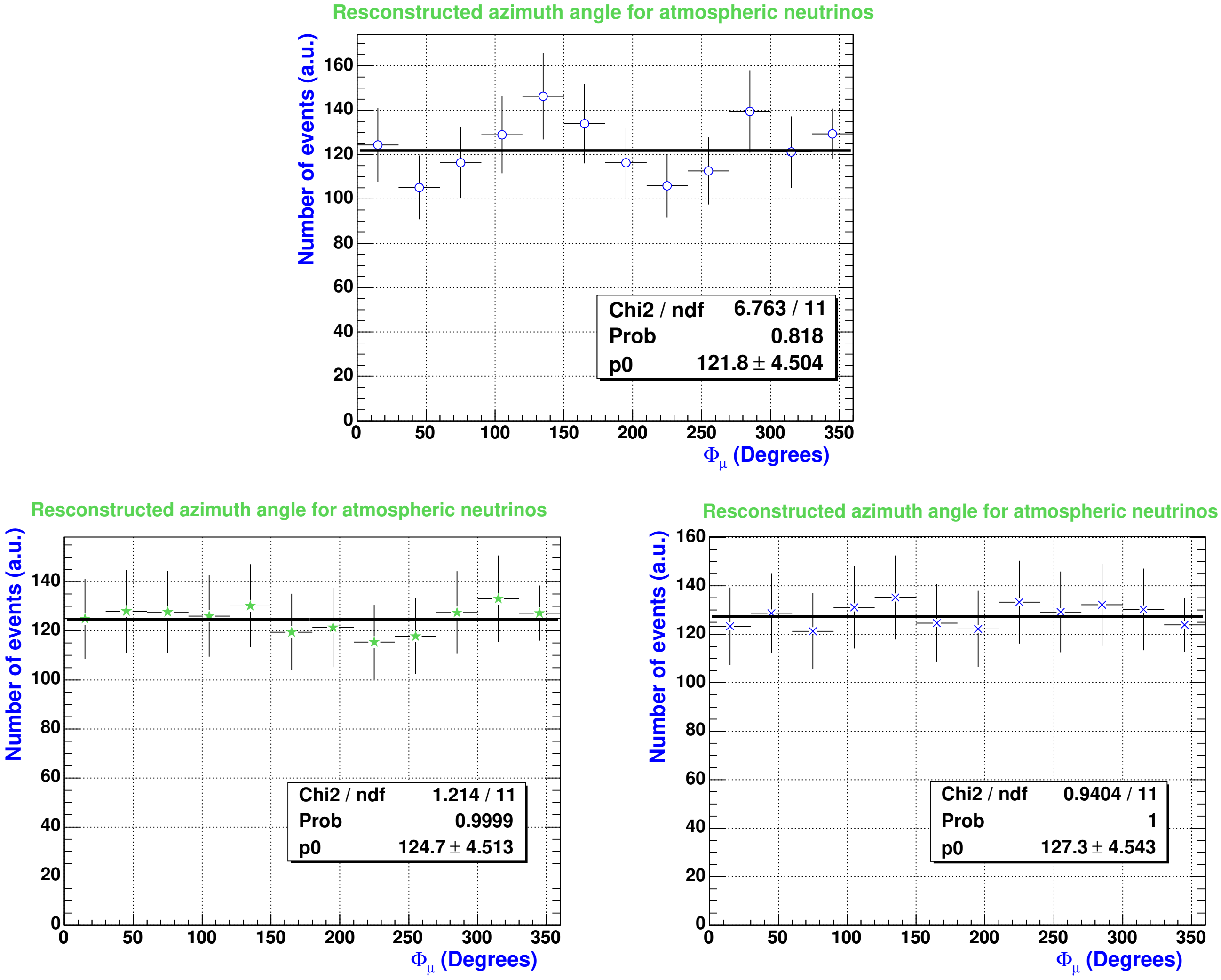

Figure 4.8: The symmetrical response for the three new 12–string detectors. The azimuth distribution for the **d15** detector (upper-plot), for the hexagonal layout detector **d13** (lower-plot-left) and for the symmetrical detector **d18** (lower-plot-right)

4.2 Reconstruction in one dimension

So far we focused ourselves in the performances of the new geometries using the 3D reconstruction strategies. However, it would be interesting to check how the storey arrangement may affect the 1-dimension (or *single-line*) reconstruction strategy. The ANTARES telescope has been optimized for the 100 GeV-10 TeV energy range, though the energy threshold for neutralino search is $\sim$ 25 GeV. We saw that at low energies the new 12–string layouts lose some efficiency when increasing the distance among strings. This effect may affect the neutralino search whose energy threshold is at the low energy range. Moreover, another factor that may affect the neutralino and neutrino oscillation search is the longer distance among PMTs in one single line. With all this in mind we have carried out another production using the OscStrategy 1D reconstruction. This strategy is a development version included in the RECO program. As already mentioned, this strategy uses the *hits* of only one string. It is therefore suitable only for vertical or low energy muons near the string. For that reason this strategy is used for the search of neutralino as well as for neutrino oscillations.

4.2.1 Number of reconstructed events

The 1D reconstruction is used for the atmospheric neutrino flux instead of a signal with spectral index of 2 and thus the comparison among the number of reconstructed events is done using this flux which is more relevant for the kind of studies made at low energy. As only one string is used to reconstruct events, the arrangement of the strings on the seabed, the layout, does not take part in the reconstruction strategy. Furthermore the number of strings is not important to a first approximation, although it may have some influence since the first step in this strategy is to perform a selection of the string that after the *hit* selection contains the highest number of *hits*. Therefore the number of strings may have a slight influence in the reconstruction strategy.

This strategy has not well defined cuts since they depend on the physics you aimed at. For this comparison we have used a set of selection cuts based on those used by the developers of this strategy:

- The number of *hits* (nhits) is greater than 5
- A cut in the Chi-square of the fit procedure: $\chi^2/(nhits - 5) \leq 2.4$
- We have not imposed any selection criterion in the zenith angle.

In figure 4.9 the comparison in the whole energy range between the three 12–strings detectors with different string design and the 10–string detector **d04** is shown.

As can be seen, the importance of the distance between storeys becomes now patently clear. Among the 25-floor arrangements, the *sparse* configuration (the **d10** detector) looks worse for the 1D event reconstruction. It is not surprising if we bear in mind that with this string configuration we have not only increase the distance between storeys and therefore the distance among PMTs, but we also have fewer number of PMTs per string (75 PMTs) than the standard string design (90 PMTs). So, with this design we have a loss of about 20% in the number of reconstructed events with respect to the **d04** detector. With the *chopped* string arrangement, there is a gain of

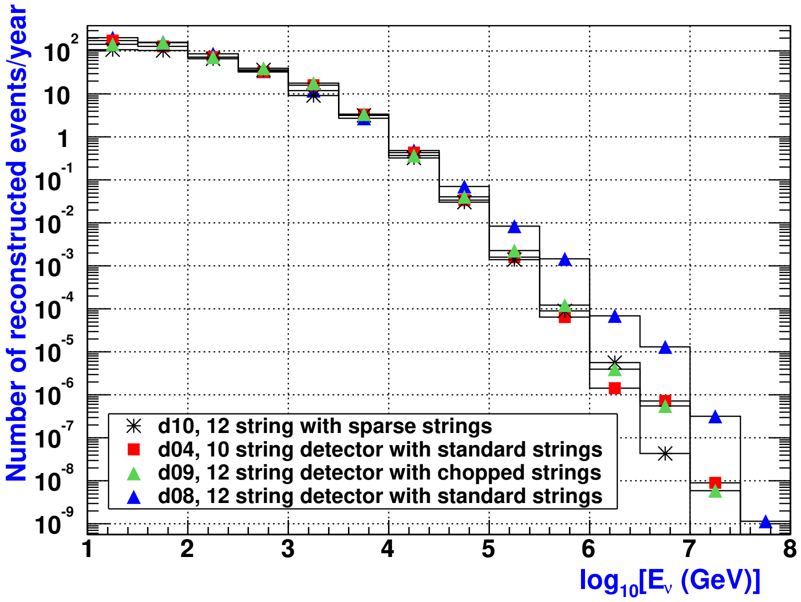

Figure 4.9: Number of reconstructed events per year for 1D reconstruction.

barely 2% w.r.t the **d04** detector. This means that the loss due to a lower number of PMTs per string is slightly over-balanced against the two strings added. In other words, the relative decrease in the length of the strings (about 16%) is smaller than the relative gain in the number of strings (about 20%). This ratio can be clearly seen if we compute the increase in the number of reconstructed events for the 12–string and 1080 PMTs detector **d08**. We see that it has an increase of roughly 18% w.r.t the 10–string detector, what is expected from the addition of just two more strings.

However, in figure 4.10 right, it is shown that this increase is more significant at high energies, and as this reconstruction strategy has the best performance at low energies, it seems that the reduction on the number of PMTs per string will not affect seriously the performances of the *single-line* strategy. However a more detail study about the goals of this strategy under these layouts has to be done.

4.2.2 Zenith angle reconstructed

As already mentioned, this strategy is optimized for the reconstruction of almost vertical down-going neutrinos (atmospheric neutrinos). Therefore, a good accuracy in the zenith angle measurement is needed. That is the reason why we are going to study thoroughly the features of this strategy depending of the detector layout, instead of studying the performances of the detector itself. As just said the most important variables in the *single line* strategy are the accuracy of the reconstructed zenith angle, the number of events reconstructed and the number of events after applying the selection

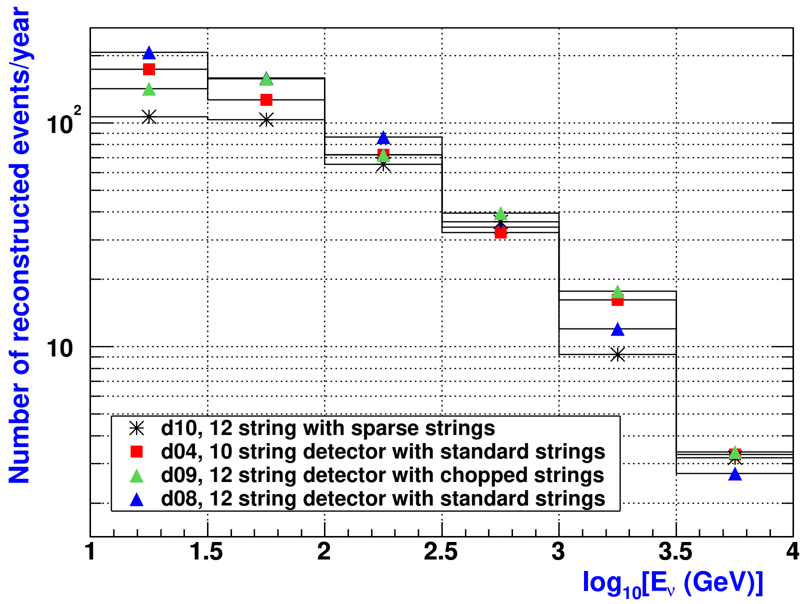

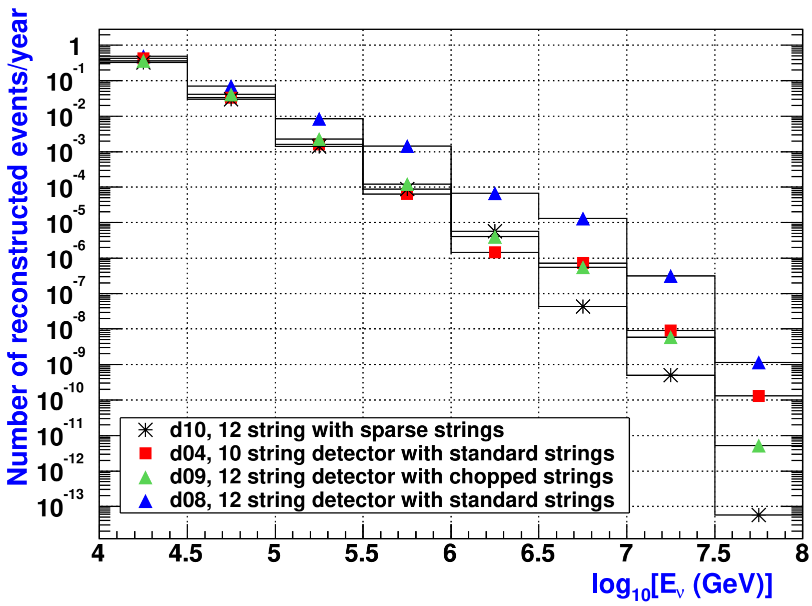

Figure 4.10: Blow-up of the number of reconstructed events as function of the neutrino energy for the low energy (upper-plot) and high energy ranges (lower-plot).

criteria.

In figure 4.11 it can be seen the true zenith angle distribution versus the reconstructed one, for all the strings design including the two versions of the *standard* design the one with 12–string (the **d08** detector) and the one with 10 string (the **d04** detector).

In these plots it can be seen that for all the strings design and for the 10–string detector **d04** the reconstructed track angles lie along a straight line. In table 4.4, are shown the numbers of events from the generation flux ($\sim E^{-1.4}$) without re-weighted by any accepted neutrino flux, at different reconstruction levels. As expected the *standard* string design with 12–strings reconstruct the highest number of events at both levels. It can be noticed that the number of selected events per line is almost the same for both *standard* detectors (**d08** and **d04**) as expected. Concerning the strings design for a 900–PMT detector with 12 strings, the *chopped* string design has a decrease of only ~ 1.5 % w.r.t. the *standard* string design, whilst the *sparse* string design is the least effective when events are reconstructed by means of this *single-line* strategy.

String design	Number of events at reconstruction level	Number of events at selection level	Number of events/line (selected)
standard (d08)	149585	2761	230
standard (d04)	123863	2219	229
chopped (d09)	128417	2716	226
sparse (d10)	135938	2092	174

Table 4.4: Number of events at different steps in the *single-line* reconstruction strategy.

In order to see the accuracy of this zenith angle reconstruction, figure 4.12 shows the difference between the Monte Carlo angle and the reconstructed one.

As can be seen all the detectors seem to perform a good zenith angle reconstruction. That leads us to think that the reconstruction features do not seem to have a deep influence in the string design. Moreover, as it can be seen from the numbers of reconstructed events at each reconstruction level, with two additional strings the reduction of the number of storeys (from 30 to 25 storeys) is not significant for the reconstruction strategy if the distance between storeys is kept. According to that, we see that taking into account the number of reconstructed events from an atmospheric neutrino flux the *sparse* string design turn out to be the worst detector in terms of reconstructing events. This an important point to bear in mind when it comes to chose the best detector layout and geometry for the future ANTARES telescope. There is a trade-off between the best features of experiment as a neutrino telescope and a neutrino oscillation and neutralino detector.

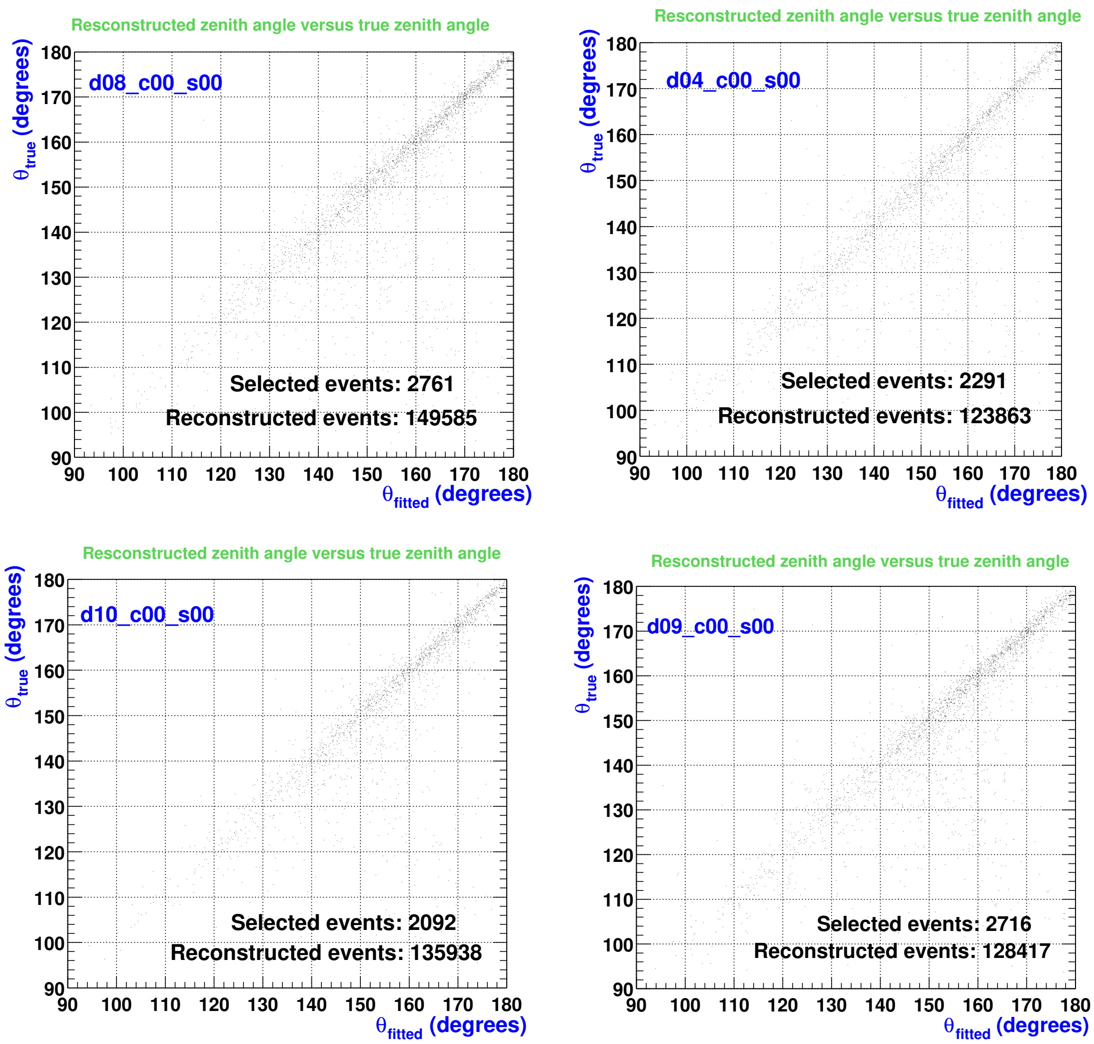

Figure 4.11: Reconstructed zenith angle versus the true zenith angle for the *standard* with 12 strings (top-left) the *standard* with 10 strings (top-right), the *sparse* (bottom-left) and the *chopped* string design (bottom-right), numbers of events after reconstruction level and after passing the selection cuts are also shown.

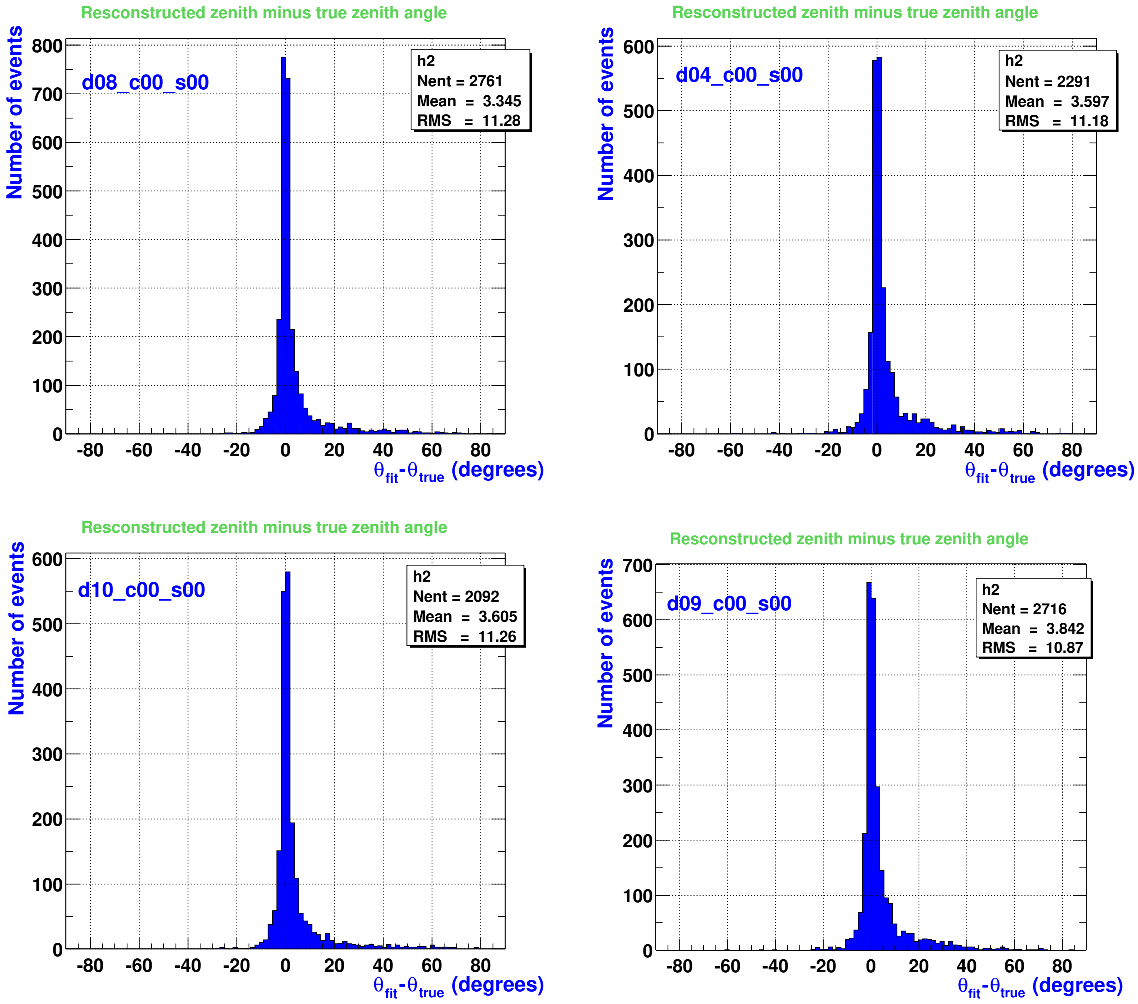

Figure 4.12: Difference between the true and the reconstructed zenith angle at selection level for the *standard* with 12 strings (top-left) the *standard* with 10 strings (top-right),the *sparse* (bottom-left) and the *chopped* string design (bottom-right).

Conclusions

With this study we have surveyed how we could increase the efficiency of the ANTARES telescope by increasing the number of strings but preserving the number of PMTs. This is important since new recent incorporations to the ANTARES Collaborations advocates for a new detector layout with two more strings. The decision of whether this should be done or not is very important and the choice of the new detector layout has to be done taking into account every particularity of the ANTARES telescope and the software machinery.

New detector layout

In chapter 3, we have presented the first approach to the study of the new 12–string detector layouts. This approach was done in a first level by just adding two more strings to the up to now official detector **d04**. This first study was done using the **d08** detector. Once we have computed the main magnitudes that better describe the detector response for this new layout, the next step was to reduce the number of PMTs from 1080 to 900 PMTs. New *intra–string* designs were proposed following this idea. We have also surveyed the effect of effective area loss at low energies due to the increase in the average distance between strings. Some first outlooks were also presented which can be summarized as follows:

- The increase in the effective area seems to scale together with the number of strings.
- There is a common behaviour at low energies for the **d04** and the **d08** due to the longer distances among strings in the latter detector.
- This effect disappears with detectors with more *string density* but we lose the increase at high energies.
- Comparing among the 900 PMTs we can conclude that the detector height is an important factor to be taking into account in the detector response.
- All 12-string detectors seem to have a better isotropic response than the old **d04** detector.

More 12–string layouts and the *single-line* reconstruction

In the chapter 4, there were proposed more 12–strings layouts. These layouts follow the idea of shortening the distance among strings (**d13**) or keeping the same layout and just adding two more strings (**d15** and **d18**). Also in this chapter a study of the *single-line* reconstruction strategy were presented. This strategy was developed to search for neutralino and the study of the neutrino oscillations. The energy range for this physics is different than the energy range in which ANTARES performs as a neutrino telescope. As this strategy uses only one single line to perform the reconstruction should be more sensitive to the string design proposed in the previous chapter. This study was done in order to see how these *intra-string* design may affect to the 1D reconstruction strategy. The results obtained are the following:

- New detector layouts have better muon effective area in all energy range w.r.t. the old 10–string detector **d04**.
- Furthermore the increase in the low energy range is about $\sim$26% w.r.t. **d04** for **d13** and **d15** even larger than the increase at high energy (less than 15%). Whereas the symmetrical layout **d18** behaves almost the same than the **d04** detector.
- With these new detectors we do not take the advantage of having two more strings.
- Angular resolution does not suffer a large increase for these layouts w.r.t the 10–string detector.
- The azimuth angle distribution follows a linear trend except for the asymmetrical layout **d15** where one can make out an angle dependence in the azimuth distribution.
- Comparing the number of reconstructed events from an atmospheric neutrino flux with the *single–line* reconstruction strategy for the different *intra–string* design, we see that the *sparse* configuration have a loss of -20% w.r.t. the *standard* and 10–string detector. On the other hand, the *chopped* string design has an increase of 2% and the fully *standard* detector has an increase of 18% that seems to scale with the number of strings added.
- As regards the 900–PMTs detectors the **d09** detector (*chopped* string design) looks better than the **d10** detector (*sparse* string design) using the *single–line* strategy.
- If we compare the strategy performances at different reconstruction levels we see that the *sparse* 12–string detector **d10** is the worst in order to reconstruct events

at the selection level, although all 900–PMTs detector reconstruct almost the same number of events before applying the selection cuts.

- Concerning the strategy accuracy we see that all, included the old 10–string detector, perform a good reconstruction.

In order to choose a detector among the 900–PMTs detectors we see that there is a trade-off of what we wants to gain at high energies and at low energies. The detector performances depend on the energy range, therefore, there is a physical question attached to the detector election. Taking into account the neutralino searches and the neutrino oscillation studies, the **d09** detectors appears as the best option, with the drawback of not being a good layout for astronomical sources detector. In that case the **d10** detector is among the 900–PMTs detectors the best one.

Resumen

Este Trabajo de Investigación examina la posibilidad de aumentar la eficiencia del detector ANTARES cambiando su geometría. Para tal fin, se proponen nuevas configuraciones geométricas del detector, a la vez que nuevos diseños internos de línea. Todo ello siguiendo la restricción de conservar el número de fotomultiplicadores al número actual de éstos en el detector (900 PMs).

Astronomía de neutrinos

La astronomía tradicional basada en la detección de fotones ha permitido explorar el Universo en un gran abanico de longitudes de onda del espectro electromagnético. Este rango se extiende desde longitudes de onda de radio ($\lambda \sim 10^4$ cm) hasta los rayos gamma del orden del TeV. Estos últimos han supuesto recientemente un nuevo empuje a la astronomía de fotones. Gracias al esfuerzo realizado durante décadas en este campo se han conseguido importantes hallazgos en el rango de altas energías como el descubrimiento de las explosiones de rayos gamma (GRBs) y el estudio de las galaxias de núcleo activo (AGNs) por mencionar algunos de ellos. Sin embargo, la astronomía de fotones sufre de una gran desventaja a la hora de explorar el Universo más allá del TeV. Los fotones de mucha energía interaccionan con el fondo de radiación de microondas, produciendo pares electrón–positrón, dando lugar a que fotones con energías mayores que el TeV recorran distancias de apenas unas decenas de Mpc (la distancia al cúmulo de Virgo es de $\sim$ 20 Mpc). Existen otros problemas como el hecho de que regiones densas del Universo no pueden ser observadas con este tipo de astronomía debido a la interacción que sufren los fotones con la materia.

Si recurrimos a los protones como posibles portadores de información a grandes distancias, encontramos que éstos también interaccionan con el fondo de radiación de microondas, fenómeno conocido como el corte GZK [2]. Asimismo, los protones, al ser partículas cargadas pierden su información direccional debido a la desviación causada por los campos magnéticos intergalácticos lo que impide cualquier intento de búsqueda de fuentes puntuales.

La astronomía de neutrinos es una disciplina reciente que nace del hecho de considerar a los neutrinos como posibles mensajeros de información para observar el Cosmos. Los neutrinos, al igual que los fotones, son partículas neutras y estables. Sin embargo, a diferencia de los fotones y protones, los neutrinos interaccionan débilmente y apenas son absorbidos en su paso por regiones densas del Universo. Tampoco interaccionan con los fotones del fondo de radiación de microondas, lo que los convierte en un candidato ideal para una nueva astronomía basada en neutrinos, complementaria a las observaciones realizadas en el rango óptico. Así pues, muchas de las hasta entonces inaccesibles fuentes de la astronomía tradicional, son ahora el principal objeto de estudio de la astronomía de neutrinos. Sin embargo, los neutrinos son partículas con baja sección eficaz que interaccionan muy débilmente, por lo que para poder detectarlos se precisa la construcción de grandes telescopios que tengan por blanco un material denso que favorezcan su detección. Una de las propuestas para la construcción de telescopios de neutrinos consiste en usar grandes medios como el agua o el hielo como blancos de detección. La colaboración ANTARES [37], siguiendo esta idea, trabaja en la construcción de un telescopio de neutrinos en el fondo del mar Mediterráneo para el estudio de fuentes astrofísicas de neutrinos.

Fuentes de neutrinos

Los objetos astrofísicos que presumiblemente emiten neutrinos son numerosos. Algunos de los fenómenos de producción de neutrinos son fuentes garantizadas, como por ejemplo, los neutrinos producidos por la interacción de los rayos cósmicos en las capas altas de la atmósfera. En este caso se habla de neutrinos atmosféricos y son una de las fuentes irreducibles de fondo para un telescopio de neutrinos astrofísicos.

Por otro lado, aquellos escenarios donde se produce la aceleración de protones se consideran también posibles fuentes de neutrinos. Los protones son constituyentes mayoritarios de los rayos cósmicos, y son unos de los principales candidatos a ser acelerados a altas energías en objetos astrofísicos. Del mismo modo en que los neutrinos se producen en la atmósfera terrestre, también se pueden producir a partir de estos protones en reacciones que tienen lugar en el interior o en la inmediaciones de los objetos astrofísicos donde son acelerados, o incluso en el espacio intergaláctico. Estos neutrinos astrofísicos constituyen la señal que se espera medir en un telescopio de neutrinos como ANTARES.

Existen numerosos modelos que predicen la emisión de neutrinos de alta energía en fuentes astrofísicas. Se puede hacer una distinción entre los modelos que explican la aceleración de partículas cargadas mediante mecanismos como la aceleración de Fermi, los modelos *bottom-up*, y los modelos que teorizan con la existencia de partículas superpesadas cuyas desintegraciones darán lugar a partículas aceleradas, los modelos *top-down*. En ambos modelos los neutrinos aparecen bien como producto de desintegración de las partículas cargadas aceleradas (modelos *bottom-up*), o bien directamente como resultado de la desintegración de partículas superpesadas (modelos *top-down*). Estos últimos modelos surgen como explicación a los indicios existentes de un flujo de rayos cósmicos por encima del corte GZK, e implican una física más exótica. Gracias a la astronomía de rayos gamma se tiene evidencia de la existencia de una aceleración de partículas en fuentes astrofísica. La cuestión de si podrían producirse neutrinos en ese tipo de escenarios depende de si las partículas cargadas aceleradas son leptones, en cuyo caso no se producirían, o por el contrario son protones, situación para la cual se espera un flujo de neutrinos en la dirección de la fuente. Entre las posibles fuentes de neutrinos cuyo origen se basa en la aceleración de Fermi cabe destacar las siguientes:

- Sistemas binarios de rayos X.

- Remanentes de supernovas cercanas a nuestra galaxia.

- Galaxias de núcleo activo.– Consisten en galaxias con un brillante núcleo en el centro debido supuestamente a un objeto compacto como por ejemplo un agujero negro.

- Explosiones de rayos gamma o *gamma ray bursts*.– Son explosiones violentas capaces de liberar grandes cantidades de energía y cuyo origen y formación hoy en día todavía son un misterio

- Microcuásares.– Son sistemas binarios formados por una estrella y un objeto compacto que se asemejan, no sólo en morfología a los grandes cuásares sino también a la física de los procesos que tienen lugar en su interior. Su proximidad a nosotros hace que sean una de las fuentes más probables de partículas aceleradas y por tanto de neutrinos.

Más exóticas son las propuestas de tipo *top–down*, donde sus defensores abogan por la existencia de partículas supermasivas como por ejemplo defectos topológicos, agujeros negros primarios y monopolos GUT. Los neutrinos también pueden ser una evidencia de la existencia de materia oscura no bariónica. La materia oscura se propone para explicar el hecho de que más del 90% de la materia en el Universo no es lumínica, las evidencias a su favor se concentran en los efectos gravitatorios presentes en la dinámica de galaxias. La materia oscura está formada por partículas que interaccionan débilmente pero con masas alrededor de la energía de la ruptura de la simetría electro–débil E_{EW}. Estos candidatos conocidos como WIMPs (*Weakly Interactive Massive Particles*) darían lugar al desintegrarse a un flujo de neutrinos detectable. Una de las partículas que se baraja como posible constituyente de la materia oscura es la partícula supersimétrica más ligera (LSP), que en muchos modelos de supersimetría se corresponde con el neutralino. Esta partícula sería estable y por tanto el producto final de las desintegraciones de las demás partículas supersimétricas. Finalmente, los neutralinos acabarían concentrándose en regiones densas del Universo, como el centro de la Galaxia, lo que aumentaría la probabilidad de autoaniquilación dando lugar a un flujo observable de neutrinos de una determinada energía. Otros posibles constituyentes de la materia oscura son los SUSY Q-balls, cuerdas cósmicas, y los anteriormente mencionados monopolos. Muchas de estas partículas tienen masas de 10^{14} eV lo cual las hace inalcanzables en un acelerador terrestre, siendo la medición de los neutrinos que provengan de sus desintegraciones una prueba directa de su existencia.

Telescopios de Neutrinos

La construcción de telescopios de neutrinos en el fondo del mar o bajo el hielo polar fue propuesta por Markov [33] en 1960. El principio de detección se basa en la observación de la luz Cherenkov que emiten los muones al atravesar un medio ópticamente adecuado como el agua o el hielo. Estos muones son el resultado de la interacción de los neutrinos muónicos de alta energía provenientes de fuentes astrofísicas con la materia que rodea el detector. La luz Cherenkov se produce cuando el muon muy energético viaja a través del medio con velocidad mayor que la de la luz en ese medio. Cuanto mayor es la energía del neutrino original mayor es la cantidad de luz recolectada por los fotomultiplicadores, por tanto mejor es también la resolución angular entre la dirección del neutrino original y el muon resultante.

Sin embargo, los retos tecnológicos a los que se enfrenta un telescopio de tales características son importantes. Tales dificultades son específicas del emplazamiento elegido para el detector, ya sea en el fondo marino o bajo el hielo.

Otras propuestas de detección de neutrinos surgidas en los últimos años se basa en la detección acústica de los neutrinos al interaccionar con el hielo, o la detección mediante ondas de radio y microondas.

El experimento ANTARES

El experimento ANTARES (*Astronomy with a Neutrino Telescope and Abyss environmental RESearch*) es una colaboración interdisciplinar en la que participan físicos, ingenieros, oceanólogos y astrónomos de Francia, Reino Unido, Alemania, España, Holanda, Italia y Rusia. La colaboración ANTARES eligió el mar Mediterráneo como emplazamiento de un detector de neutrinos de un área efectiva de 0.1 km^2. El telescopio estará formado por una serie de líneas distribuidas sobre el fondo marino. Dichas líneas estarán ancladas al fondo marino y mantenidas en posición vertical por medio de boyas colocadas en los extremos. Las líneas formarán una matriz tridimensional de fotomultiplicadores. El detector estará ubicado en la Costa Azul de Francia, cerca de Tolón, y a una profundidad de 2400 m. El emplazamiento elegido se beneficia de las instalaciones cedidas por el Instituto Oceanográfico Francés IFREMER situado en La Seyne, localidad donde se encuentra el centro de control del telescopio.

Las dificultades a las que se enfrenta el proyecto son varias y de distinta naturaleza. Por un lado, las condiciones extremas que se dan en el fondo del mar obligan a que los componentes electrónicos y mecánicos estén adaptados a tal medio, lo que conlleva un estudio exhaustivo de materiales y diseños que mejor soportan las condiciones de alta presión, corrosión y sedimentación del fondo marino. La física conlleva también grandes dificultades debido a que la baja sección eficaz de los neutrinos requiere la utilización de telescopios de gran área efectiva para conseguir una tasa de sucesos considerable. Las estimaciones existentes para el flujo de neutrinos astrofísicos indican la necesidad de crear telescopios del orden del km^2 para detectar, por ejemplo, fuentes puntuales de neutrinos. Del mismo modo, el hecho de estar sumergido bajo el agua tiene implicaciones físicas. Las desintegraciones del ^{40}K presente en la sal marina son las responsables de la principal fuente de fondo en el detector. Otra fuente de fondo, aunque menos problemática, es la bioluminiscencia. Ésta es debida a diversos animales o bacterias que adheridas a los fotomultiplicadores son capaces de emitir luz provocando grandes picos en la tasa de cuentas. A diferencia del ^{40}K constituye un fondo que se puede descartar fácilmente por la localización. Todos los parámetros y propiedades del agua han sido estudiados en una fase preliminar en el lugar del emplazamiento del detector. Durante esa fase también se estudiaron las diversas maniobras de despliegue de las líneas y su inmersión en el mar.

El proyecto ANTARES construirá un telescopio marino de un área efectiva de 0.1 km^2. La experiencia obtenida y los componentes desarrollados permitirán la construcción de un futuro telescopio de un km^2 de área efectiva. El detector ANTARES estará formado por 12 líneas separadas una distancia de 60 metros unas de otras. Todas ellas estarán conectadas al armario de conexiones (*Junction Box*) que a su vez unirá las líneas con la estación de tierra por medio de un cable electro-óptico a través del cual se transmitirán los datos obtenidos y se distribuirá la energía eléctrica a las líneas.

En la actualidad, ANTARES se encuentra en la fase de pre-producción en masa de líneas, habiendo realizado con éxito numerosos despliegues y recuperaciones de varias líneas de prueba. Diversos elementos como el armario de conexiones y el cable electro-óptico han sido ya sumergidos y permanecen bajo el mar esperando a que la líneas sean desplegadas y conectadas. En febrero de 2003 un sector de línea (un quinto de línea) de prueba llamado *Prototype Sector Line* fue sumergido con éxito junto con una línea (*Mini Instrumentation Line*) que contaba con diversos aparatos de calibración, medición y seguimiento de los parámetros ambientales que serán ubicados en algunas de las líneas estándares. Ambas líneas fueron recuperadas y posteriormente se realizaron diversas comprobaciones. Como resultado, se comprobó que la mayoría de los distintos componentes tanto electrónicos como mecánicos habían funcionado correctamente. Así pues, todo se encuentra dispuesto para la producción en masa, y se espera que la primera línea completa se instale en 2004 y la construcción del detector finalice y se encuentre operativo en el año 2006.

Prestaciones

Las prestaciones del detector se pueden presentar en función de diversas magnitudes. Estas variables describen la eficiencia del detector en diversos aspectos como el número de sucesos que es capaz de detectar, la resolución angular, etc.

- *Área efectiva.*– El área efectiva puede expresarse en términos de muones y neutrinos. En ambos casos lo que se mide con esta magnitud es la eficiencia del detector y representa la extensión que tendría una superficie plana de eficiencia 100% que observase el mismo número de neutrinos (muones) atravesándola. Esta cantidad es función de la energía y de la dirección del neutrino y es independiente del flujo incidente.

- *Resolución angular.–* La resolución angular se puede definir en términos del ángulo entre el muon reconstruido y el neutrino incidente con lo que hablaríamos de resolución angular de neutrinos, o bien como el ángulo entre el muon reconstruido y el muon producto de la interacción del neutrino con la materia, siendo en este caso la resolución angular de muones. En ambos casos la resolución angular se define como la mediana de la distribución de dichos ángulos. La resolución angular de muones es la que realmente describe el comportamiento del detector pues no engloba el ángulo físico entre el neutrino y el muon debido a la interacción del neutrino con la materia.

Ambas magnitudes se calculan para las diversas configuraciones del detector. El análisis de los resultados permite una comparación directa de la respuesta y eficiencia de las distintas geometrías propuestas en este trabajo.

También se han examinado las prestaciones reales del detector que se obtienen convolucionando las magnitudes anteriores con un flujo de neutrinos dado. Cuando se han usado estrategias de reconstrucción tridimensionales el flujo usado ha sido el correspondiente a fuentes astrofísicas ($d\Phi_\nu/dE \propto E^{-2}$), mientras que el flujo de neutrinos atmosféricos se ha usado en el análisis de la reconstrucción en una dimensión para el estudio de neutralinos y oscilaciones de neutrinos.

Objetivos

Hasta la fecha el diseño original de ANTARES consistía en un detector de 10 líneas con 30 pisos. Cada piso está provisto de tres módulos ópticos con un fotomultiplicador (PM) en su interior, haciendo que el detector en su conjunto posea un número total de 900 PMs. Dentro de una línea, los pisos están separados una distancia de 12 metros, lo que lleva a que la línea tenga una longitud de aproximadamente 360 metros. Este diseño de línea es lo que se conoce como línea *estándar*, y el detector descrito se corresponde con el modelo **d04**, también llamado detector de 10 líneas.

El objetivo principal de este trabajo es el estudio de las prestaciones de diversas configuraciones y geometrías en el telescopio de neutrinos ANTARES. El propósito es comprobar si se puede aumentar la eficiencia del detector aumentando el número total de líneas de 10 a 12 pero conservando el número de fotomultiplicadores (900 PMs). Para ello se han propuesto nuevos trazados de las líneas así como nuevos diseños de línea. Una vez configurados los nuevos detectores y creados mediante *software* se comparan diversas magnitudes para comprobar la eficiencia de cada detector, y su respuesta a distintos tipos de flujo de neutrinos y estrategias de reconstrucción de las trazas.

Nuevos trazados de 12 líneas

En este capítulo se mantiene el diseño estándar de 30 pisos con un total de 90 PMTs por línea, pero se añaden al diseño del detector dos líneas más, obteniéndose así un detector de 1080 PMs. Dicho detector es el **d08** y debido a su mayor número de fotomultiplicadores tendrá una mejor eficiencia que el antiguo detector de 10 líneas. Este primer paso nos permite estudiar con mayor detalle la relación entre el aumento del número de líneas y la conservación del número de PMs. Una vez comparadas las magnitudes entre estos dos detectores, podemos continuar proponiendo diseños con un total de 900 PMs. Sin embargo, antes de proceder con los diseños de 900 PMs, se estudian otros detectores de 1080 PMs para confirmar y validar la respuesta del detector **d08**. Estos nuevos detectores se diferencian del **d08** en el trazado de las líneas, siendo el trazado de éstos más compacto y con una menor área. Durante este capitulo estudiamos como se ven afectadas magnitudes tales como el área efectiva de muones y neutrinos, la resolución angular y el número de sucesos reconstruidos para un flujo de índice espectral 2.

Una vez analizado este primer paso, abordamos el diseño de nuevos detectores con 900 PMs. En este punto, se proponen nuevas configuraciones de líneas. A continuación presentamos una descripción de los diseños de líneas usados en este estudio:

- *Línea estándar.*– Esta línea, anteriormente descrita, posee 30 pisos separados una distancia de 12 metros unos de otros. El diseño de esta línea obliga a que si se desea restringir el número de PMs a 900 solo pueda usarse en un detector de 10 líneas, un detector de 12 líneas con este tipo de línea contaría con 1080 PMs.

- *Línea rala.*– Línea de 25 pisos separados una distancia de 14.5 metros, preservando de este modo la altura total del detector en 360 metros.

- *Línea cortada.*– Su diseño es básicamente el de la *línea estándar* a la que le han sido sustraídos los últimos 5 pisos, haciendo que la altura total del detector sea ahora de unos 300 metros. Tanto este diseño como el anterior tienen un número de 75 PMs por línea, con lo que ambos son los diseños usados para los detectores de 12 líneas con 900 PMs.

Las principales magnitudes de estos nuevos detectores de 900 PMs se comparan con el detector de 10 líneas **d04** y con el detector de 12 líneas y 1080 PMs **d08**, obteniéndose los primeros resultados y conclusiones sobre los distintos parámetros del detector.

Nuevos detectores de 12 líneas y estudio de la reconstrucción en una dimensión

En este capítulo se proponen otros detectores de 12 líneas con 900 PMs. Estos detectores siguen uno de los diseños de líneas descritos anteriormente pero el trazado de las líneas difiere de los propuestos hasta ahora. También en este capítulo se hace hincapié en la respuesta de los detectores, más concretamente de los diseños de línea, para la reconstrucción de una dimensión. Esta estrategia de reconstrucción fue desarrollada por la colaboración ANTARES para el rango de bajas energías, donde el interés físico principal es el estudio de la búsqueda de neutralinos y las oscilaciones de neutrinos atmosféricos. Es una reconstrucción totalmente distinta de los algoritmos tridimensionales, puesto que utiliza solamente los impactos de los PMs (*hits*) de una línea a la hora de reconstruir las trazas. Así pues, se espera que sea más sensible al diseño particular de las líneas (*estándar*, *cortada*, *rala*) que las estrategias tridimensionales que realizan la reconstrucción usando varías líneas. La respuesta de los detectores con distintos diseños de línea se comparan, y se estudian magnitudes como el número de sucesos reconstruidos para un flujo de neutrinos atmosféricos y la precisión con la cual se reconstruye el ángulo cenital.

Discusión de los resultados

En la primera parte de este Trabajo de Investigación, se comprueba que la eficiencia del detector de 12 líneas y 1080 PMs **d08**, expresada en términos de área efectiva de muones es mejor que la del telescopio de 10 líneas y 900 PMs **d04**, escalando la ganancia según el número de líneas añadidas. Sin embargo, un fenómeno inesperado ocurre a bajas energías por debajo de los $10^{2.5}$ eV. En ese rango de energía ambos detectores parecen tener la misma respuesta. Se prueban varias estrategias de reconstrucción de trazas, entre ellas la estrategia Carmona y la estrategia Aart, a fin de comprobar que dicho resultado no es causado por un problema en el *software* de reconstrucción. Una vez descartado que pueda deberse al software de reconstrucción, se propone una posible explicación basándose en el hecho de que a bajas energías la distancia entre líneas es más importante para reconstruir sucesos que el número de éstas. Así pues, y dado que en el trazado del detector **d08** la distancia entre líneas ha aumentado unos 5 metros con respecto al trazado del detector **d04**, el detector **d08**, pese a tener una gran ganancia de área efectiva a altas energías ($\sim 25\%$), a bajas energías se comporta como un detector de 10 líneas.

Con el fin de confirmar dicho fenómeno, se proponen nuevos trazados con una mayor *densidad de líneas* o menor distancia media entre ellas. Dichos trazados también de 1080 PMs, se corresponden con los detectores **d11** y **d12**, con los que se puede comprobar que el efecto desaparece a bajas energías pero que la ganancia a altas energías se ve reducida por el hecho de haber acercado las líneas. Nos encontramos pues, con un balance entre lo que se quiere ganar a altas energías y lo que se puede perder a bajas energías.

Una vez validado el hecho de que el fenómeno no se debe a ningún tipo de error en los útiles de reconstrucción, pasamos a testear los detectores con 900 PMs. Dichos detectores, que siguen el mismo trazado que el detector **d08**, se caracterizan por un cambio en el diseño de las líneas pasando del diseño *estándar* al diseño *ralo* o *cortado*. Estos nuevos detectores son el detector *ralo* **d10** y el detector *cortado* **d09**.

En este punto del estudio se puede comprobar que la altura del detector parece ser un factor importante siendo la ganancia de área efectiva de muones con respecto al detector de 10 líneas **d04** de sólo un 6% en el rango de altas energías (10^4–10^8 eV) para el detector *cortado* **d09** mientras que para el detector *ralo* **d10** la ganancia sube hasta un 16%. Sin embargo, la pérdida de eficiencia a bajas energías se hace más marcada en ambos detectores llegando a perder hasta un 3% con respecto al detector **d04** en el rango de bajas energías (10–10^4 eV). Este comportamiento es de esperar si tenemos en cuenta que ambos detectores siguen el trazado del detector **d08** en el que las líneas han aumentado su separación en 5 metros.

Otros parámetros como la resolución angular de los detectores así como la respuesta azimutal a un flujo de neutrinos atmosféricos se comparan también.

Una vez examinada la respuesta de los nuevos diseños de línea, se combinan con los trazados más *densos* propuestos anteriormente para evitar el efecto de pérdida en el área efectiva a bajas energías. Estos detectores, donde se opta por el diseño *ralo* frente al *cortado* por haber demostrado tener una mejor repuesta en la sección anterior, se corresponden a los detectores **d13**, **d15** y **d18**. En todos ellos aumenta la ganancia a bajas energías en el área efectiva de muones llegando a alcanzar para los detectores **d13** y **d15** hasta un 26%. Sin embargo, la ganancia a altas energías es menor que en los casos anteriores. De los tres nuevos detectores propuestos es el **d15** el que demuestra un mejor comportamiento teniendo en cuenta todo el rango de energía. Sin embargo, debido principalmente a su diseño asimétrico es el que muestra una respuesta azimutal menos uniforme y más dependiente del ángulo.

También se comparan en esta sección la respuesta de los distintos diseños de líneas a la estrategia de reconstrucción de una dimensión. Este tipo de reconstrucción no depende del trazado de las líneas, aunque el número total de líneas sí tiene una influencia ya que cuantas más líneas, más sucesos se pueden reconstruir. En esta sección comparamos los detectores **d08** (diseño *estándar*), **d10** (diseño *ralo*) y **d09** (diseño *cortado*). Todos ellos junto con el detector **d04** (diseño *estándar* pero de 10 líneas). Los resultados en este caso favorecen el diseño *cortado* donde ahora la altura del detector no es importante pero si la distancia entre pisos. De esta manera, el detector *ralo* **d10** es el que sale más perjudicado en este apartado en comparación con los detectores de 900 PMs.

En la tabla 4.5 se resumen las características de los distintos detectores estudiados:

Conclusiones

En este estudio hemos tenido que valorar diversos aspectos a la hora de decidir que diseño recoge mejor los intereses de la colaboración ANTARES. Por un lado, el detector ANTARES puede desarrollar la labor de telescopio de fuentes celestes. Para este fin y con el propósito de observar dichas fuentes por encima del fondo de neutrinos atmosféricos se necesita una energía umbral de $\sim$ 1 TeV. Es decir, el rango de altas energías está optimizado para la búsqueda de fuentes puntuales. Por el contrario la búsqueda de neutralinos tiene una energía umbral de $\sim$ 25 GeV cercana a la del estudio de oscilaciones de neutrinos $\sim$ 10 GeV (aunque ésta última depende de Δm^2). De modo que una baja eficiencia en el rango de bajas energías afectaría al estudio de neutralinos y oscilaciones de neutrinos. Por ese motivo, la elección del diseño del detector es una tarea en la que hay que sopesar muchos aspectos y en la que hay que hacer un balance

Detector	núm. de líneas	núm. de PMs	núm. de pisos	distancia entre pisos (m)	Trazado	Diseño de línea
d04	10	900	30	12	TDR 10–líneas	*estándar*
d08	12	1080	30	12	octogonal	*estándar*
d09	12	900	25	12	octogonal	*cortado*
d10	12	900	25	14.5	octogonal	*ralo*
d11	12	1080	30	12	octogonal reducido	*estándar*
d12	12	1080	30	12	hexagonal	*estándar*
d13	12	900	25	14.5	hexagonal	*ralo*
d15	12	900	25	14.5	TDR asimétrico	*ralo*
d18	12	900	25	14.5	TDR simétrico	*ralo*

Table 4.5: Descripción de los detectores de 12 líneas comparados en este estudio junto con el detector original de 10 líneas **d04**.

entre la eficiencia que se quiere ganar a altas energías y a bajas. Por esta razón y teniendo en cuenta que la función principal del detector ANTARES es la de telescopio de fuentes astrofísicas, **d10** es el detector que mejor se adapta a las exigencias de la colaboración, siendo el elegido para la construcción del telescopio ANTARES.

Bibliography

[1] V. F. Hess. *Phys. Z.*, 13:1084, 1912.

[2] K. Greisen. *Phys. Rev. Lett.*, 16:748, 1966.

[3] M. Takeda et al. *Phys. Rev.*, 81:1163, 1998.

[4] T. Abu-Zayyad et al. (HiRes collaboration). *astro-ph/0208243, astro-ph/0208301.*

[5] E. Fermi. On the origin of the cosmic radiation. *Phys. Rev.*, 75(8):1169, April 15 1949.

[6] A. M. Hillas. *Ann. Rev. Astron. Astrophys.*, 22:425, 1984.

[7] S. L. Glashow S. Coleman. *Phys. Rev. D*, 59:116008, 1999.

[8] K. Mannheim. *Science*, 279:676, 1998.

[9] C. E. Fichtel and J. I. Trombka. Gamma-ray astrophysics: New insight into the universe. Technical report, 1997. NASA-RP-1386.

[10] M. et al. Punch. *Nature*, 358:477, 1992.

[11] Quinn et al. *Astrophy. Journal*, 456, 1996.

[12] K. S. Hirata et al. *Phys. Rev. Lett.*, 58:1490, 1987.

[13] A. Dar S. Dado and A. De Rújula. The supernova associated with GRB 030329. *astro-ph/0304106.*

[14] E. Waxman and J. Bachall. *Phys Rev. Lett.*, 78:2292, 1997.

[15] A. Dar and A. De Rújula. The cannonball model of gamma ray burst: spectral and temporal. *astro-ph/0012227.*

[16] F. D. Torres et al. Nearby quasar remnants and ultra-high energy cosmic rays. astro-ph/0204419.

[17] O. Reimer et al. *Astron. Astrophys*, 390:L43, 2002.

[18] K. S. Cheng et al. *J. Phys*, G(16):1115, 1990.

[19] F. A. Aharonian and A. M. Atoyan. *APH*, (3):275, 1995.

[20] D. Guetta and E. Amato. *APh*, 19(403), 2003.

[21] I. F. Mirabel and L. F. Rodriguez. *astro-ph/9902062*, 1999.

[22] E. Waxman C. Distefano, D. Guetta and A. Levinson. *ApJ*, 575:378, 2002.

[23] B. Zhang et al. *ApJ*, (595):346, 2003.

[24] P. Bhattacharjee and G. Sigl. Origin and propagation of extremely high-energy cosmic rays. *Phys. Rep.*, 327:109, 2000.

[25] V. Berezinsky and M. Kachelriess. *Phys. Rev. D*, 63:34007, 2001.

[26] P. Gondolo and J. Silk. Dark matter annihilation of the galactic center. *MPI-PhT/99-10*, OUAST/99/9(OUAST/99/9), March 1999.

[27] T. J. Weiler P. L. Biermann S. D. Wick, T. W. Kephart. *astro-ph/0001233*.

[28] A. Barrau. *Astropart. Phys.*, 12:269, 2000.

[29] I. Affleck and M. Dine. *Nucl. Phys. B*, 249:361, 1985.

[30] Super Kamikande Collaboration. *Phys. Lett.*, B539:179–187, 2002.

[31] The SNO collaboration. *Phys. Rev. Lett.*, 89(1):011301, 2002.

[32] Y. Ashie et al. *hep-ex/0404034*, 2004.

[33] A. M. Markov. In *Proceedings of the Rochester Conference*, New York, 1960.

[34] J. G. Learned and S. Pakvasa. *APh*, 3:267, 1995.

[35] R. Ghandi et al. *Astropart. Phys.*, 5:81, 1996.

[36] CTEQ Collaboration. http://www.phys.psu.edu/ cteq/.

[37] ANTARES Collaboration. A deep sea telescope of high energy neutrinos. *astro-ph/9907432*, 1999.

[38] J. Brunner. The refraction index at the antares site. *ANTARES internal note*, 2000.

[39] Agrawal et al. *Phys. Rev.*, D53:1314, 1996.

[40] Protheroe. astro-ph/9607165.

[41] K. Mannheim. *Astrop. Phys.*, 11:49, 1999.

[42] Halzen and Hooper. *Astrophys. J. Lett*, 527:L93–L96, 1993.

[43] Waxmman and Bahcall. *Phys. Rev.*, D59:023002, 1999.

[44] Protheroe K. Mannheim and Rachen. *Phys. Rev.*, D64(023003), 2000.

[45] ANTARES Collaboration. Conceptual design report of the $0.1km^2$ detector. *ANTARES internal document*, 1999.

[46] ANTARES Collaboration. The fouling of optical surfaces in the antares site. *ANTARES internal note*, 2001.

[47] The AMANDA Collaboration. *Nucl. Phys. B (Proc. Suppl.)*, 91:423, 2000.

[48] M. P. Kowalski and A. Karle et al. AMANDA contributions to the 28th ICRC. In *Proceedings of the 28th International Cosmic Ray Conference*, volume 3, pages 1301–1325, Tsukuba, 2003. Universal Academic Press. ISBN 4-946443-80-0.

[49] K. Woschnagg. New results from AMANDA. *Neutrino 2004*, Paris, France.

[50] M. Ribordy. AMANDA: status and latest results. *hep-ex/0405035*.

[51] The IceCube Collaboration. IceCube: A kilometer scale neutrino observatory. NSF Proposal, 2001. http://pheno.physics.wisc.edu/IceCube/proposal.html.

[52] S. Yoshida. The IceCube high energy neutrino telescope. In *Proceedings of the 28th International Cosmic Ray Conference*, volume 3, pages 1369–1373, Tsukuba, 2003. Universal Academic Press. ISBN 4-946443-80-0.

[53] The Baikal Collaboration. *Nucl. Phys. B (Proc. Suppl.)*, 91:438, 2000.

[54] M. P. Kowalski. Results from the Baikal neutrino telescope. In *Proceedings of the 28th International Cosmic Ray Conference*, volume 3, pages 1353–1356, Tsukuba, Japan, 2003. Universal Academic Press. ISBN 4-946443-80-0.

[55] Zh. Dzhilkibaev. The baikal experiment. status, results and perspectives. *Neutrino 2004*, Paris, France.

[56] The NESTOR Collaboration. *Nucl. Phys. B (Proc. Suppl.)*, 85:153, 2000.

[57] P. K. F. Grieder. Nestor neutrino telescope status report. In *Proceedings of the 28th International Cosmic Ray Conference*, volume 3, page 1377, Tsukuba, Japan, 2003. Universal Academic Press. ISBN 4-946443-80-0.

[58] A. Capone. Site characterization for a km^3 scale deep underwater astrophysical neutrino observatory in the Mediterranean Sea. In *Proceedings of the 26th International Cosmic Ray Conference*.

[59] Extension of Genneu v3r0 event generator for high energy neutrino interactions with muon propagation to the detector. ANTARES internal note. ANTARES-Soft/2000-005.

[60] David J. L. Bailey. Genhen v3r1 : Further optimization for large energy ranges. ANTARES Internal Note. ANTARES-Soft/2000-6.

[61] D. J. L. Bailey. Genhen v5r1: Software documentation. ANTARES internal note. ANTARES-Software/2002-004.

[62] G. Ingelman et al. Lepto 6.5. *Comput. Phys. Common*, 101:108, 1997.

[63] G. D. Barr. *The separation of signal and background in nucleon decay experiment.* PhD thesis, University of Oxford, United Kingdom, 1987.

[64] E. Scapparone. HEMAS: a Monte Carlo code for hadronic, electromagnetic and TeV muon components in air shower. In *Proceedings of the International Workshop on Simulation and analysis methods for large neutrino detectors, Desy Zeuthen (1998)*, pages 238–246. (physics/9902043).

[65] Study of the atmospheric muon background with hemas and corsika. ANTARES internal note. ANTARES-Soft/2003-005.

[66] Study of the atmospheric muon background with hemas and corsika. part 2: Propagation to the can level. ANTARES internal note. ANTARES-Soft/2003-006.

[67] P. Antonioli, C. Ghetti, E. V. Korolkova, V. A. Kudryavtsev, and G. Sartorelli. A three-dimensional code for muon propagation through the rock: Music. *Astropart. Phys.*, 7:357–368, 1997.

[68] P. Lipari and T. Stanev. Propagation of multi TeV muons. *Phys. Rev.*, D44:3543, 1991.

[69] I. A. Sokalski, E. V. Bugaev, and S. I. Klimushin. MUM: flexible precise Monte Carlo algorithm for muon propagation through thick layers of matter. *Phys. Rev.*, D64:074015, 2001.

[70] D. Bailey. Km3 v2r1 : User guide. ANTARES Internal Note. ANTARES-Soft/2002-006.

[71] J. Brunner. Geasim: User manual. ANTARES Internal documentation. http://antares.in2p3.fr/internal/software/geasim.html.

[72] S. Navas. A comparison between GEASIM and KM3 generators. ANTARES Internal Note. ANTARES-Soft/1999-002.

[73] J. S. Ricol. *Etude de la dètection de monopôles magnétiques au sein du futur télescope à neutrinos Antares et caractérisation des performances du traitement des impulsions des photomultiplicateurs.* PhD thesis, Université de la Méditérranée–Aixx Marselle II, France, 2002.

[74] F. Cassol. Reconstruction re-organization: RECO version 2.0. ANTARES internal note. ANTARES-Soft/1999-004.

[75] F. Cassol. RECO version 2.1: code and scripts. ANTARES internal note. ANTARES-Soft/1999-005.

[76] A. Romeyer and Th. Stolarczyk. Reconstruction algorithms: a handbook for developers. ANTARES internal note. ANTARES-Soft/2001-001.

[77] E. Carmona. *Study of the event reconstruction and expected performances for the point-like sources of the future ANTARES neutrino telescope.* PhD thesis, Universitat de València, Spain, 2003.

[78] A. Heijboer. An algorithm for track reconstruction in ANTARES. ANTARES internal note. ANTARES-Phys/2002-002.

[79] R. Brun and F. Rademakers. ROOT - An Object Oriented Data Analysis Framework. *Nucl. Inst. & Meth. in Phys. Res.*, A389:81, 1997. See also http://root.cern.ch/.

[80] F. Cassol. GENDET 1.0: A program to generate detector files. ANTARES Internal Note. ANTARES-Soft/1999-007.

[81] F. Cassol Brunner. GENDET 1.2: Cards and tags. ANTARES Internal Note. ANTARES-Soft/2000-8.

[82] D. J. L. Bailey. *Monte Carlo tools and analysis methods for understanding the ANTARES experiment and predicting its sensitivity to Dark Matter.* PhD thesis, University of Oxford, United Kingdom, 2002.

[83] A. Heijboer. *Track reconstruction and point source searches with ANTARES.* PhD thesis, Universiteit van Amsterdan, 2004.